Comprehensive Ionization Model Development for the FEBIAD Ion Source and Its Application for TRIUMF's Radioactive Ion Beam Program

by

Fernando Alejandro Maldonado Millán
B. Sc., Universidad Autónoma de Yucatán, 2013
M. Sc., University of Victoria, 2016

A Dissertation Submitted in Partial Fulfillment of the
Requirements for the Degree of

DOCTOR OF PHILOSOPHY

in the Department of Physics and Astronomy

Comprehensive Ionization Model Development for the FEBIAD Ion Source and Its Application for TRIUMF's Radioactive Ion Beam Program

by

Fernando Alejandro Maldonado Millán
B. Sc., Universidad Autónoma de Yucatán, 2013
M. Sc., University of Victoria, 2016

Supervisory Committee

Dr. A. Gottberg, Co-Supervisor
(Department of Physics and Astronomy, TRIUMF)

Dr. D. Karlen, Co-Supervisor
(Department of Physics and Astronomy)

Dr. M. Lefebvre, Departmental Member
(Department of Physics and Astronomy)

Dr. R. Herring, Outside Member
(Department of Mechanical Engineering)

ABSTRACT

Radioactive isotopes enable advanced medical treatments and the study of nuclear structure, nuclear astrophysics, and fundamental symmetries. TRIUMF, Canada's Particle Accelerator Centre, generates radioactive isotope beams using the Isotope Separation On-Line method. At TRIUMF, the Forced Electron Beam Induced Arc Discharge (FEBIAD) ion source is used to ionize specific isotopes but often presents limited performance and lower efficiencies compared to other facilities. To investigate the source limitation, elucidate the ionization mechanism, and propose improved and highly efficient sources for upcoming facilities, a combined numerical and experimental campaign has been undertaken. The developed numerical ionization model is able to describe the source as an electron impact ion source that is governed by strong space charge effects. The spatially distributed ionization rate is higher at specific locations of the anode volume, and this has been confirmed experimentally. The validated numerical model has been further used to propose simulation-based optimizations. With the overall optimization, the ionization efficiency for the TRIUMF FEBIAD is expected to increase ten-fold.

Contents

List of Tables

List of Figures

List of Acronyms

FEBIAD Forced Electron Beam Induced Arc Discharge

RIB Radioactive Ion Beam

ISOL Isotope Separation On-Line

ISAC Isotope Separation and ACceleration facility

ARIEL Advanced Rare IsotopE Laboratory facility

SIS Surface Ion Source

RILIS Resonant Ionization Laser Ion Source

RMS Root Mean Squared

IG-LIS Ion Guided Laser Ion Source

TIS Target and Ion Source

ISAC TS ISAC Test Stand

ISAC EVP2 ISAC EVaPorator #2

HLA High Level Application

FEA Finite Element Analysis

FWHM Full Width at Half Maximum

ACKNOWLEDGEMENTS

I would like to thank:

Anders Mjøs and Aaron Schimdt, for their help in performing experiments at TRIUMF.

Pierre Delahaye and Ujic Predrag, for their help in performing experiments at GANIL.

Carla Babcock and Thomas Day Goodacre for their support, discussion, and insight.

Alexander Gottberg, for support, encouragement, and patience.

Dean Karlen, for support and advises throughout my degree program.

University Of Victoria, for funding me with a Scholarship.

TRIUMF, for letting me being part of the ARIEL project.

DEDICATION

My parents and brothers are the first persons I want to thank: Alejo, Amalia, Guillermo, and Luis. They were my first source for trying to find answers and sparking my curiosity. I also remember reading my brother's notebooks when I was a kid and wondered what those weird symbol were (integral signs). I also dedicate this work to Marla, *una flamante mujer* who is also my life companion. Her support during this madness will be forever thanked.

Introduction

TRIUMF is Canada's Particle Accelerator Centre and for more than 50 years it has built and advanced a strong scientific program in a variety of fields. The scientific success is mostly enabled by the largest cyclotron of the world, which generates proton beams with an energy up to 520 MeV. The proton beam serves to characterize materials, contributes to treatments of certain types of cancer, and creates radioactive isotopes that do not occur naturally. Particularly, the radioactive isotopes support advanced treatments and diagnostics in various fields of medicine, and also enable the study of nuclear structure, nuclear astrophysics, and fundamental symmetries.

To generate radioactive isotope beams, TRIUMF utilizes the Isotope Separation On-Line (ISOL) method. In an ISOL facility, a driver beam impinges on a thick target where nuclear reaction products diffuse and effuse into an ion source. The ion source ionizes the reaction products that are consequently extracted with an electric field and sent towards a dipole electromagnet. The electromagnet separates the ions according to their momentum-to-charge ratio forming the Radioactive Ion Beam (RIB), which is finally transported and delivered to the experimental areas. To provide the different RIBs requested, several target material and ion source combinations are used [1]. Typically, a chosen combination aims at reliable high performance for approximately three weeks.

For the past 20 years at TRIUMF, the Isotope Separation and ACceleration (ISAC) facility has been responsible for generating the RIBs used in the different experimental areas. The facility consists of two ISOL target stations that are used alternatively for approximately three weeks. This operation mode arises from the single proton line driving the RIB production.

To increase its ISOL capabilities, TRIUMF is developing the Advanced Rare IsotopE Laboratory (ARIEL) facility. ARIEL consists of two target stations that can operate simultaneously. One target station uses a new proton beamline from the cyclotron while the other uses a state-of-the-art electron linear accelerator. With

the added flexibility and a new type of driver beam, ARIEL not only increases the number of RIB hours delivered to the experiments but also creates Research-and-Development (R&D) opportunities to increase the ISOL efficiency and access to new radioactive isotopes.

The RIB production and delivery of the ISOL method have specific associated efficiencies, ranging from nuclear reaction and ion extraction to final beam delivery. Out of all the efficiencies involved, the isotope release from the target material and the isotope ionization are the smallest ones, with their lower values around 10^{-4} % and 10^{-1} %, respectively. Because of these limiting values, R&D for highly efficient target material and ion sources is paramount.

The ISOL ion source has to be not only efficient but also selective due to the wide range of nuclear production using high-energy driver beams, and the limited selectivity of most experiments. Moreover, different ion source designs are required to span over the range of Ionization Potentials (IPs) [2]. For instance, elements or molecules with IP$<$ 6 eV are successfully ionized with a Surface Ion Source (SIS); for IP$<$ 10 eV, the Resonant Ionization Laser Ion Source (RILIS) is efficient and highly selective for elements; finally for elements and molecules with IP$>$ 10 eV, the choice is the Forced Electron Beam Induced Arc Discharge (FEBIAD) ion source [3].

Both the SIS and RILIS are well-understood ion sources; however, the FEBIAD still poses in-depth understanding challenges and in the case of ISAC, it also presents operational challenges. Few studies have tried to understand the mechanism behind the FEBIAD ionization process and RIB extraction due to the source complexity [4, 5]. To investigate the limitations of the ISAC FEBIAD and to understand the underlying physical mechanisms of the FEBIAD ion source, a combined simulation and experimental campaign has been conducted. The first chapter presents an overview of the three main ion sources used in the ISOL method with an emphasis on the FEBIAD. The second chapter introduces the experimental tools used and the simulation software employed. The third chapter describes the physical mechanisms involved in the generation of the RIB alongside the numerical model developed that have resulted in a publication [6]. The fourth chapter presents the characterization of the FEBIAD ancillary systems, such as heating, and how the results validate the engineering simulations. The fifth chapter presents the experimental campaign for ionization efficiency measurements and how the model describes the ion source, which have also resulted in a publication [7]. The sixth chapter presents a series of simulation-based optimizations for the FEBIAD ion sources used at TRIUMF. The final chapter presents the conclusions drawn from the research.

Chapter 1

Ion Sources for Radioactive Ion Beam Production

Ion sources enable the application of ion beams in diverse fields such as medicine, industry, and science. Based on the individual source application, they differ in their geometry, lifetime, and ionization mechanism. In the context of this research, ion sources for radioactive ion beam production are described in detail but similarities and differences with ion sources for stable ions are highlighted.

1.1 General Aspects of an Ion Source

Producing ion beams requires specialized ion sources to create the desired ionized element. Different ionization techniques exist, but the ions are often created and extracted from a gas discharge plasma. To ignite and sustain the plasma, stringent requirements on pressure, electric field, and magnetic field need to be satisfied. Irrespectively of the ionization technique, electric and magnetic fields are used to extract, control, and deliver the ions to the experimental area.

Ion sources may differ in their implementation but common figures of merit allow quantifying and comparing their performance. To characterize the beam quality, a common figure of merit is the transverse beam emittance. For an ion beam moving in the z-direction, the transverse emittance is the area occupied by particles in phase space defined by the particle's position and momentum $[x, p_x]$, or more commonly in the so-called trace space $[x, x']$ where $x' = p_x/p_z$. Moreover, measured emittances are reported with a statistical definition known as the 4-Root-Mean-Squared-emittance.

The 4RMS-emittance, $\epsilon_{4\text{rms}}$ (µm), of the beam in the x-direction[1] is calculated using

$$\epsilon^{x}_{4\text{rms}} = 4\sqrt{V_x V_{x'} - V^2_{x\cdot x'}}, \tag{1.1}$$

where V_x is the variance of the position distribution (m^2), $V_{x'}$ (unitless) the variance of the angle distribution, and $V_{x\cdot x'}$ (m) the covariance among both distributions [8]. This definition guarantees that around 90 % of the particles are contained within the area (see Fig 1.1). A small emittance indicates that a beam is compact and does not spread out when moving along the beamline.

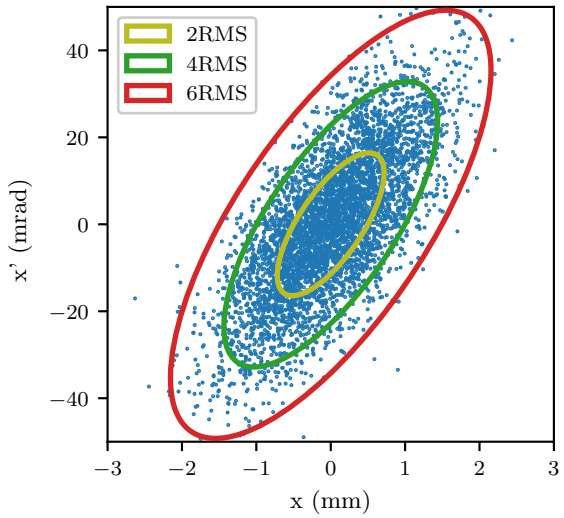

Figure 1.1: Phase space plot from which the emittance can be computed. Each point represents a particle of the beam. Typically, a 4RMS area is used because it contains approximately 90% of the particles.

In addition to the emittance, another beam quality figure of merit is the energy spread. The source of energy spread can be due to multiple reasons. From ripples on the power supply, resulting in voltages oscillations on the extraction, to intrinsic energy gain after the ionization process. Regardless of the origin, a large energy spread can become detrimental for some applications. Conversely, a small energy spread corresponds to near mono-energetic beams, which reduces the chances of transport losses. For example, a state-of-the-art momentum separator requires an emittance smaller than 3 µm and an energy spread smaller than 1 eV/60 keV to achieve proper momentum (mass) selection [9].

[1] The same relation holds for the vertical direction y and $y' = p_y/p_z$, and is identical to $\epsilon^{x}_{4\text{rms}}$ when cylindrical symmetric systems are studied.

The last figure of merit to discuss is the efficiency of the ion source. The term *efficiency* can be defined differently depending on the field of application. For instance, industrial applications might quote an efficiency based on the ratio of consumed wall power over generated ion current [10]. Other fields report it as the ratio of ions extracted over available neutrals. The latter definition is decisive for applications where neutrals are scarce, as is the case for radioactive ion beam production.

1.2 Emergence and Application of Ion Sources for Radioactive Ions

Nuclear physics investigations in the late 1930s motivated the development of efficient proton, deuterium, and helium ion sources [11]. By combining these sources with an electromagnet as a mass separator, the ion beams enabled spectroscopic nuclear disintegration experiments [12]. To further investigate species with half-lives in the order of 10 s, the ion sources were coupled to a cyclotron driving a nuclear reaction target in what is currently known as the Isotope Separation On-Line (ISOL) method [13, 14].

In the ISOL method, a driver beam impinges on a thick target to induce nuclear reactions (see Fig 1.2). The reaction products diffuse out of the target material and effuse, via a transferline, into the ion source to be ionized. The ions are extracted with an electric field and transported into a dipole electromagnet that separates the beam components based on their momentum-to-charge ratio to form a Radioactive Ion Beam (RIB).

The RIB intensity, I_{RIB} (s^{-1}), is given by [15]

$$I_{\mathrm{RIB}} = \sigma_{\mathrm{n}} \cdot I_{\mathrm{d}} \cdot N_{\mathrm{t}} \cdot \varepsilon, \tag{1.2}$$

where σ_{n} is the cross section of the nuclear reaction process (m^2), I_{d} the driver beam intensity (s^{-1}), N_{t} the number of target atoms per surface area (m^{-2}), and ε the total efficiency of the overall processes involved:

$$\varepsilon = \varepsilon_{\text{release}}\, \varepsilon_{\text{ionization}}\, \varepsilon_{\text{transport}}\, \varepsilon_{\text{bunching}}\, \varepsilon_{\text{post-acceleration}}\,. \tag{1.3}$$

The transport, bunching, and post-acceleration efficiencies reach values around 10^1 % to 10^2 %, but the target release and the ionization efficiencies have their lower values around 10^{-4} % and 10^{-1} %, respectively [16].

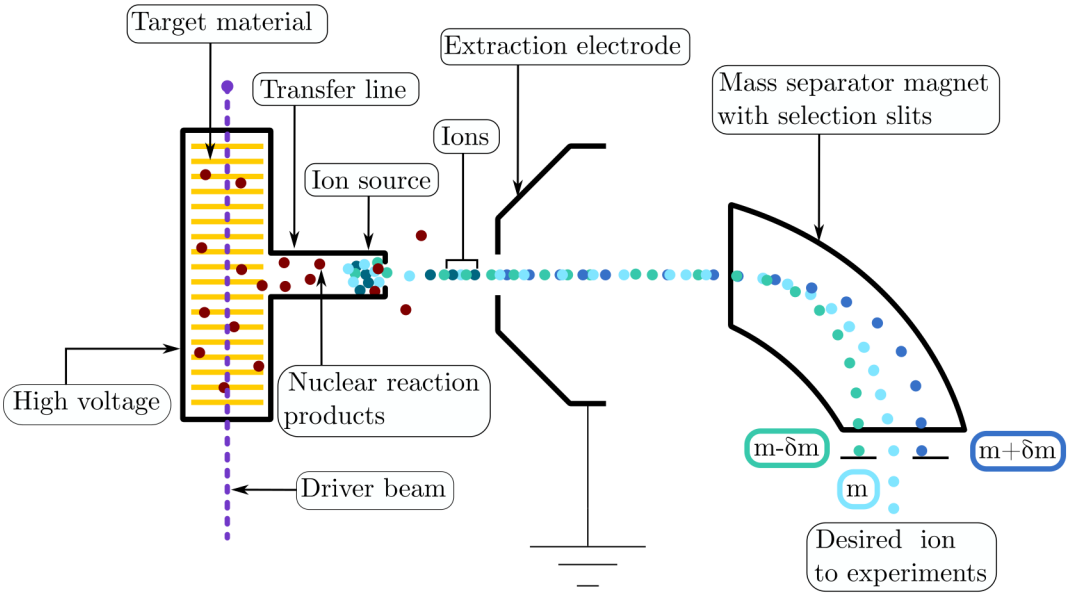

Figure 1.2: Schematic of the Isotope Separation On-Line method. A broad range of reaction products are created in different amounts and they diffuse and effuse into the ion source. The ions extracted are separated and go through some extra manipulation, if required, before arriving at the experiment.

The research and development for a more efficient ion source differ between stable and radioactive beams. For example, a stable ion beam source aims for long-term reliability and low power consumption while typically operating with a surplus of neutral species to ionize. These stable sources are often accessible during operation and are therefore easy to repair and maintain. Conversely, the radioactive ion source has to sustain radiation damage, making them inaccessible even after completed operations; when the sources need to be diagnosed, remote handling infrastructure is required to access them. Nevertheless, a radioactive ion source mainly has to maximize the ionization efficiency as the number of neutrals to ionize is scarce. In addition, the source has to be as chemically selective as possible to suppress unwanted products on similar masses (isobaric contaminants). Moreover, given the long transport system and the series of post-acceleration steps involved, the beam quality has to be maximized and the beam-self-repulsion minimized. Because of these transport constraints on self-repulsion, ion currents desired are typically below the order of 1×10^{-6} A [17].

ISOL facilities currently under construction [18–23] require more efficient radioactive ions sources to achieve higher RIB intensities. The differences highlighted create unique challenges for the radioactive ion source development. As RIBs are hindered by neutral production, the figure of merit to characterize the ion sources is the ion-

ization efficiency. This efficiency is defined as

$$\varepsilon_{\text{ionization}} = \frac{n_{\text{i}}}{n_{\text{n}}} \ ,$$

where n_{i} is the rate of ions extracted (s^{-1}) and n_{n} is the rate of neutrals entering the ion source (s^{-1}).

The following sections present an overview of the most common ion sources used in the ISOL method to produce singly charged ions.

1.3 Surface Ion Source

The Surface Ion Source (SIS) is one of the simplest yet robust and reliable ion sources for producing singly charged ions. The SIS is not only used at TRIUMF [24] but also at other ISOL facilities due to the well-understood ionization mechanism. The ionization of a neutral element occurs upon contact with a hot metal, where the atom is adsorbed into the wall with an increased probability of being released as an ion (see Fig. 1.3).

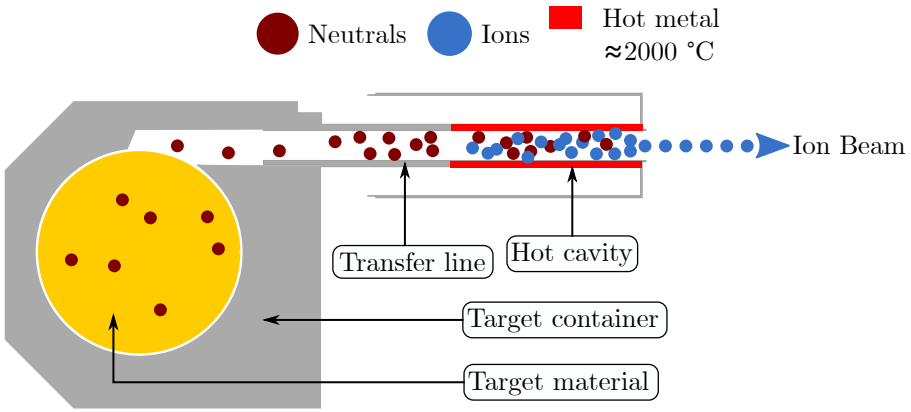

Figure 1.3: Surface Ion Source schematic. The neutrals move through the transfer line to reach the hot metal region where the ionization occurs.

The degree of ionization α can be described by the Saha-Langmuir equation [25]:

$$\alpha = \frac{\rho_{\text{i}}}{\rho_{\text{n}}} = \frac{g_{+}}{g_{\text{o}}} \exp\left[\frac{W - P_{\text{i}}}{k_{\text{B}} T}\right], \tag{1.4}$$

where ρ_{i} and ρ_{n} are the number densities of ions (m^{-3}) and neutral atoms (m^{-3}), respectively; g_{+} and g_{o} are the statistical weights of the ionic and atomic states, respectively; W is the material work function (eV), T the surface temperature (K), k_{B} the Boltzmann constant (eV K^{-1}), and P_{i} the first ionization potential of the atom (eV).

The ionization efficiency $\varepsilon_{\text{ionization}}$ of the SIS is computed as the following [26]

$$\varepsilon_{\text{ionization}} = \frac{\rho_{\text{i}}}{\rho_{\text{i}} + \rho_{\text{n}}} = \frac{\rho_{\text{i}}}{\rho_{\text{n}}} \frac{1}{(1 + \rho_{\text{i}}/\rho_{\text{n}})} = \frac{\alpha}{1 + \alpha}; \tag{1.5}$$

however, a modified equation was found in [27] and this indicates an enhancement factor in α as $\alpha \rightarrow \omega\kappa\alpha$, in the ionization efficiency that is:

$$\varepsilon_{\text{ionization}} = \frac{\omega\kappa\alpha}{1 + \omega\kappa\alpha}, \tag{1.6}$$

where the enhancement factor arises from the ion trapping (ω) along the ionizer tube and the increased number of neutral-wall collisions (κ).

Equation 1.4 suggests that a high work function material increases the efficiency, while also defines the maximum ionization potential. With the most common ionizer materials listed in Table 1.1, alkalis with first ionization potentials ranging from 3.89 eV to 5.3 eV are efficiently ionized. Nevertheless, operating the source at a higher temperature enables IPs$\leq$7 eV to be ionized as well.

Table 1.1: Common materials used for the ionizer tube and their work function [28].

Material	**Work function (eV)**
Tantalum	4.25
Tungsten	4.55
Rhenium	4.72

At TRIUMF, a rhenium foil is inserted in the hot cavity region to increase the work function locally and consequently increase the ionization efficiency [24]. In 2019, 100 % of the SIS implemented a rhenium foil [29].

1.4 Resonant Ionization Laser Ion Source

The Resonant Ionization Laser Ion Source (RILIS) is the most requested ion source at TRIUMF due to its efficient chemical selectivity [30]. This selectivity arises from the ionization mechanism, which is achieved through a series of lasers that match the energy levels of the outermost electron (see Fig. 1.4). This mechanism also means that selection between isotopes of the same mass (isobars) is possible provided that the energy levels are known. Typically during online operations, there are dedicated measurements to find optimal transitions and/or maximize the transition efficiency of the laser schemes.

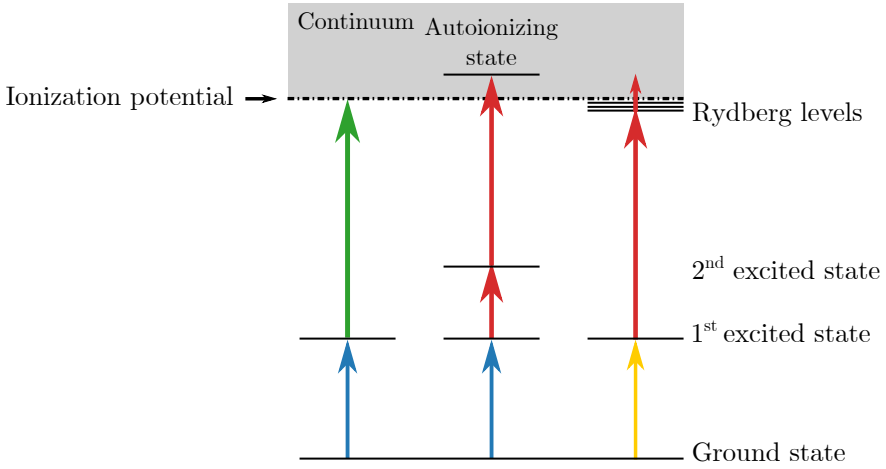

Figure 1.4: RILIS principle of operation. Atomic energy levels are matched with a sequence of lasers to remove the outermost electron. Ionization via resonant steps, ionization via an autoionizing state, and ionization via Rydberg levels are depicted.

The main drawbacks for the RILIS is the incapability of ionizing noble gases or molecules, but more importantly is the requirement of an atom-laser interaction region which is commonly the SIS hot cavity (see Fig. 1.5). The hot cavity both causes increased thermal velocity of the neutrals and additional surface ionized species that limit the chemical selectivity of the source. To prevent surface ionized species from extraction, a repulsive electrode is sometimes placed in front of the hot cavity to repel ions and only allow neutrals to enter a radio-frequency guide. With this setup, a specialized region for atom-laser interaction is achieved and this source is known as Ion-Guided Laser Ion Source (IG-LIS) [31]. Despite reducing the total number of ions extracted, the IG-LIS significantly increases the beam purity.

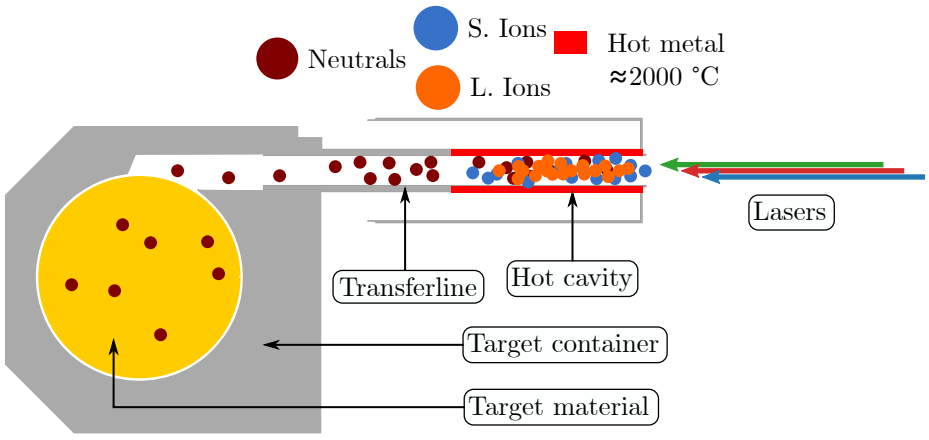

Figure 1.5: RILIS ionization schematic. Lasers are directed into a surface ion source, from which both surface ionized (S. Ions) and laser ionized (L. Ions) species are extracted.

1.5 Forced Electron Beam Induced Arc Discharge Ion Source

The ion source typically used for producing singly charged RIBs of noble gases, halogens, or molecules is the Forced Electron Beam Induced Arc Discharge (FEBIAD) ion source. In a FEBIAD, neutral atoms effuse into an anode volume where electrons cause electron impact ionization (see Fig. 1.6). The electrons are generated via thermionic emission from a hot cathode and accelerated with an electric field between the anode and the cathode. Additionally, an electric current flowing through an electromagnetic coil generates a magnetic field that focuses and confines the electrons in the axial direction. Finally, the ions are extracted with an electric field defined by the extraction electrode set to ground potential.

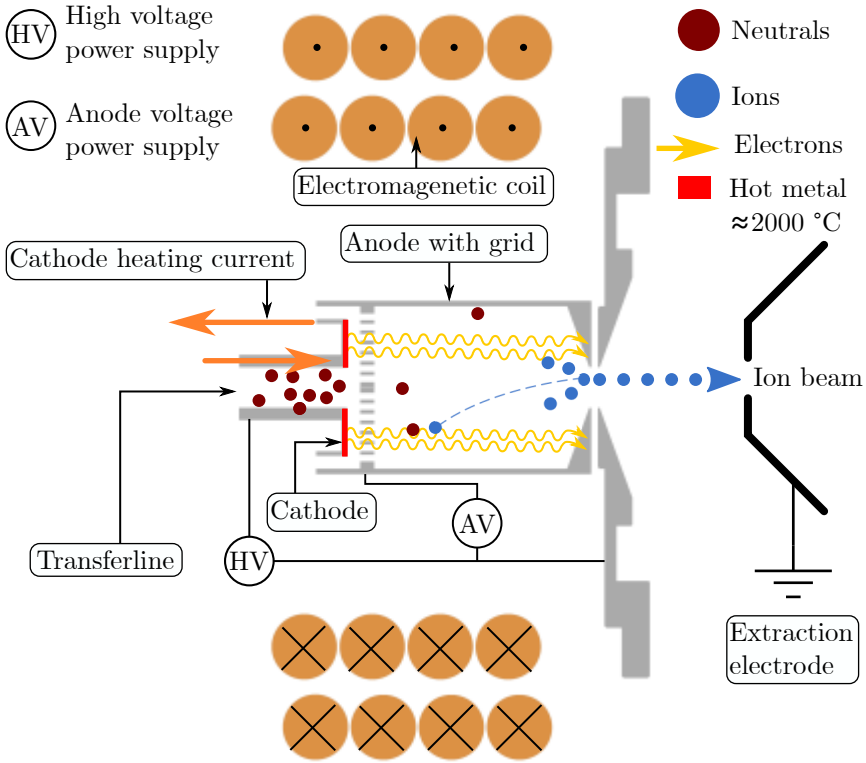

Figure 1.6: FEBIAD ion source cross sectional view with a depiction of the ionization process. Neutrals effuse from a transferline (target container not shown) into the anode volume where they interact with electrons emitted from the hot metal cathode and accelerated towards the anode grid to cause ionization. An extraction electrode generates an electric field that guides the ions towards the anode outlet to form the ion beam. The magnetic field generated by the electromagnetic coil confines the electrons and can increase the overall ion current.

The main parameters to operate the FEBIAD ion source are cathode temperature and electric and magnetic field. However, these are indirectly defined by three tunable parameters (see Fig. 1.6):

- The cathode temperature for electron emission is defined by the cathode heating current that causes a temperature generation through the Joule heating effect. At ISAC, typically 290 A are used.
- The electric field for electron extraction is controlled by the voltage difference between anode-cathode and is defined by the anode voltage power supply. At ISAC, typically 200 V are used.
- The magnetic field for electron confinement is controlled by the electric current flowing in the electromagnetic coil. At ISAC, typically 30 A are used.

1.5.1 Historical Development

From a historical point of view, the FEBIAD ion source is the culmination of a series of improvements that date to the very beginning of the ISOL method. The ion source used in the first online separation experiment was a source of the magnetic type [12] that was later known as a Nielsen-type ion source [32]. The Nielsen Ion Source (NIS) consists of a filament that ignites a plasma discharge, from where the ions are extracted, and a magnetic field that confines the electrons created by the filament [33]. The filament of the NIS had a short lifetime and to increase it, modifications were performed to encapsulate the cathode to protect it from harsh vapors [34].

The NIS was further modified by reducing its dimensions to increase the temperature of the walls thus preventing species condensation, and this was coined the Modified Nielsen Ion Source (MNIS) [35]. The MNIS presented higher efficiencies compared to the standard NIS but the operation required stringent control of the gas injected to sustain the plasma discharge. To overcome this stringency, a grid bias to anode voltage was placed in front of the cathode. This final design led to what is known now as the FEBIAD, where the name *Forced Electron Beam* comes from the direct electron extraction due to the grid [3].

In 1975, a transferline combined with a cathode was developed such that both parts were heated with the same electrical circuit [36]. This is the FEBIAD known and used in the ISOL community nowadays. Particularly, this type of FEBIAD was incorporated into the ISAC ion source inventory in 2007 to produce neon and fluorine beams. The ISAC design consisted of a grid with a 75% transparency, boron nitride insulators, and a permanent magnet [37].

1.5.2 Current Status

During the last decade, many aspects of the FEBIAD ion source have been investigated by the ISOL community. While some laboratories have focused on the numerical aspect of a specific part of the FEBIAD, others have found ways to overcome operational challenges. A brief overview follows.

The ISOLDE facility [22] at CERN has standardized their variety of FEBIADs into a single model named VADIS (Versatile Arc Discharge Ion Source), which also implemented the change of grid material from graphite to molybdenum [38]. An experimental campaign was conducted, and the results indicated a saturation of efficiency as a function of cathode temperature from which an operational-based model was proposed [38]:

$$\epsilon = (V * \sigma_{\mathrm{i}} * n_{\mathrm{e}} * n_{\mathrm{n}} * v_{\mathrm{rel}}/n_{\mathrm{n_{in}}}) * f,$$

where V is the anode volume (m^3), σ_{i} is the electron impact ionization cross section (m^2), n_{e} the electron density (m^{-3}), n_{n} the neutral density (m^{-3}), v_{rel} the relative velocity between the neutrals an ions ($\mathrm{m\,s}^{-1}$), $n_{\mathrm{n_{in}}}$ the neutral flux (s^{-1}), and f an experimentally determined extraction efficiency factor. The simulation accompanying the research included, for the first time, space charge effects from the electron beam; however, the magnetic field was neglected despite the experiments showing noteworthy effects [4]. Therefore, the f factor couldn't be predicted for the actual operation nor for any proposed geometrical changes. On the other hand, the VADIS anode has been used as a laser-atom interaction region for RILIS ionization and named VADLIS (Versatile Arc Discharge and Laser Ion source) [39, 40]; however, the operation regime differs from that of a standard FEBIAD operation and no comparison is possible.

The SPES facility [21] in Italy has developed numerical models to characterize the cathode temperature [41]. The research focused on heating reliability and improvement of their model. The experimental results match their simulations, providing confidence in the methodology of their thermo-mechanical studies.

The SPIRAL facility [18] in France has operated a FEBIAD as the principal ion source for producing metallic beams. The developments performed for target and ion source reliability have overcome limitations, such as electrical shorts between anode and cathode and unwanted structural deformations [42].

The BRISOL facility [43] in Beijing is developing a combined FEBIAD with a Surface Ion Source (SIS) [44] for versatile operation with fewer ion source exchanges. The prototype, however, has been only successfully characterized in the SIS mode and no FEBIAD comparison is possible at the moment.

The TRIUMF's ISAC facility [45] in Canada has implemented two FEBIADs based on ISOLDE's MK5 model [36, 38]. One is the standard configuration and the other is the Cold Transfer Line (CTL) configuration. The latter suppresses less volatile elements such as sodium [46]. Despite comprising the same functional elements, the ISAC-FEBIAD previously exhibited offline efficiencies 4 to 5 times lower as compared to ISOLDE.

The upcoming TRIUMF's state-of-the-art ISOL facility ARIEL [19] in Canada foresees the use of both standard and CTL FEBIAD. Because of how different the FEBIAD models are for ISAC and ARIEL (see Fig.1.7), developing an in-depth understanding requires a more fundamental approach complemented by an operational perspective.

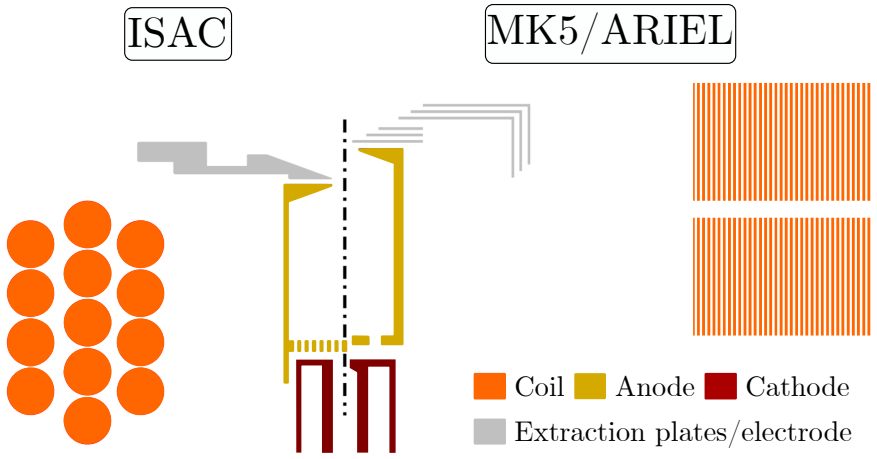

Figure 1.7: Schematic showing the differences between the ISAC and ARIEL FEBIAD ion sources. The anode length, grid openings and coil construction are noticeable different. For instance, the operational range for the ISAC coil current is 0 A to 100 A while for ARIEL is 0 A to 10 A.

Despite the efforts described, a definitive model that explains and predicts ionization and extraction does not exist. Even identical designs do not perform strictly reproducibly, and this suggests an intrinsic difference during operation [47]. Moreover, while electron impact ionization causes the ion generation, the nature of an arc discharge—as the name FEBIAD suggests—, is not entirely defined. With the goal of understanding the cause of the ISAC limitations and to model the FEBIAD ion source, a combined experimental and numerical campaign has been conducted. A numerical model is proposed based on the operational constraints and from fundamental mechanisms. The benefit of a numerical model is three-fold as it allows to gain in-depth knowledge on the source operation, perform simulation-based optimization, and elucidate the ion source driving mechanisms.

Chapter 2

Tools to Characterize the FEBIAD Ion Source

To prepare the different target-and-ion-source units for online operation, specialized offline infrastructure exists at TRIUMF. Typically, the offline operation occurs under restrictive parameters to prevent unit damage. However, these settings limit the parameter space to investigate. To overcome this limitation, dedicated target-and-ion-source units were employed here, and upgrades were performed to the offline infrastructure. This chapter briefly presents the units, the infrastructure, and the computational tools of this study.

2.1 FEBIAD Target-and-Ion-Source Unit

In the Isotope Separator On-Line (ISOL) method, a driver beam impinges on a thick target and the nuclear reaction products effuse into an ion source where they are ionized. Electric fields extract the ions sending them to a dipole electromagnet to separate its components according to their momentum-to-charge ratio to form a Radioactive Ion Beam (RIB).

The crucial part of the ISOL method relies on the Target-and-Ion-Source (TIS) assembly. The assembly consists of a target container filled with the target material coupled to an ion source. Moreover, the assembly is housed inside a water-cooled vessel and the assembly/vessel combination is called the TIS unit (see Fig. 2.1a). The vessel, which acts as a heatshield, also includes feedthroughs to provide a variety of services such as cooling water, gas, voltage, and current (see Fig. 2.1b). Online, the typical lifetime of a TIS unit ranges from 5 to 30 days.

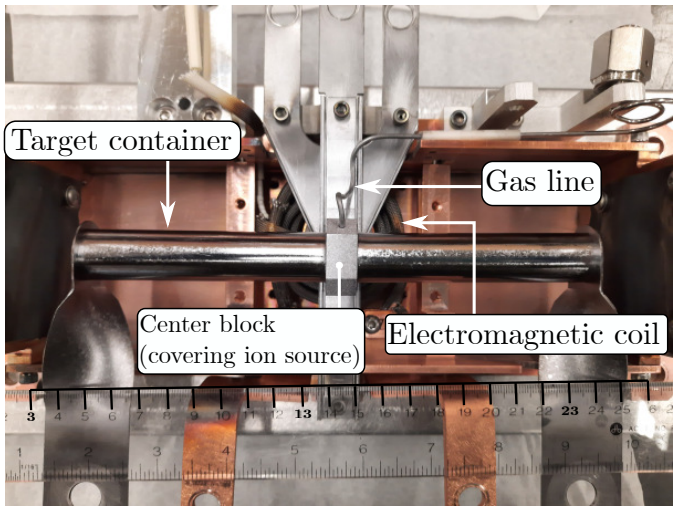

(a) Open TIS unit showing the back of the TIS assembly

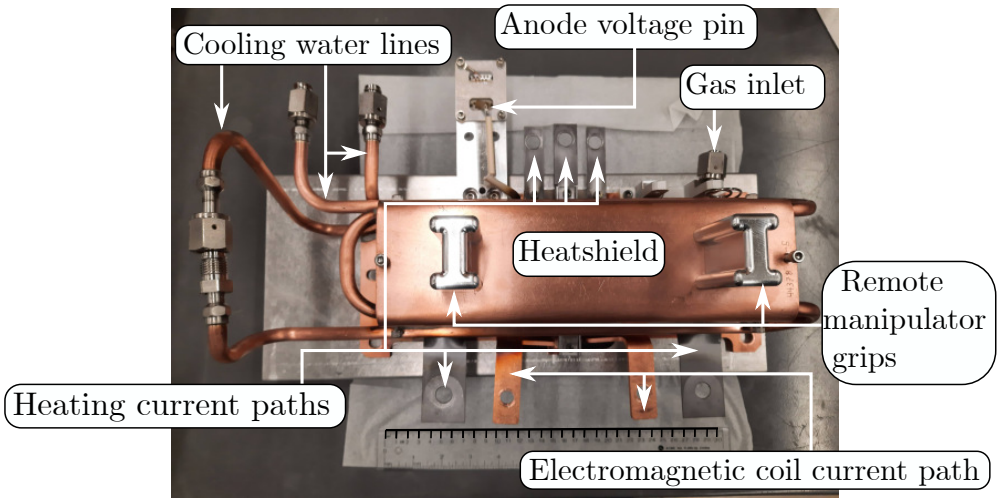

(b) Closed TIS unit

Figure 2.1: Target-and-ion-source unit as used at the ISAC facility. In (a), the vessel lid is removed and the back of the target assembly is visible. The front of the target assembly (with the ion source) is shown in Fig. 2.2a. In (b), the lid is in place and several feedthroughs are indicated. In both pictures, a 30-cm ruler is placed as a fiducial marker.

The FEBIAD TIS assembly comprises specifically a cathode and an anode body of roughly 1 cm in diameter (Fig. 2.2a and 2.2b). The cathode features an emitting face with an area of $\approx 62\,\mathrm{mm}^2$. Moreover, electrical shorts between anode-cathode are prevented by using customized insulators resulting in a total stack-up length of around 3 cm (see Fig. 2.2c). The nominal distance between cathode and grid is 1 mm as can be observed in a CAD model with a quarter cut view (see Fig. 2.3). The CAD model displays both the grid location with respect to the cathode and its small dimension relative to the TIS unit.

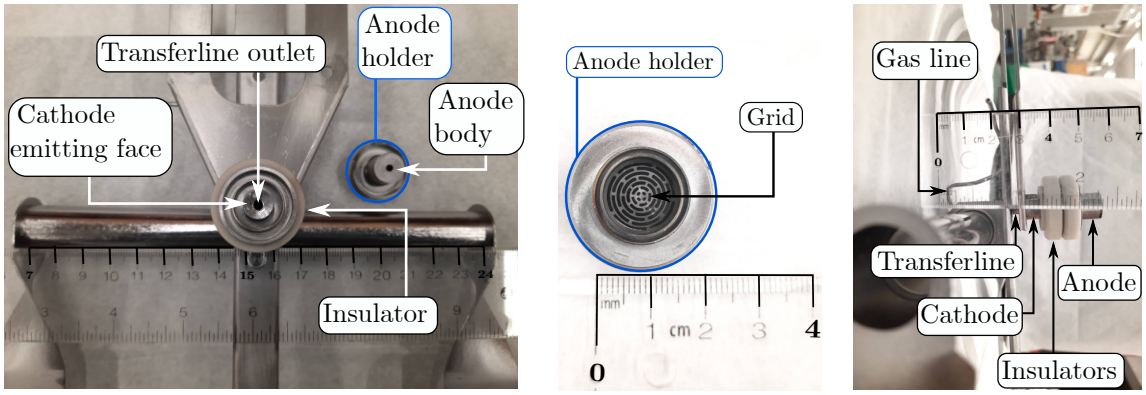

(a) Front TIS assembly

(b) Back of anode showing the grid

(c) Side TIS assembly

Figure 2.2: FEBIAD TIS assembly used at the ISAC facility. (a) FEBIAD front view showing the cathode and anode. (b) Back of the anode showing the intricate pattern of the grid. (c) Side view with all the parts stack-up as in operation. In all pictures, a 30-cm ruler is placed as a fiducial marker.

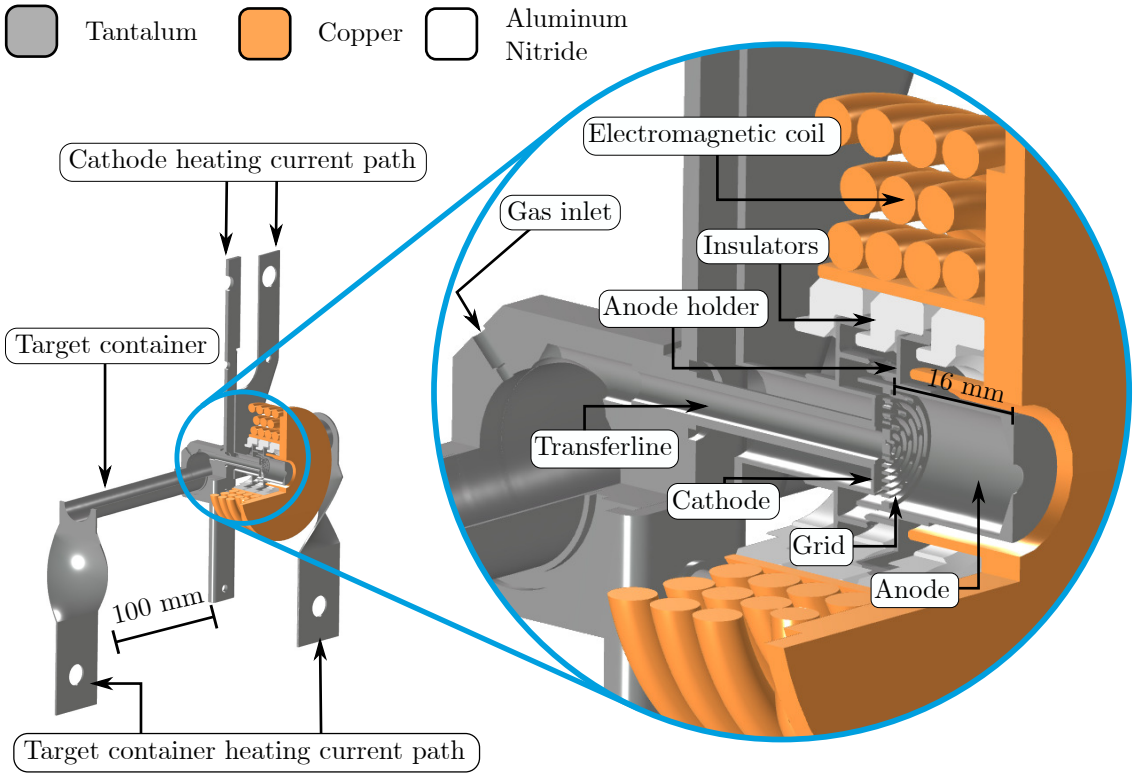

Figure 2.3: Quarter cut view of a FEBIAD TIS assembly. The detail circle shows the main components of the FEBIAD ion source.

2.2 ISAC Test Stand and Evaporator #2

In this thesis, the FEBIAD ion source has been characterized by two offline systems. The first system is the ISAC Test Stand (ISAC TS), a replica of the online target station used to prepare and test the correct function of the TIS units before their installation at the irradiation point [48]. The second system is the ISAC Evaporator #2 (ISAC EVP2), a vacuum furnace typically used for producing and conditioning target materials. A brief description of both systems follows.

The ISAC TS has been used to study the FEBIAD's beam quality, ion beam formation, and ionization efficiency employing existing hardware (see Fig. 2.4). Specifically, the ISAC TS comprises a 5-m long beamline with an electromagnetic mass separator, electrostatic quadrupole lenses, and several beam diagnostics to characterize the ion beam. Depending on the quadrupole voltages employed, the mass resolving power $M/\Delta M$ ranges from 300 to 3000. Moreover, an Allison-type emittance meter [49] is used to measure the emittance and characterize the beam quality. Faraday cups are used to measure the total current from the source, and after mass separation, to measure the ion current of the isotope of interest. Additionally, a gas system switchyard allows injecting a desired gas into the ion source. When combined, the gas injection and the ion current measured, allow computing the ionization efficiency as a function of FEBIAD operational parameters (as in chapter 5).

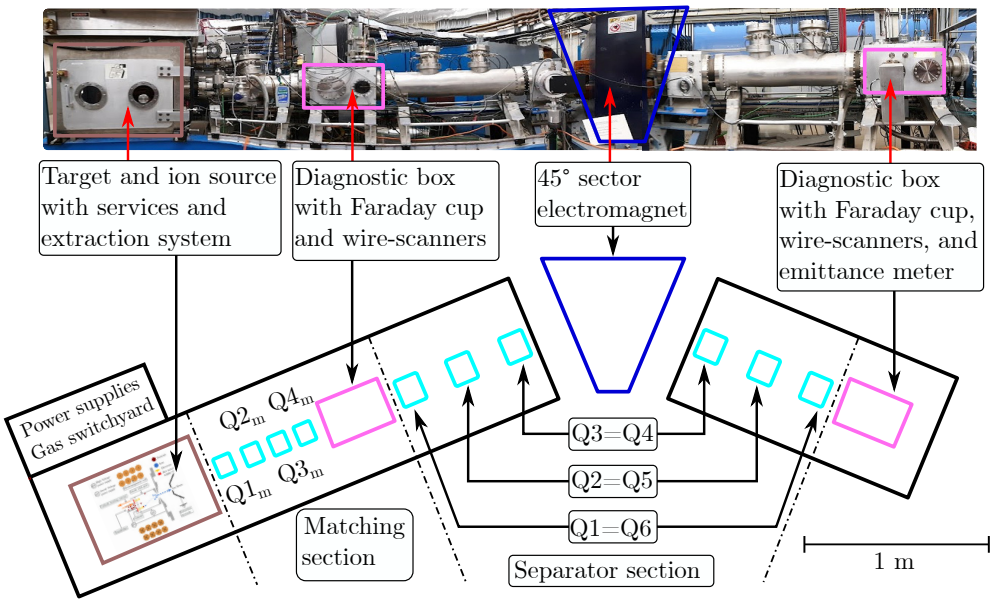

Figure 2.4: ISAC test stand panoramic picture (top) and schematic layout (bottom). The matching section consists of four electrostatics quadrupoles that match the ion beam from the ion source to the separator section. The separator section consists of a 45° sector magnet between two symmetric quadrupole triplets. Two diagnostics boxes provide the hardware necessary to characterize the ion beam.

The ISAC EVP2's heating circuit has been used to study the cathode temperature by means of a non-contact 2-color pyrometer (as in Sec. 4.1). The advantage of the ISAC EVP2 is visual access to the FEBIAD's cathode from a viewport installed on the vacuum chamber. The coupling plate and the heating system inside the vacuum furnace is a replica of the heating components used both at the online stations and the ISAC TS (Fig. 2.5). The heating inside the vacuum furnace employs a constant DC current that makes contact-type measurements challenging. Specifically, the use of thermocouples is prone to chemical reaction with the surface of interest and to bad thermal contact due to the intense cathode temperature. Consequently, non-contact type measurements with a pyrometer were performed with a 2-color pyrometer (METIS 311 by Sensotherm). The pyrometer estimates the temperature by taking a ratio of the power detected at two spectral bands, and effectively cancels the explicit material emissivity dependence. Specifically, the pyrometer has spectral bands at 0.7 µm to 0.9 µm and 0.9 µm to 1.1 µm. However, if the emissivity differs at the spectral bands, a correction factor is required. The factor in the pyrometer employed ranges from 0.8 to 1.2, where 1 corresponds to an identical emissivity at the spectral bands mentioned. Based on preliminary and previous investigations [50], there is a 2% systematic error associated with the knowledge of the correction factor that corresponds to a temperature error of ≈50 °C.

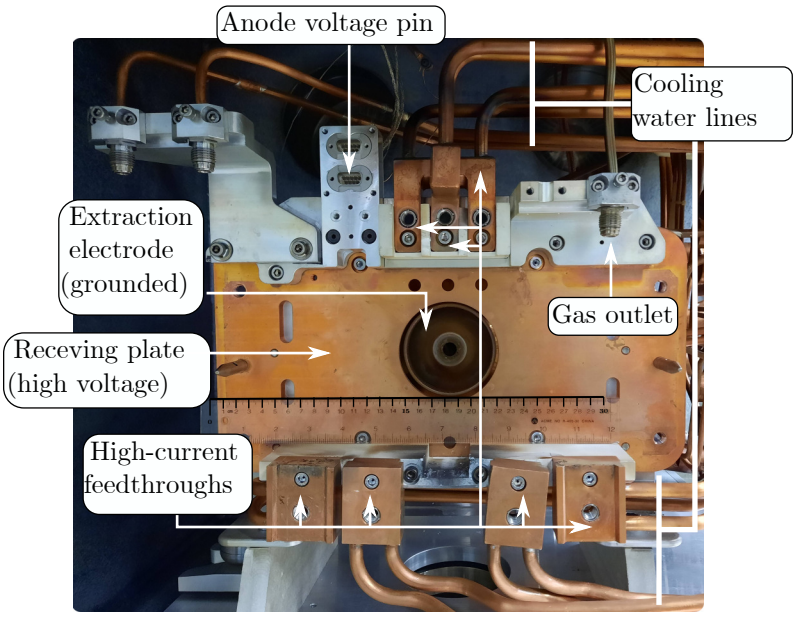

Figure 2.5: Coupling plate to install a TIS unit at the ISAC test stand. The services come from a complex network of water-cooled copper pipes; the ISAC EVP2's heating system is identical minus the ground electrode. Specifically, the ground electrode allows ion beam extraction. During operation, all the components are under vacuum.

2.3 Offline Infrastructure Upgrades

To enable reproducible ionization efficiency measurements at the ISAC TS, the gas injection system has been modified (Fig. 2.6). Previously, an argon gas bottle with a customized glass capillary released gas at a leak rate of 1×10^{-7} mbar L s^{-1}. The gas bottle was connected to a remotely controlled pneumatic switchyard; however, the gas flow started ≈2 m away from the ion source (Fig. 2.6a). During preliminary investigations the gas system was dominated by contaminants that impeded the correct gas analysis. For comparison, the gas system at the online ISAC target station consists of a similar fixed calibrated leak and an almost 20 m pipeline before reaching the TIS unit, which likely causes the same limitations observed at the ISAC TS. To rule out losses and contamination in the ISAC TS gas delivery system, a new system has been developed to inject high-pressure gas into the lines and intercept it with a mechanical calibrated leak ranging from 1×10^{-7} mbar L s^{-1} to 1×10^{-5} mbar L s^{-1}. The new leak is located in the outer part of the heatshield and the molecular flow starts at ≈7 cm away from the TIS assembly (see Fig. 2.6b). With the new system, there is a guaranteed gas injection with practically no contamination nor delivery losses.

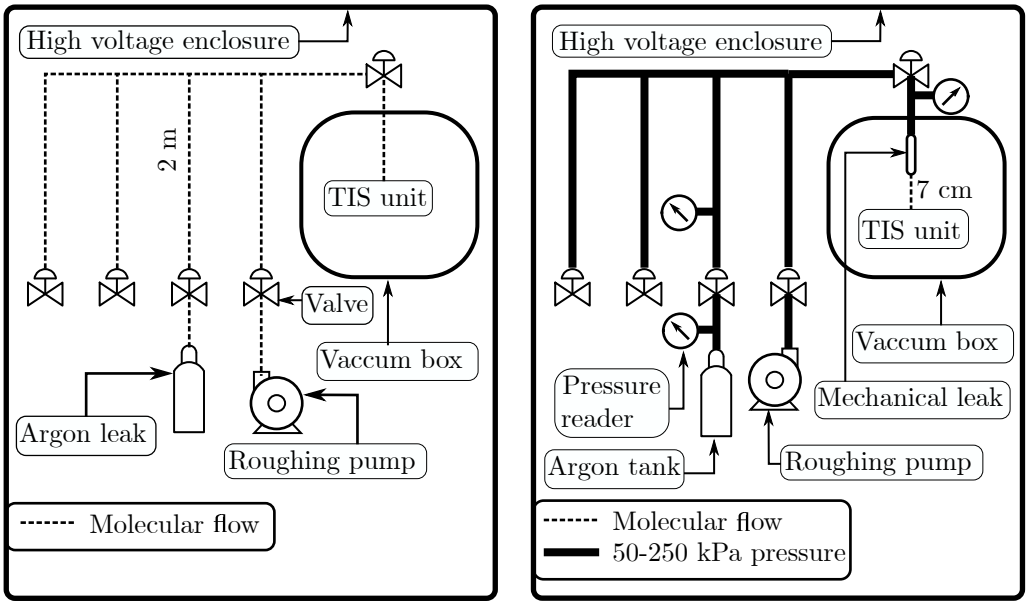

(a) Old gas delivery system

(b) New gas delivery system.

Figure 2.6: FEBIAD gas system upgrades for the ISAC test stand. (a) The gas bottle outlet directly leaks at a constant rate. The molecular flow covers around 2 m of pipes before reaching the ion source. (b) The gas bottle pressurizes the pipes from ≈50 kPa to ≈250 kPa (0.5 bar to 2.5 bar). The high pressure is intercepted by a mechanical leak that leaks at a rate dependent on the upstream pressure.

The main upgrade has been performed for the ISAC TS control system which is operated with the EPICS software [51]. Given the FEBIAD parameter space arising from the different tunable parameters and their range (see Sec. 1.5), systematic measurements were limited due to the time constraints of the experimental apparatus. In addition to the time required to manually explore the parameter space, the options to export the data were limited and the data cleaning required substantial data file manipulation. To overcome this, High Level Application (HLA) scripts [52] have been developed with python to operate the ISAC TS controls system, and in this way, perform automatic measurements and export data in a user-friendly way (as in chapter 5). The automation of the measurements is possible due to a server that handles requests from python code to the EPICS server. The relevant measurements are displayed within a Jupyter notebook [53] as scattered plots and on-the-go data analysis is performed (see Fig. 2.7).

The number of data points taken in a single day of operation has increased ten-fold with the customized data acquisition upgrade. In addition, the measurement time at each data point is consistent throughout the experimental campaign. In this case, and due to the negligible signal variation once a set of parameters is defined, the time average window for the signal is set to 2 s.

The ISAC EVP2 has also been upgraded by installing a voltage power supply in order to have an operational voltage on the anode while investigating the cathode temperature. This upgrade allows both extracting and recording the electron emission current from the cathode (as in Sec. 4.1).

Finally, the online infrastructure was not used, but measurements are foreseen given that the upgrades presented above are planned for implementation at the ISAC online target stations. Specifically, the FEBIAD's HLA implementation is foreseen to be tested by May 2022. The gas upgrade is not planned in the short term as it requires substantial work that interferes with the rigid ISAC RIB schedule. Nevertheless, once both online upgrades are in place, a direct comparison with the offline methodology becomes possible. Moreover, two FEBIAD units are planned to run online in 2022. These sources will be conditioned and operated as presented in this thesis. The measurements planned for mid-June will be reported elsewhere and are expected to serve as a baseline for the radioactive isotope of interest.

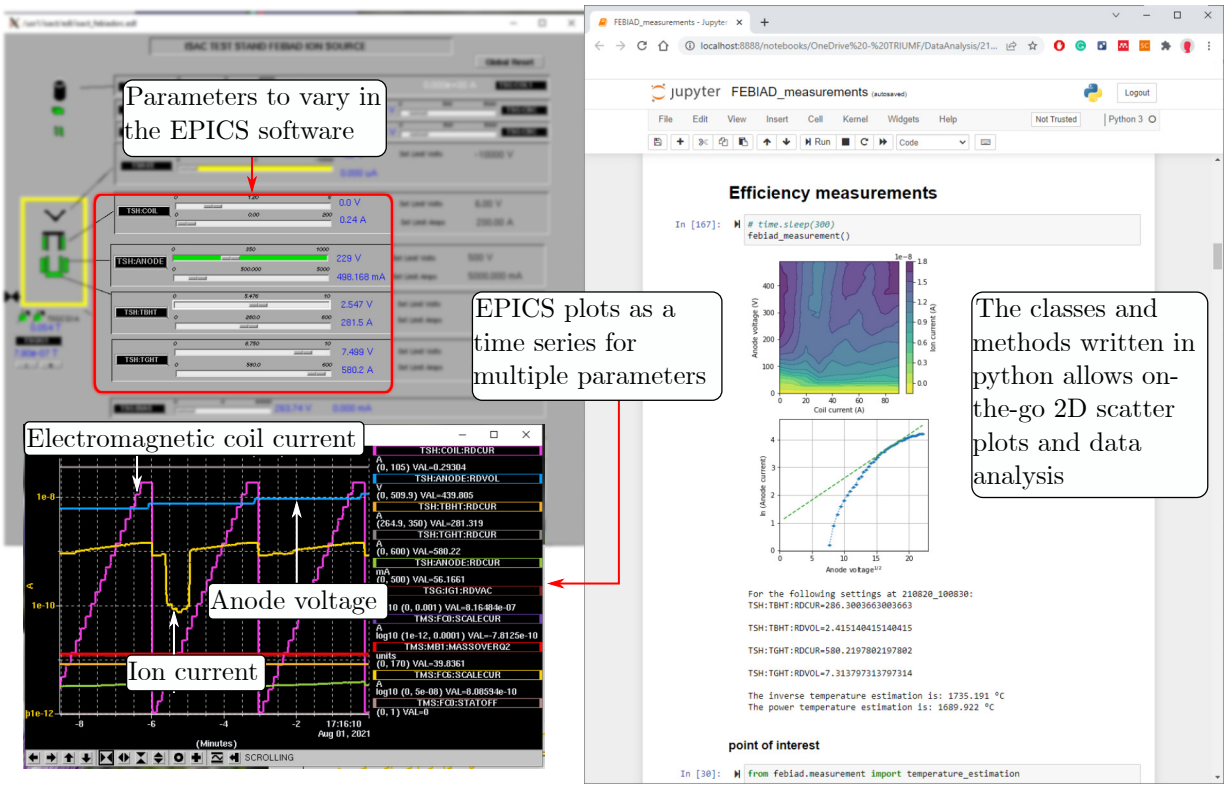

Figure 2.7: Top left window shows the EPICS software and the sliders to manually vary the FEBIAD ion source parameters. Bottom left window shows how EPICS plots the variables as a time series. Right window shows the Jupyter notebook where the classes and methods implemented allow a systematic and automatic variation while plotting and exporting the data. The type of plots and fitting routines are fully customized through python.

2.4 Simulation Softwares

The ISAC TS transport system exhibited limitations in the mass separation resolution, thus hindering a clear distinction of a specific mass of interest. To mitigate this, the in-house code TRANSOPTR [54] has been used to find the optimal values for the electrostatic lenses, also known as beam tune, and provide better mass separation. The code requires the physical characteristics of the transport lenses such as size and separation from other elements in order to return the optimal voltages for the electrostatic lenses. With the new voltage values, the ion beam presents narrow and distinct peaks after separation (see Fig. 2.8a). Combined with the upgraded gas system, the desired mass can be identified and investigated with confidence (see Fig. 2.8b).

The FEBIAD services such as heating currents, gas delivery, and electromagnet current have been characterized by means of numerical simulations performed with the COMSOL multiphysics software [55]. COMSOL is a commercial Finite Element

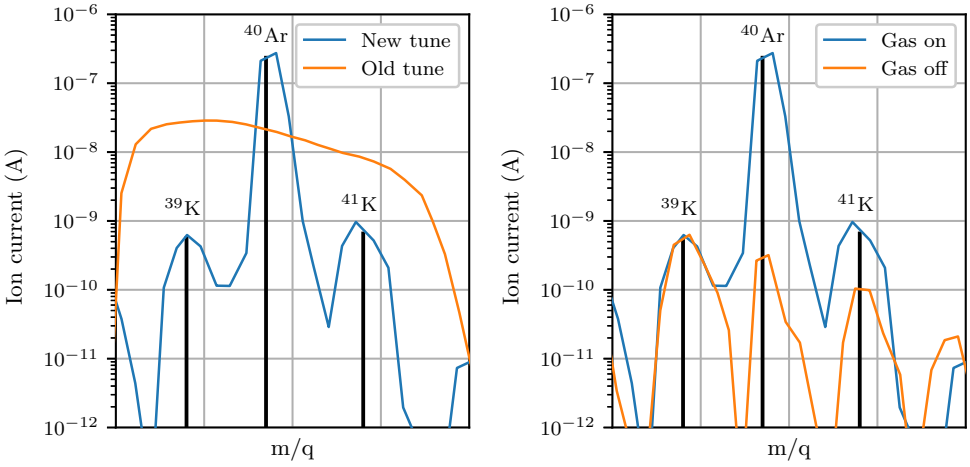

(a) Old tune comparison **(b)** Gas comparison

Figure 2.8: Argon mass peak with its potassium neighbor species. (a) The old tune prevented resolution of the three distinct masses 39, 40, and 41. (b) The combination of optimized beam transport and a new gas injection system allows to properly distinguish the species injected and provides confidence in the methodology. At the moment of the "gas on" measurement, the mass 41 likely present a contribution from aluminum nitride (AlN).

Analysis (FEA) software capable of solving a variety of physical and engineering phenomena such as heat transfer, electrostatics, and plasmas, to name a few. Figure 2.9 shows the desktop application with the different *physics* modules employed in this research. The software further facilitates the use of existing CAD models, increasing the simulation fidelity by using realistic geometry models. For example, in section 4.1, one of the studies performed for the FEBIAD TIS geometry (see Sec. 2.1) consists of solving for the Joule heating, heat transfer, and the consequent structural deformations. This *multiphysics* approach is accomplished by using the corresponding physical equations and imposing the appropriate boundary conditions such as heating electrical currents, cold temperature walls, and fixed constraint walls (see Fig. 2.10). Moreover, the software allows to include imperfect electrical contacts that results in a more accurate temperature profile.

To elucidate the driving mechanisms of the FEBIAD ion source, a numerical ionization model has been developed [6] also with COMSOL multiphysics (see Sec. 3.5). COMSOL is used again due to its versatility for solving physical Partial Differential Equations (PDEs) and Ordinary Differential Equations (ODEs). Furthermore, COMSOL enables analytical expressions, mathematical operations, and derived quantities calculations to be used within the model while it is being solved. The *bottom-up* ap-

proach of the model continuously increased its complexity; however, when comparing the model to experimental data (as in Sec. 5), the choice of not including the plasma module is justified. Nevertheless, the plasma module could be added to study glow and arc discharges if required. Moreover, a variety of software could be used for each aspect of the source; however, a single platform has been chosen because the results of one simulation can be directly used as an input for the next one. For instance, the temperature obtained on a heat transfer study can be used on an electrostatic analysis if desired.

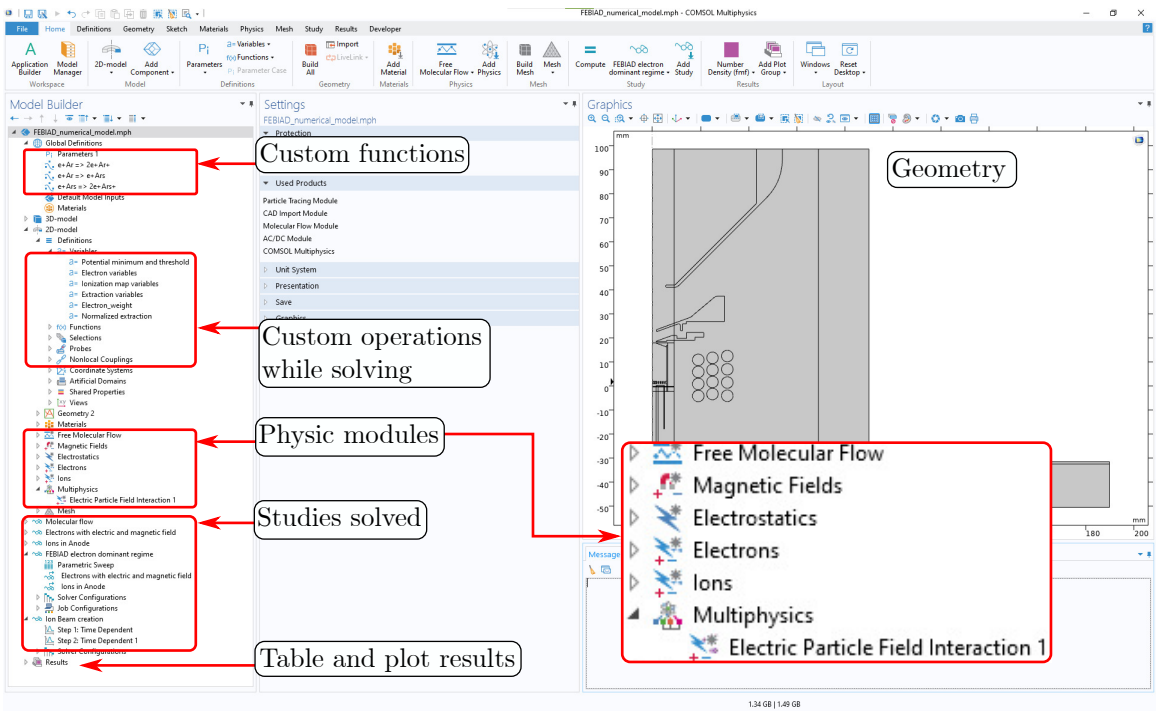

Figure 2.9: COMSOL window desktop showing the different physical modules used as well as the geometry (2D axially symmetric in this case). In the left side under *Model Builder* it is possible to defined parameters, functions, material properties and the type of studies to solve (stationary or time dependent).

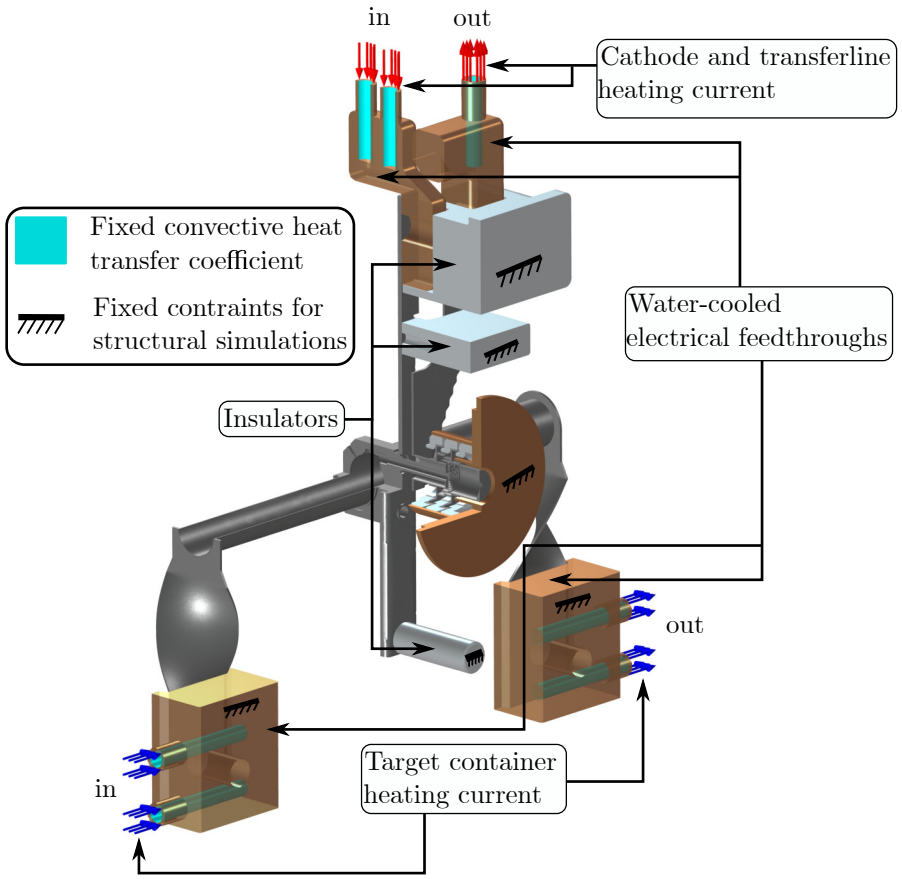

Figure 2.10: Example of boundary conditions imposed to study heat transfer from Joule heating, radiation heat transfer, conductive cooling, and resulting structural deformations. Imperfect electrical contacts exist between the copper feedthroughs and the TIS assembly.

Chapter 3

Ionization Model for the FEBIAD Ion Source: Physical Processes and Their Simulation

In the previous chapter, the FEBIAD has been introduced along with its implementation in the ISAC's Target-and-Ion-Source unit. To study the FEBIAD in detail, a comprehensive simulation package has been developed with the COMSOL multiphysics software [6]. This chapter describes the physical processes in a FEBIAD ion source and relevant equations are presented together with their simulation implementation.

3.1 Thermionic Emission

The electrons driving the FEBIAD ion source are generated through the thermionic emission process. In this process, a heated metal provides the electrons with enough energy to overcome the potential barrier to the vacuum (see Fig. 3.1). The lower the barrier—or material work function—, the higher is the probability of an electron escaping the metal. The electron current emission is described by the Richardson-Dushman equation

$$J_{\mathrm{R}}(T) = A_0 T^2 \mathrm{e}^{\frac{-W}{k_{\mathrm{B}}T}}, \tag{3.1}$$

where A_0 is a material dependent coefficient ($\mathrm{A\,m^{-1}\,K^{-2}}$), T the cathode temperature (K), W the material dependent work function (eV), and k_{B} the Boltzmann constant ($\mathrm{eV\,K^{-1}}$) [56]. With an additional spatial dependence on temperature, $T(x)$, the electron emission $J(T)$ also shows that dependency (see Fig. 3.2).

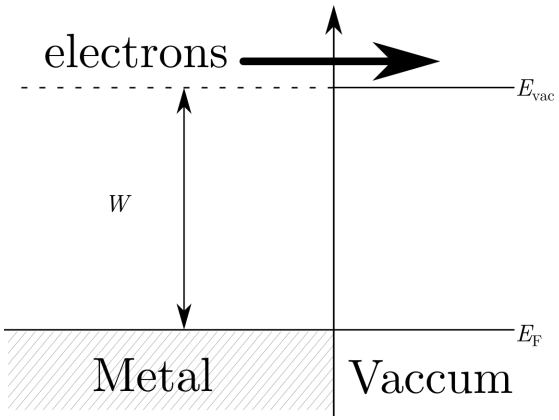

Figure 3.1: Schematic for thermionic emission from a hot metal. The energy required for an electron to escape the Fermi energy level (E_F) into the vacuum is known as the work function (W). Electrons with sufficient energy can overcome the barrier W and are released to the vacuum.

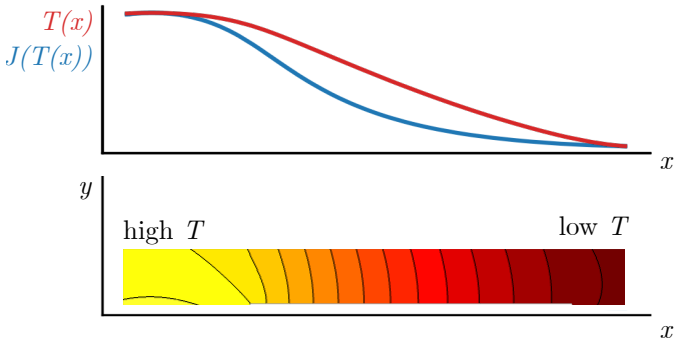

Figure 3.2: Hot metal piece presenting a temperature spatial dependency $T(x)$. By using equation 3.1, higher electron emission corresponds to the location with higher temperature.

The electron emission current further increases by the presence of the electric field between the FEBIAD's cathode and anode. Specifically, the exponential factor in equation 3.1 increases because the electric field causes a potential barrier reduction (see Fig. 3.3). This potential reduction, known as the Schottky effect, translates into a lower work function by

$$\delta W(E) = \sqrt{\frac{e^3 E}{4\pi\epsilon_0}},$$

where e is the elementary charge (C), ϵ_0 the vacuum permittivity ($\mathrm{C\,V^{-1}\,m^{-1}}$), and E the electric field at the cathode ($\mathrm{V\,m^{-1}}$) [57]. The new electron current is described with a correction on equation 3.1:

$$J_S(E,T) = A_0 T^2 \mathrm{e}^{\frac{-W_{\mathrm{eff}}(E)}{k_B T}}, \tag{3.2}$$

where $W_{\text{eff}}(E) = W - \delta W(E)$ is the effective work function. Equation 3.2 shows how increasing E and T increases the electron emission. By assuming a fixed cathode-anode distance d, the effective work function depends only on the voltage V by the relation $E = V/d$ and the electron emission function becomes $J_{\text{S}}(V, T)$.

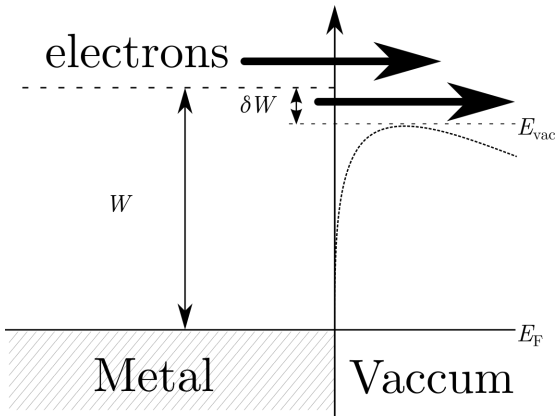

Figure 3.3: Schematic of thermionic emission from a hot metal, including the Schottky effect. The reduced work function allows more electrons to escape the metal.

The Schottky equation can also be expressed as the product of the thermionic emission and an enhancement factor as

$$J_{\text{S}}(V, T) = J_{\text{R}}(T)\, \mathrm{e}^{\frac{\delta W(V)}{k_{\text{B}} T}}, \tag{3.3}$$

$$J_{\text{S}}(V, T) = J_{\text{R}}(T)\, \mathrm{e}^{a(T)\cdot\sqrt{V}}, \tag{3.4}$$

where in the last expression, all the constants and the temperature have combined into $a(T)$. For a voltage of 0 V, the Richardson's equation is recovered. By further taking the natural logarithm, the following expression is obtained:

$$\ln J_{\text{S}}(V, T) = \ln J_{\text{R}}(T) + a(T) \cdot \sqrt{V}. \tag{3.5}$$

With equation 3.5 is possible to experimentally determine, at a constant temperature, the onset of the Schottky regime as it shows a linear dependence with $x = \sqrt{V}$.

3.2 Space Charge Effects

Particles of the same charge repel each other due to electrostatic forces, the so-called space charge effects. For instance, the electrons emitted from the FEBIAD's cathode are subjected to transport limitations as they generate a potential barrier beside the cathode due to the negative charge accumulation. This potential barrier repels

new electrons back to the cathode, reducing the electron current transported. When this occurs, the cathode operates in the so-called space-charge limited regime. The electron current in this regime is described with the Child-Langmuir equation

$$J_{\mathrm{CL}}(V) = \frac{4\epsilon_0}{9}\sqrt{\frac{2e}{m_{\mathrm{e}}}}\frac{V^{3/2}}{d^2}, \tag{3.6}$$

where ϵ_0 is the vacuum permittivity ($\mathrm{C\,V^{-1}\,m^{-1}}$), e the elemental charge (C), m_{e} the electron mass (kg), V the voltage applied between anode and cathode (V), and d the anode-cathode distance (m) [58]. As this regime corresponds to a transport limitation, an increase in temperature does not result in a higher electron current measured.

Space charge effects are also experienced by charged particle beams, consequently affecting the beam local particle density. For example, the electron beam traveling into the FEBIAD's anode volume expands due to the self-induced electrostatic forces. Consequently, the beam both collides with the surrounding anode body walls and decreases the beam current locally. In this case, as either the number of particles increases or the beam energy decreases, the space charge effects become more pronounced.

An extreme consequence of the space charge effects is the electric potential distortion in the FEBIAD's anode volume. In free space, there are no charges and the electric potential is found by solving the Laplace equation

$$\nabla^2 V = 0,$$

where V is the voltage in the anode volume (V); however, with an increasing number of charged particles, the field is found through the Poisson equation

$$\nabla^2 V = \rho/\epsilon_0,$$

where ρ is the charged particle density inside the anode volume ($\mathrm{C\,m^{-3}}$) and ϵ_0 the vacuum permittivity ($\mathrm{C\,V^{-1}\,m^{-1}}$). This last equation becomes relevant as the electron beam can be prevented from expansion with a magnetic field, effectively increasing the charge density locally. This increased charge in the anode volume can generate significant electric potential distortions. In this work it has been assumed that $\rho \approx \rho_{\mathrm{e}}$, that is, the charged particle density corresponds only to the electron density ρ_{e}. Any contribution from the ion density translates into a different electric potential; however, Sec. 5.6 shows evidence for the dominant electron density defining the electric potential.

3.3 Electron Impact Ionization

In a FEBIAD ion source, the principal mechanism for producing ions is the electron impact ionization process. In this process, an electron from the FEBIAD's cathode removes the outermost electron of a neutral element as described by the process cross section. The cross section indicates the probability of the event to occur, and it is a function of the incoming electron energy and element of interest.

Semi-empirical values are typically used for the cross section as they use measured data fitted with a general equation for several elements and electron energies. The ionization process can be described by

$$\sigma_{\mathrm{i}}(E) = a\{1 - b\ \mathrm{e}^{-c(E/P_1-1)}\}\sum_{i=1}^{N} q_i \frac{\ln(E/P_i)}{P_i\ E}, \tag{3.7}$$

where q_i is the number of electrons in the i_{th} orbital, E the incoming electron energy (eV), P_i the ionization potential on the i_{th} orbital (eV), and a ($\mathrm{cm^2eV^2}$), b and c free parameters fitted experimentally [59]. Specifically, the cross section for the argon ionization process

$$\mathrm{e^-} + \mathrm{Ar} \longrightarrow \mathrm{Ar^+} + 2\,\mathrm{e^-}, \tag{3.8}$$

is described with the inclusion of two orbitals ($N = 2$) with ionization energies of $P_1 = 15.8\,\mathrm{eV}$ and $P_2 = 29.2\,\mathrm{eV}$, and with fitting parameters $a = 4.0 \times 10^{-14}\,\mathrm{cm^2eV^2}$, $b = 0.62$, and $c = 0.04$ (see Fig. 3.4).

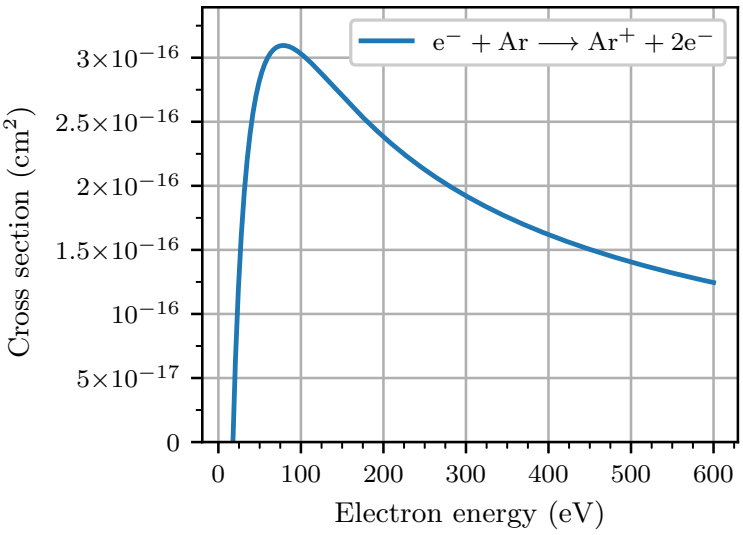

Figure 3.4: Electron impact ionization cross section for argon as a function of electron energy as found from Eq. 3.7. The cross section rises sharply at ≈20 eV and peaks at ≈75 eV.

3.4 Electron Motion in Electric and Magnetic Fields

The motion of the thermally emitted electrons in the FEBIAD's electric and magnetic field is described with the well-known Lorentz force. In the non-relativistic regime, the force is expressed as

$$m\frac{d\vec{v}}{dt} = q(\vec{E} + \vec{v} \times \vec{B}),$$

where m is the particle mass (kg), $\vec{v}$ the incoming charged particle velocity ($\mathrm{m\,s^{-1}}$), q the particle charge (C), $\vec{E}$ ($\mathrm{V\,m^{-1}}$) and $\vec{B}$ (T) the electric and magnetic fields, respectively. From the Lorentz force follows that

$$\frac{dE_\mathrm{k}}{dt} = q\vec{E} \cdot \vec{v}, \tag{3.9}$$

where E_k is the particle energy[1] (eV) that only varies with the electric field. Nevertheless, both the electric and magnetic fields are required to find the equations of motion from the cathode through the grid openings and into the anode volume, as well as the particle energy to describe the electron impact ionization process.

The electric field in a FEBIAD is defined by the boundary conditions of the anode, cathode, and electron beam. The field with no charges is found by solving the Laplace equation

$$\nabla^2 V = 0,$$

and $\vec{E} = -\nabla V$. However, the electron beam current J entering the anode volume has an associated charge density $\rho = J/|\vec{v}|$ from which follows that

$$\rho(\vec{E}) = J(\vec{E}, T)/|\vec{v}| = \begin{cases} J_\mathrm{S}(\vec{E}, T)/|\vec{v}| & \text{Enhanced thermionic emission,} \\ J_\mathrm{CL}(\vec{E})/|\vec{v}| & \text{Space-charge limited emission.} \end{cases}$$

The space charge effects thus distort the electric potential, as found by solving the Poisson equation

$$\nabla^2 V = \nabla \cdot \vec{E} = \rho(\vec{E})/\epsilon_0.$$

Consequently, the solution for the electric field is a combination of the metal boundary conditions and the beam self-induced forces. This combination changes the electron energy, and the value of the corresponding ionization cross section (see Sec. 3.3).

[1] the subscript k is simply used to distinguish it from the electric field symbol.

The magnetic field along the axis in a FEBIAD arises from the electromagnetic coil and is computed by solving the well-known Ampere's law

$$\vec{B} = \mu n I_{\text{coil}} \hat{z},$$

where μ is the vacuum permeability ($\mathrm{T\,m\,A^{-1}}$), n the longitudinal turn density ($\mathrm{m^{-1}}$), and I_{coil} the current flowing in the electromagnet (A). Despite the magnetic field not changing the electron energy (see Eq. 3.9), this field indirectly affects the electron energy when considering the space charge effects. As mentioned in section 3.2, the space charge effects cause beam expansion; however, the magnetic field confines the electrons into a helical orbit, increasing the charge density locally. This confinement arises from the gyromotion of the charged particle which is inversely proportional to the magnetic field. With a larger magnetic field, the helical motion occurs in a smaller radius and conversely, with a smaller magnetic field, the motion is on a larger radius. Indeed, with an increasing magnetic field, the charge density increases locally. Therefore, the charged density becomes a function of the magnetic field:

$$\rho(\vec{E}) \rightarrow \rho(\vec{E}, \vec{B}) \rightarrow J(\vec{E}, \vec{B}),$$

and the space charge effects cause localized variations of electron density and consequently changes in the particle energy that depends on a combination of electric and magnetic fields.

The electron motion inside the FEBIAD's anode volume is then described with the following set of equations

$$m\frac{d\vec{v}}{dt} = q(\vec{E} + \vec{v} \times \vec{B}), \tag{3.10a}$$

$$\nabla \cdot \vec{E} = \rho(\vec{E}, \vec{B})/\epsilon_0, \tag{3.10b}$$

$$\rho(\vec{E}, \vec{B}) = J(\vec{E}, \vec{B})/|\vec{v}|, \tag{3.10c}$$

$$\frac{dE_{\text{k}}}{dt} = q\vec{E} \cdot \vec{v}, \tag{3.10d}$$

$$\vec{v} = \vec{v}(\vec{E}, \vec{B}), \vec{E} = \vec{E}(\vec{r}), \vec{B} = \vec{B}(\vec{r})$$

subjected to the boundary conditions of cathode temperature T, anode voltage V, and electromagnet current I_{coil}. The electric and magnetic fields have been left in vector form to highlight their spatial dependence.

The equation set 3.10 exhibits non-linearity, and consequently, the electron motion and the fields have been solved numerically. Many codes exist to solve charged particle

motion with space charge effects, but most of the codes operate similarly. First, the electric potential is computed without charges in the entire domain studied. Next, the charged particles are released and the self-induced electrostatic forces are computed. With this solution, another iteration for the electric potential is performed including the self-induced forces. Lastly, the steps are repeated until there is no variation in the solution and self-consistency has been achieved. The FEBIAD's magnetic field has been included for the first time to account for its effects on the electron motion.

To model the electron motion, particle tracking simulations are performed considering their interaction with the electric and magnetic fields of the FEBIAD, including the extraction field for the ions. The simulation self-consistently accounts for space charge effects by solving the electric potential and the electron trajectory. A total of 1000 electrons are released and each simulated electron represents a macroparticle such that they add up to a defined initial electron emission current.

The simulated electron trajectories show how the electron beam expands near the middle of the anode volume due to space charge effects (see Fig. 3.5). A plot of the axial electric potential facilitates to note a potential well between 3 mm and 17 mm with a height defined by the value near the outlet of the anode volume. The potential well inside the anode volume has been predicted before, but without including the magnetic field effects [38, 40]. The results in the present research—rather than including a homogeneous magnetic field—, include a realistic magnetic field computed from the real electromagnet geometry. Consequently, each electric field, magnetic field, and electron current combination generates unique electric potential profiles inside the anode volume.

The variables recorded from the electron simulations have been used to compute the ion creation inside the anode volume by using the appropriate electron impact ionization cross section.

3.5 Ionization Model for the FEBIAD Ion Source

The cross section, electron energy, and electron current density combine to create the ionization model that describes the number of ionization events via the ionization rate and ionization rate coefficient. The ionization rate coefficient, k_i ($\mathrm{cm^3\,s^{-1}}$), is expressed as

$$k_\mathrm{i}(E_\mathrm{k}) = \sigma_\mathrm{i}(E_\mathrm{k}) \cdot v_\mathrm{e} \ ,$$

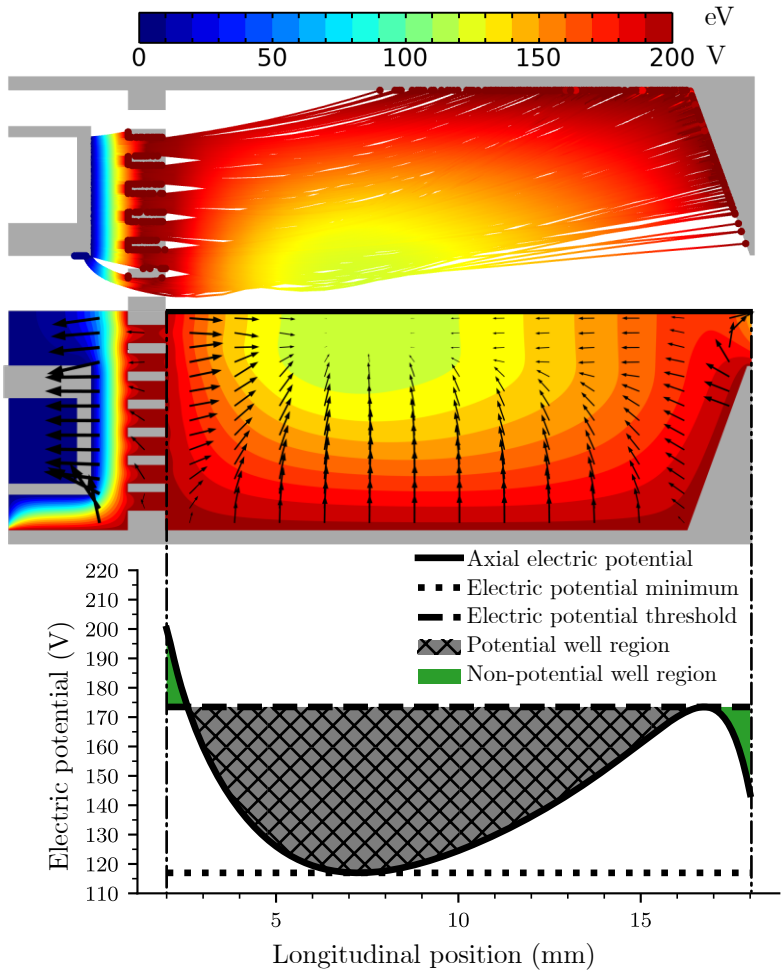

Figure 3.5: Anode cross section showing the electron particle trajectories (top) and electric potential contour plot (middle). The electric field magnitude is proportional to the size of the black arrows which indicate that the highest electric field occurs close to both sides of the grid. The lower line plot shows the axial electric potential. For an applied voltage of 200 V, coil current of 30 A, and electron current of 150 mA, a potential well develops (middle and bottom) due to the space charge effects with a depth of ≈60 V. The potential well decreases the electron energy from 200 eV to ≈120 eV.

where $\sigma_i(E_k)$ is the energy dependent cross (cm^2) and v_e the electron velocity ($m\,s^{-1}$). Because of space charge effects, the velocity v_e depends on J_e and E_k by the changes on magnetic and electric field (see Sec. 3.4). This dependency means that the ionization rate coefficient depends on the conditions imposed by the FEBIAD operational parameters.

The ionization model uses the electron information necessary to compute the

ionization rate per unit volume, $n_{\mathrm{i}}(\mathrm{cm}^{-3}\,\mathrm{s}^{-1})$, as

$$n_{\mathrm{i}} = k_{\mathrm{i}}(E_{\mathrm{k}}) \cdot n_{\mathrm{e}} \cdot n_{\mathrm{n}} = [\sigma_{\mathrm{i}}(E_{\mathrm{k}}) \cdot v_{\mathrm{e}}] \cdot n_{\mathrm{e}}\; n_{\mathrm{n}} = \sigma_{\mathrm{i}}(E_{\mathrm{k}}) \cdot \frac{J_{\mathrm{e}}}{e}\; n_{\mathrm{n}}, \tag{3.11}$$

where $k_{\mathrm{i}}(E_{\mathrm{k}})$ is the energy-dependent ionization rate $(\mathrm{cm}^3\,\mathrm{s}^{-1})$, n_{n} the neutral particle density (cm^{-3}), J_{e} the electron current density $(\mathrm{A\,m}^{-2})$, and e the elemental charge [60]. The analytical, empirical, and simulation results combine to generate a surface plot of the ionization rate per unit volume (see Fig. 3.6). The surface plot indicates the likelihood of a particle being created in a specific location of the anode volume.

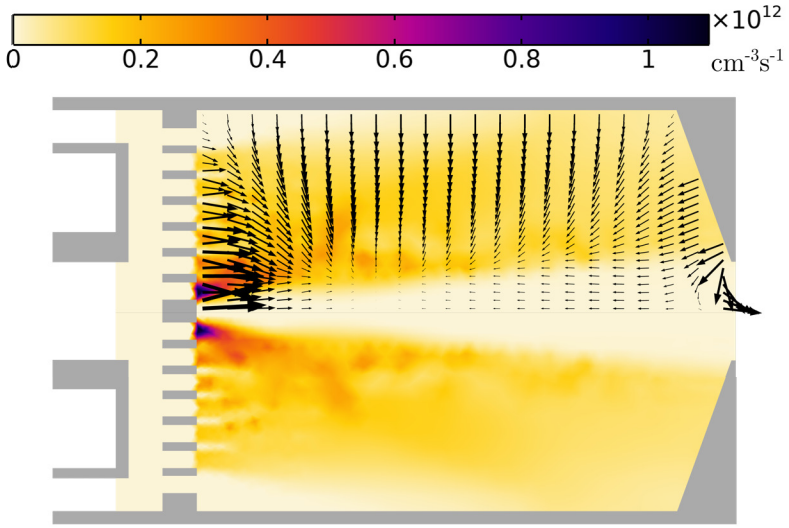

Figure 3.6: Ionization rate per unit volume inside the anode volume as computed from Eq. 3.11 for an applied voltage of 200 V, coil current of 30 A, and electron current of 150 mA. The ionization is higher near the grid as the electron density is higher at this location. This region also matches the place with the highest longitudinal electric field as depicted by the size of the black arrows.

The model has been developed assuming that not all the anode volume contributes equally to the ions generated and measured. One justification is that the electric potential presents a barrier near the exit of the anode (see Fig. 3.5), and only ions with higher energy than the barrier are extracted. For instance, between the grid and the beginning of the potential well there is a voltage difference of ≈25 V that defines the ion initial energy and energy spread (see Fig. 3.5). Moreover, ions generated at the center of the potential well move with thermal velocity only as the electric field is negligible. However, the principal justification is the increased number of ionization

events predicted just beside the grid. With a high longitudinal electric field in this region, ions experience sufficient energy gain to overcome the barrier, so this region is expected to create the ions seen experimentally.

Integrating the ionization rate per unit volume provides a first approximation to the ionization rate as a function of the FEBIAD parameters:

$$I_{n_\mathrm{i}}(E_\mathrm{k}, T, V, I_\mathrm{coil}) = \int_\Omega n_\mathrm{i}\, d\Omega, \tag{3.12}$$

where Ω corresponds to the anode volume (cm^3), which is dominated by the first couple of millimeter besides the grid. Contrary to [5, 38], the spatial ion generation corresponding to the measured ion current arises from the back of the source and not from its center.

The ionization rate per unit volume has been used to initialize the ion positions to perform particle tracking simulation inside the anode volume (see Fig. 3.7). However, as explained previously and to save computational time, the ions released corresponds to those generated outside the potential barrier contour. With this constriction, 10000 macroparticles are initialized following a Maxwellian velocity distribution for a given cathode temperature. The ions are tracked inside the anode volume and some are lost either towards the cathode or the anode walls; however, some remain in the potential well, and the rest reach the anode outlet. Despite releasing the same number of particles on each simulation, the ion extracted ratio is weighted by I_{n_i} to describe the ion extraction as a function of the FEBIAD parameters.

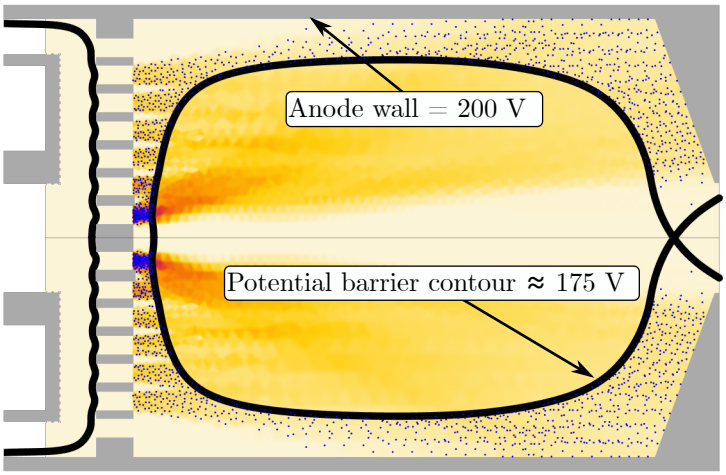

Figure 3.7: Ion initialization and ionization map with equipotential line plot delimiting the potential barrier for the ions. The blue dots corresponds to the ion initialization as computed from the ionization rate per unit volume. Ion created in regions of higher potential compared to the barrier are able to reach the exit of the anode.

The information of the ions reaching the anode outlet has been used to compute the ion beam formation. To study the ion beam, particle tracking simulations have been performed for the ISAC extraction system (see Fig. 3.8). The ions are tracked from the anode outlet to the exit of the ground electrode. A scoring plane is defined at the end of the simulation domain to export the particles' properties for posterior analysis. The plane location is determined based on the negligible variation in the electric potential, which guarantees no changes in beam energy.

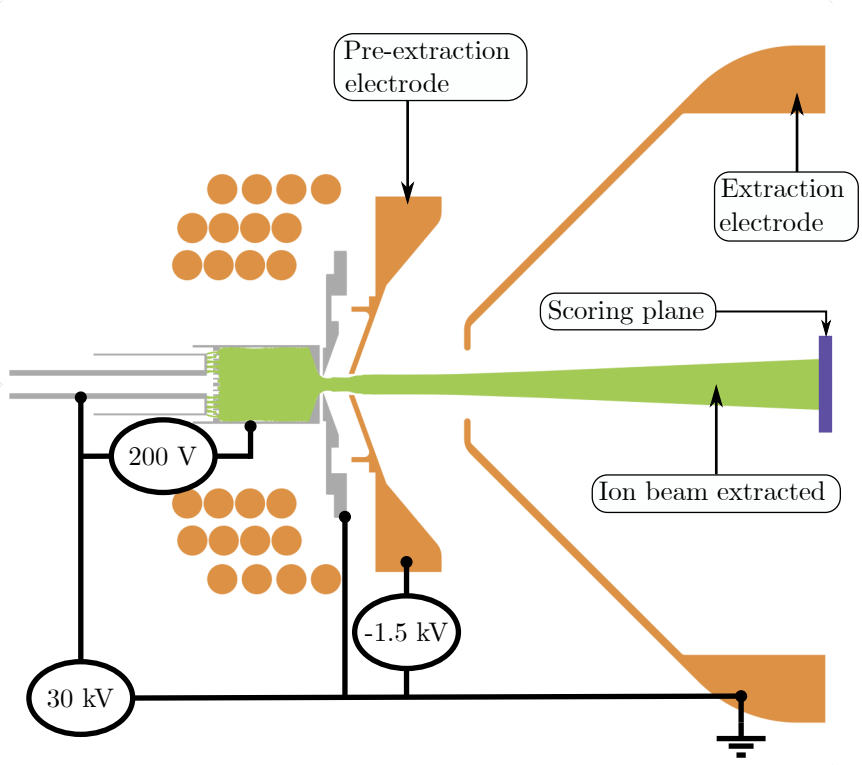

Figure 3.8: Simulated extracted ion beam in the ISAC FEBIAD geometry. Only new items added are labeled, and the typical values used on the electrodes are stated. Some ions are lost to the cathode, others remain inside the anode but the rest is extracted.

Exported beam properties include direct observables that can be compared to measurements such as position, angle with respect to the longitudinal axis, and ion energy. These properties and Eq. 1.1 allow to compute the 4-RMS-emittance from the position and angle distributions (Fig. 3.9). The energy spread is computed with two methods. First, a Gaussian distribution is used to obtain the standard deviation from which the Full Width at Half Maximum (FWHM) is obtained:

$$E_{\mathrm{FWHM}} = 2 \cdot \sqrt{2 \ln 2}\, \sigma_{\mathrm{E}}.$$

The second method computes the 2-Root-Mean-Square (2-RMS) directly from the distribution. Table 3.1 shows the energy spread values obtained with the two methods, but the values only differ by <3 %.

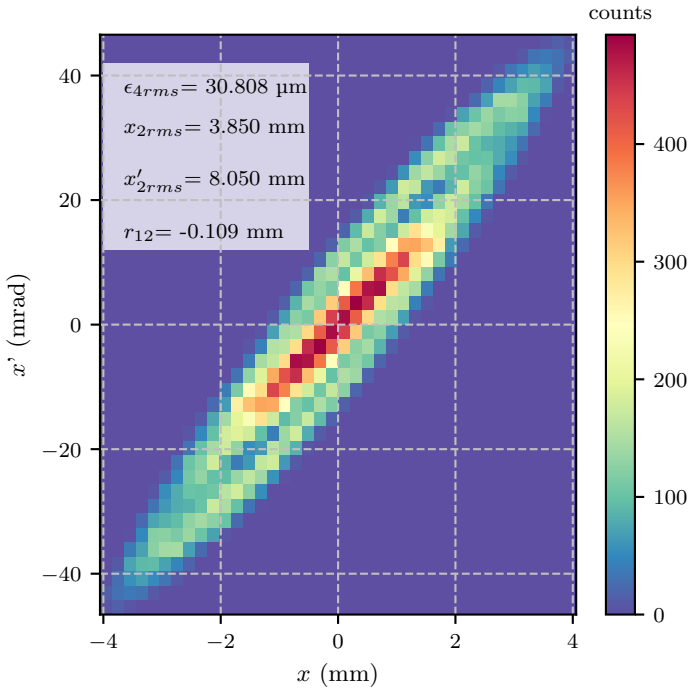

Figure 3.9: Phase space map from simulations. The ion beam extracted is simulated with the following parameters: anode voltage=200 V, coil current=30 A, cathode emitted current=150 mA.

Table 3.1: Energy spread from simulations at nominal operation values with an electron current of 150 mA.

Parameter combination	**Gaussian FWHM (eV)**	**2-RMS (eV)**
(200 V, 30 A)	17.24	16.84

The ions' starting positions and velocities are defined from the ion tracking inside the anode volume; however, the tracking is defined from the electron transport from the cathode into the anode volume. Therefore, the simulated beam properties reflect the processes involved in the ion creation. In this way, observables like relative intensity, energy spread, and emittance can be computed as a function of FEBIAD parameters. Moreover, the simulation approach is similar to an electron impact ion source because the space charge effects are considered only for the electrons [61, 62].

This approach is also referred to as an electron dominant regime. Nevertheless, the simulated quantities from the ionization model are compared to measurements in the following chapters, validating the simulation methodology used to characterize the FEBIAD ion source.

Chapter 4

FEBIAD Operational Parameters Characterization

The FEBIAD ion source is controllable by tunable operational parameters defined by ancillary services. These services were independently characterized by means of experiments and simulations to understand their influence on the FEBIAD ion source operation. This chapter presents the results that help to understand the current status of the ion source and validate the simulation-based characterization of the ancillary services.

4.1 Cathode Temperature

The cathode temperature defines the number of electrons thermally emitted from the cathode surface (see Sec. 3.1). However, the FEBIAD cathode temperature is defined by a controllable cathode heating current (see Sec. 1.5). Therefore, a sufficiently accurate calibration between heating current and cathode temperature is necessary to estimate the maximum electron current available for ionization. To achieve this calibration, simulations with COMSOL (see Sec. 2.4) and measurements with a pyrometer at the ISAC EVP2 (see Sec. 2.2) have been performed. The simulation results are explained prior to the measurements; however, the simulated and measured temperatures are compared in Fig. 4.6, after explaining the measurements.

The simulation characterization of the cathode temperature comprises Joule heating simulations. In this type of simulations, electric currents flow into the Target-and-Ion-Source (TIS) bodies, generating a heat load in the system. Together with the imposed cooling boundary conditions, the program solves for the steady state tem-

perature as a function of the electrical input currents (see Fig. 2.10). The resulting cathode emitting face presents an inhomogeneous temperature for all the simulated electrical currents. The general result shows a maximum temperature at the inner radius that decreases toward the outer radius with a gradient of ≈300 °C (see Fig. 4.1). The simulated cathode average temperature is plotted as a function of heating current and is compared to measurements in Fig. 4.6.

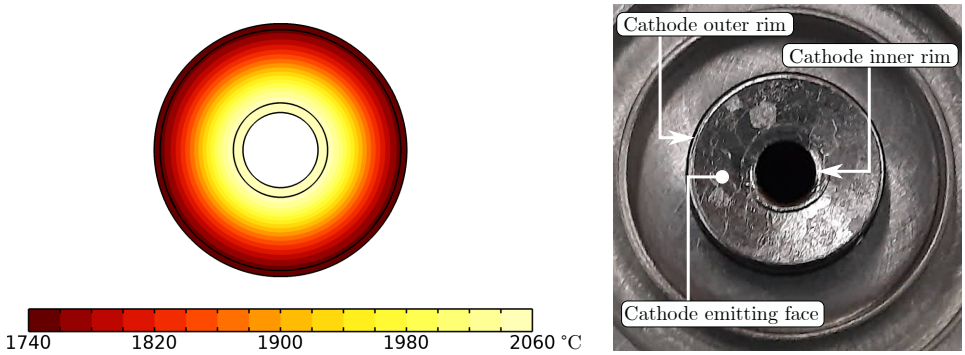

Figure 4.1: Simulated cathode face temperature for an input heating current of 320 A. (a) Despite the different electrical currents used in the simulations, the cathode face generally presents a thermal gradient of ≈300 °C. (b) Photograph of the cathode emitting face as also shown in Fig. 2.2.

To remotely measure the cathode temperature with a pyrometer, a modified TIS unit was used to obtain visual access to the cathode (see Fig. 4.2a). Despite the cathode being partially blocked by the grid, the latter was not removed as it defines an important boundary condition subjected to heat transfer between surfaces. By removing the grid, the temperature measurements wouldn't be consistent with the experimental operation of the ion source. Conversely, and to obtain a better view of the cathode, the anode outlet diameter was increased from 3 mm to ≈8 mm (see Fig. 4.2b and Fig. 4.2c). This modification is located away from the cathode, and the effect on the cathode temperature is negligible as the cold surfaces seen by the cathode are on an almost identical temperature to the anode outlet.

Measurements were performed with a 2-color pyrometer (METIS 311 by Sensotherm, see Sec. 2.2). When observing through the pyrometer viewport, the grid with a colder temperature looks darker with respect to the cathode (Fig. 4.3a). When the pyrometer is optically focused on the cathode-grid, the temperature recorded corresponds to the maximum of the hot body. To access an average cathode temperature, the pyrometer requires defocusing to allow all the light to contribute to the signal detected (Fig. 4.3b). This average temperature is systematically lower by ≈40 °C to

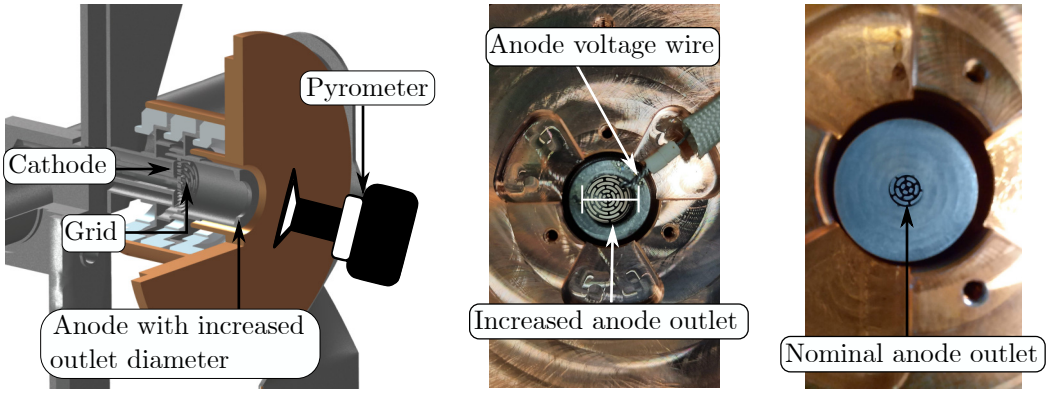

(a) Pyrometer relative location for cathode measurements

(b) Photograph of the modified anode outlet diameter

(c) Photograph of the nominal geometry

Figure 4.2: Modified anode body for cathode temperature measurements. (a) Experimental setup depiction with the pyrometer aiming to the cathode from the anode side. (b) Anode outlet diameter modification to increase the area measured by the pyrometer. The diameter is ≈8 mm. (c) Nominal geometry for comparison purposes. The diameter corresponds to 3 mm.

≈50 °C when compared to the optically focused measurement, but this is expected from the simulations that show a temperature gradient across the cathode face (see Fig. 4.3c). The defocusing, however, causes an unknown error as the grid is still partially resolved by the pyrometer. Nevertheless, the average temperature is closer to the hot temperature inner rim than to the colder outer rim and therefore is expected to better describe the electron emission which occurs over all the cathode face.

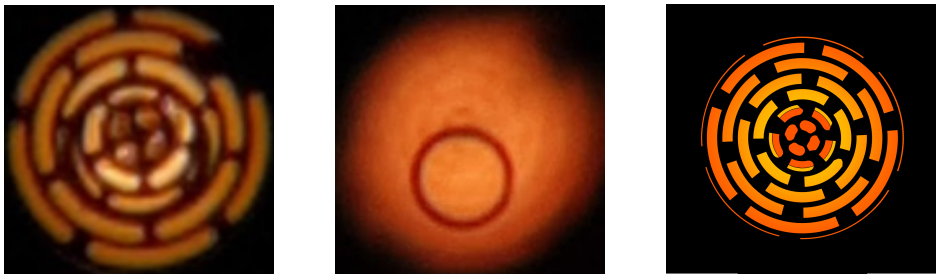

(a) Optically focused pyrometer

(b) Optically defocused pyrometer

(c) Cathode front view from simulations

Figure 4.3: Hot cathode observed through the pyrometer viewport during temperature measurements. (a) An optically focused pyrometer provides the maximum temperature of the bodies on sight. (b) An optically defocused pyrometer provides an average temperature of the bodies on sight. (c) The inner radius of the simulated cathode is hotter than the outer radius. The yellow color indicates a high temperature while the color orange a cold temperature.

The measured temperature has been analyzed assuming that a fraction of the input heating power is emitted as thermal radiation from the cathode surface. Specifically, the cathode surface temperature follows the well-known Stefan-Boltzman law, which indicates that $P \propto T^4$, or more conveniently, that $T^4 \propto P$. The temperature and power relation is fitted with the following equation:

$$y = k_1 \cdot P + k_2,$$

where $y = T^4$ is the surface temperature to the fourth power (K^4), k_1 ($\mathrm{K}^4\,\mathrm{W}^{-1}$) and k_2 (K^4) fitting parameters, and P the electrical input heating power (W). In figure 4.4, the data shows a linear trend as a function of input power with the parameters $k_1 = 3.42 \times 10^{10}\,\mathrm{K}^4\,\mathrm{W}^{-1} \pm 3\,\mathrm{K}^4\,\mathrm{W}^{-1}$ and $k_2 = -3.23 \times 10^{12}\,\mathrm{K}^4 \pm 1933\,\mathrm{K}^4$, validating the methodology employed. From the statistical error δk_i of the estimated parameters, a 90 % Confidence Interval (CI) is also plot as the area between the lines defined by the parameters $k_{i\pm} = k_i \pm 2\delta k_i$. The measured temperatures from the pyrometer are plotted against heating current in Fig. 4.6.

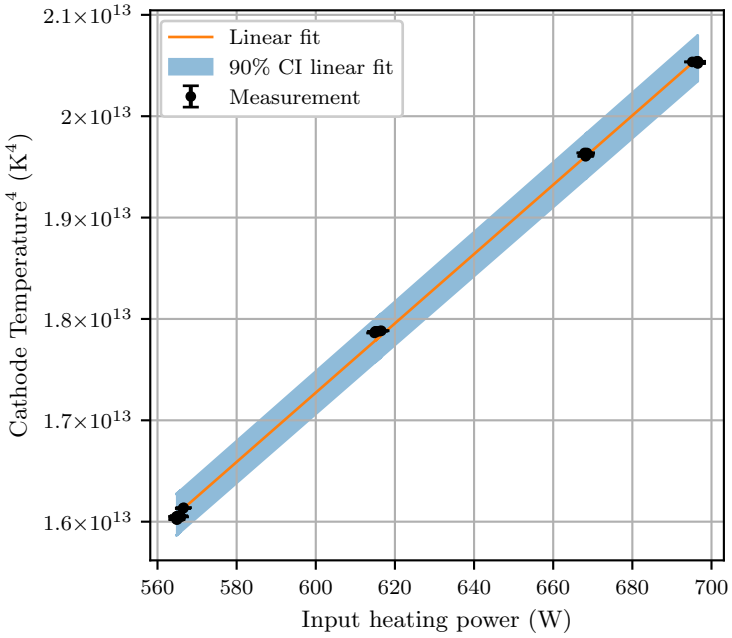

Figure 4.4: Cathode temperature as a function of electrical input heating power. The linear fit describes well the data and serves as a calibration for predicting the temperature in other assemblies by using the fitting parameters $k_1 = 3.42 \times 10^{10}\,\mathrm{K}^4\,\mathrm{W}^{-1} \pm 3\,\mathrm{K}^4\,\mathrm{W}^{-1}$ and $k_2 = -3.23 \times 10^{12}\,\mathrm{K}^4 \pm 1933\,\mathrm{K}^4$ (see text).

The cathode temperature has also been characterized through the recorded electron current, applied voltage, and Schottky equation (Eq. 3.2) with a procedure known as Schottky analysis [57]. In this analysis, a plot of the natural logarithm of the electron current ($\ln J$) against the square root of the voltage applied ($\sqrt{V}$) enables to perform a linear fit to ultimately find the electron current arising from pure thermal effects (see Eq. 3.5). By equating this electron current to Richardson's equation (Eq. 3.1), the temperature can be numerically solved for assuming constant material properties.

To measure the electron current, a voltage sweep was performed for different input heating currents. The electron current was recorded from the readback on the voltage power supply (PS/FL0.7F2.0 by Glassmaan). Using the Schottky analysis, a linear fit is possible by letting $x = \sqrt{V}$ and $y = \ln J_{\mathrm{S}}(x, T)$, with J_{S} being the Schottky enhanced thermionic emission. A Schottky plot exhibits two regimes: for low voltages the space-charge limited regime dominates; but as the voltage increases, as explain in section 3.1, a linear trend indicates the onset of the Schottky regime (see Fig. 4.5).

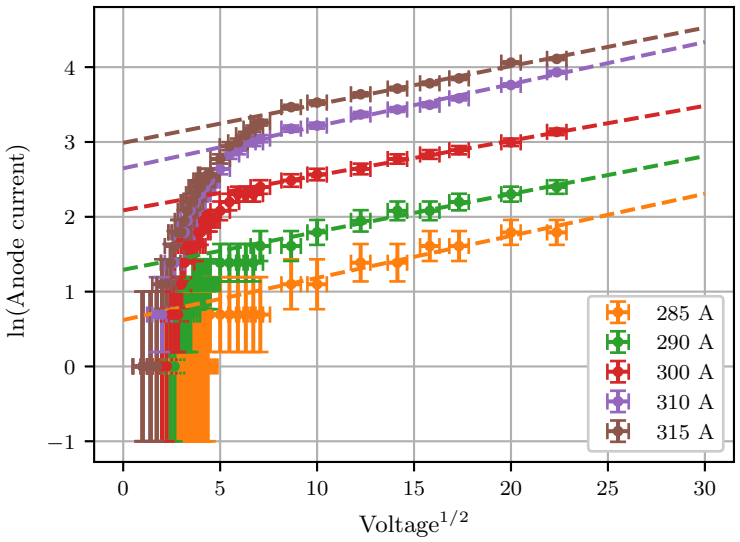

Figure 4.5: Natural logarithm of the electron current as a function of the square root of the applied voltage for several input heating currents. By plotting the mentioned quantities, the cathode temperature is estimated from a Schottky analysis (see text).

The cathode temperature from the Schottky analysis is found by using the fitting equation (see Eq. 3.5)

$$y(x) = a \cdot x + \ln(J_{\mathrm{Rich}}) = a \cdot x + b \tag{4.1}$$

from which follows that for 0 V, that is $x = 0$:

$$y(0) = b \tag{4.2}$$

$$J_{\mathrm{S}}(0, T) = J_{\mathrm{Rich}}(T) = e^{b} \tag{4.3}$$

Equation 4.3 shows that the ordinate value e^{b} (mA) from the projected linear fit provides the electron current arising from pure thermal effects. The temperature is finally found by using Richardson's equation (Eq. 3.1) and the projected electron current.

The Schottky temperature estimation is also plotted in Fig. 4.6 alongside with the pyrometer measurements, and the average simulated temperature. The simulated average temperature shows good agreement for all the heating currents investigated. Specifically, the pyrometer measurement at 290 A is (1688 ± 25) °C and the corresponding simulation is (1653 ± 12) °C, which indicates a underestimation of around ≈35 °C. Nevertheless, the measured temperatures are consistent with each other when considering the experimental errors, validating the methodology established to characterize the temperature as a function of cathode heating current.

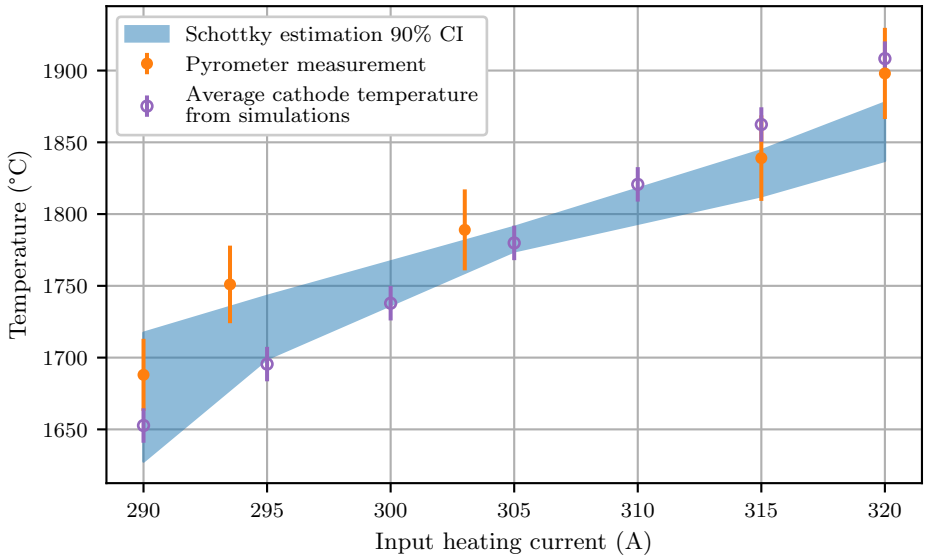

Figure 4.6: Temperature as a function of cathode input heating current. Both direct and indirect measurements are consistent with each other and validate the methodology. The 90% confidence interval corresponds to the calculated temperature from the Schottky estimated parameter b, whereas the error bar on the measured temperature corresponds to the dominant systematic error of the pyrometer (see Sec. 2.2). The error bars on the simulation originate from varying the cooling temperatures on the insulators from 15 °C to 60 °C (see Fig. 2.10).

The theoretical electron current emitted from the cathode is compared both for the thermal regime and Schottky enhanced regime and they show good agreement (see Fig. 4.7). The theoretical estimation uses the direct temperature measurement, cathode area, and material work function as inputs for Eq. 3.1, and the value found is compared with the projected electron current found via Eq. 4.3. The projected electron current is used due to the absence of electron transport at 0 V; even at lower voltages, the measurements are voltage driven as they occur in the space-charge limited regime, and therefore do not describe a thermal emission regime. Moreover, the measured electron current at 500 V is plotted as function of measured temperature. This data set can be described by a reduction of work function of around 3% arising from the the Schottky effect in combination with an increase effective cathode area. The increased area likely arises from the electric field penetration into the transferline: a 1 mm length in the 1.5 mm radius of the transferline, corresponds to $\approx$7 mm^2 for a total area of $\approx$69 mm^2.

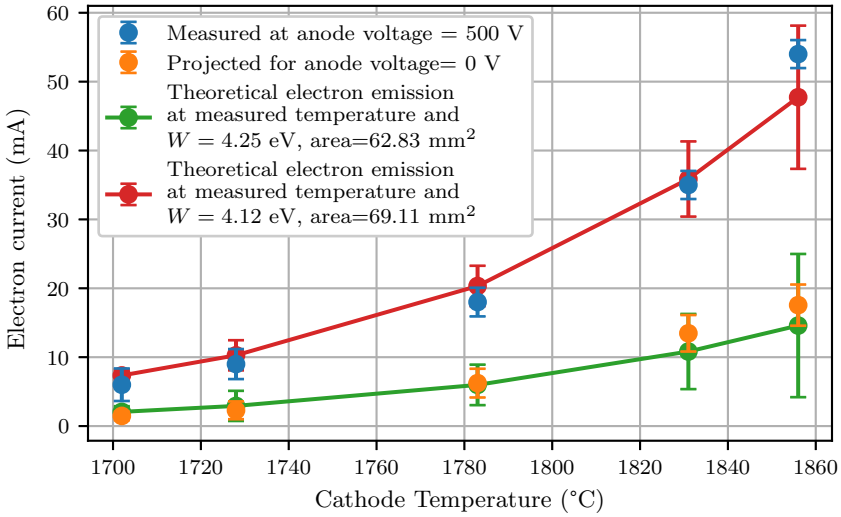

Figure 4.7: Measured and projected electron current as a function of cathode temperature. The theoretical estimation with nominal area and work function matches the projected value. As the electric field increases the effective emission area increases and the work function decreases due to the Schottky effect.

The temperature calibration curves presented in this section are expected to vary during online operations. These differences arise from the power deposition of the driver beam into the target material, which impose a different heat load into the TIS assembly. Consequently, the offline cathode temperature against electron current will not describe the online operation. However, the relation between voltage and electron current reading can provide a better temperature estimate (as in Fig. 4.5). By measuring the V-I_e relation both offline and online, a proper temperature comparison will be possible.

4.1.1 Cathode Emission Changes Due to Thermal Stress Effects

The cathode temperature simulations include the entire system and allow a general assessment of the intense heating and thermal stresses associated (Fig. 4.8). For all the simulated heating currents, a hot spot develops at ≈10 mm inside the transferline, which exhibit a temperature gradient of ≈300 °C to the cathode inner rim. The temperature gradients cause thermal stresses in most of the TIS assembly and deformations are expected to occur.

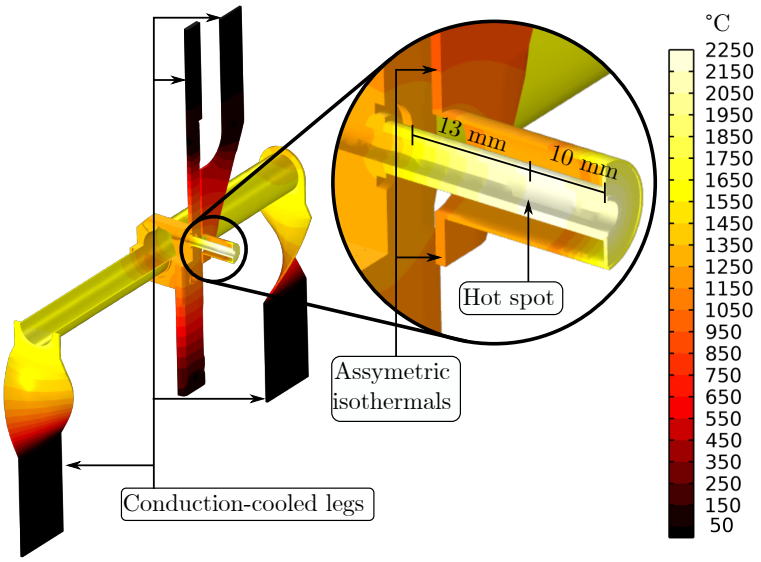

Figure 4.8: Quarter cross section view of the simulated FEBIAD TIS temperature for a 320 A cathode heating current. In the transferline tube, a hot spot is located at ≈10 mm and there is a difference of ≈300 °C between the hotspot and the cathode inner radius.

Structural simulations were performed with COMSOL to determine the thermal induced deformations and their consequence on the cathode integrity (see Fig. 2.10). During the experimental campaigns, thermo-mechanical limitations were observed and they can be understood from simulations. The simulations consist of an iterative computation that solve the Joule heating effect and the deformation arising from thermally-induced stresses. The deformation obtained qualitative agree with the experimentally observed deformations (see Fig. 4.9).

The structural analysis further indicates that the deformations observed on the cathode arise due to the way it is constructed (Fig. 4.10). Because the cathode return path is not radially symmetric, an asymmetric heating induces asymmetrical thermal stresses that cause a downward expansion. Additionally, the transferline exhibits longitudinal deformation mainly caused by the hotspot inside of it. The transferline is joined to the target and cathode, however, the latter components are not prevented

to displace longitudinally. Consequently, the transferline expands in two directions; first by pushing the planar cathode towards the anode and second by pushing the target container backwards.

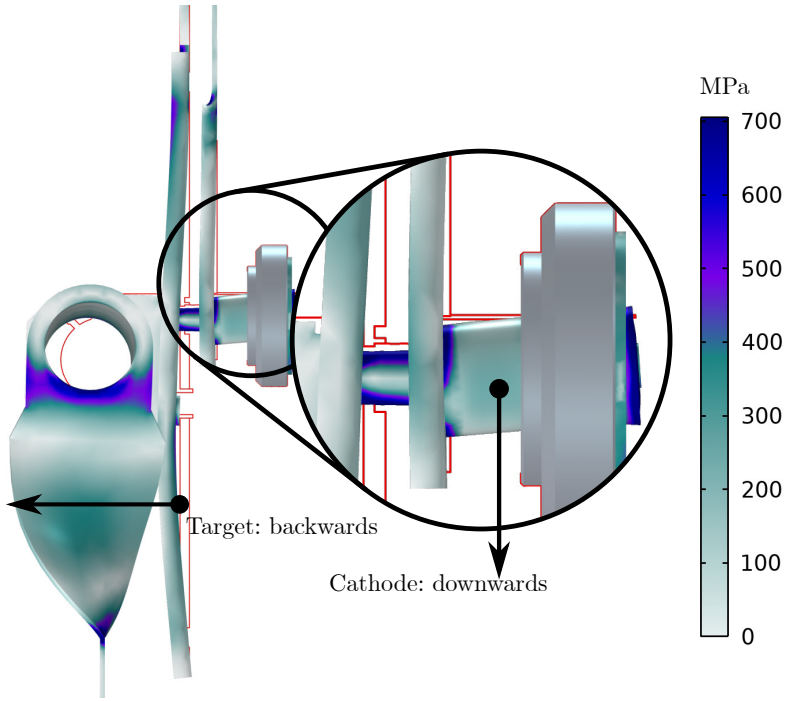

(a) Simulation

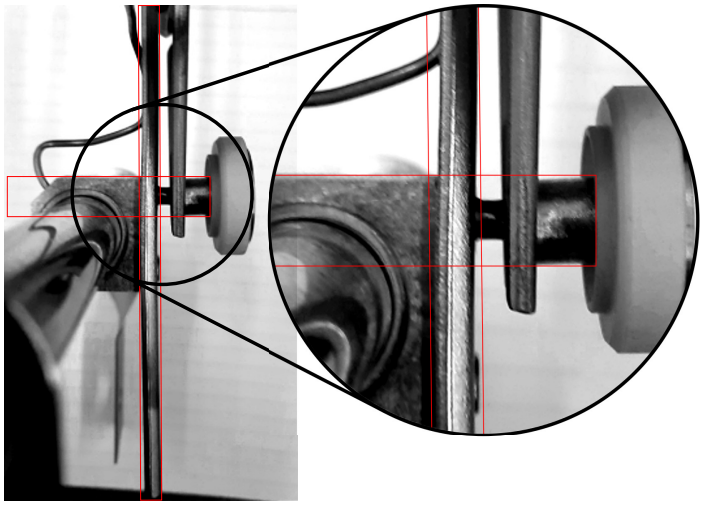

(b) System after heating

Figure 4.9: Structural simulation and experimental comparison. (a) Thermally-induced deflections from simulations. Deformations are exaggerated by a factor of 5 to better observe them. The thin red lines outline the nominal geometry. (b) System observed after heating experiments. The red squares help to guide the eye to distinguished the relative deformation from the nominal edges as also shown in the simulation.

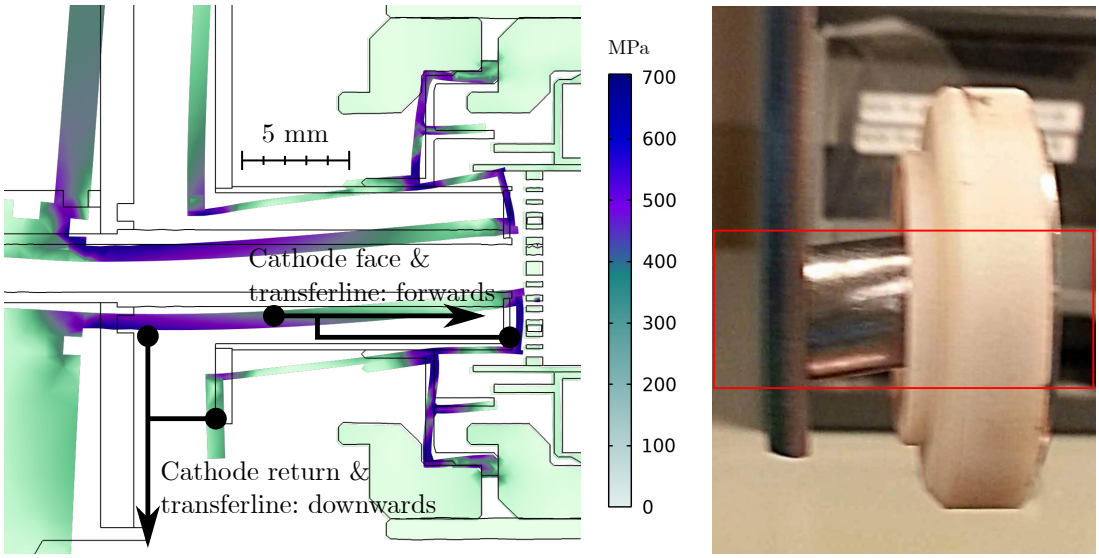

(a) Simulated deformed cathode **(b)** Observed deformed cathode

Figure 4.10: Deformations predicted from simulation and observed after the temperature characterization campaign. (a) Cross section of the thermally-induced stresses and resulting deformations. The transferline expands forwards and move downwards causing the cathode to get closer the grid. The deformations are exaggerated by a factor of 5 to better visualize the effect. The thin black lines outline the nominal geometry. (b) The cathode return is severely deformed as predicted from simulations. The red lines are in place to help guide the eye.

The intense heating also results in a broken transferline at a point near the hotspot predicted from simulations (see Fig. 4.11a). The observed breaking point and the hotspot differ by ≈1 mm. In this case, the thermal expansion caused necking at the hotspot, ultimately breaking the transferline in two while also causing the cathode to touch the grid (see Figs. 4.11b and 4.11c). During operation, an electrical short developed indicating a contact between anode and cathode. This contact specifically developed between the grid and cathode as they were found stuck together during a post-failure inspection. The deformations and failure points match the thermal-structural simulation predictions and provide confidence in the model.

The intense heating also causes increased electron current that ultimately impinges onto the grid with catastrophic consequences. Two FEBIAD assemblies investigated exhibited the same type of melted grid failure. At the cathode heating current of 336 A that corresponds to ≈1940 °C, a voltage sweep causes the grid to start glowing (see Fig. 4.12a). The change in brightness is an indication of the electron beam power deposition which ultimately causes the grid to fail (see Fig. 4.12b).

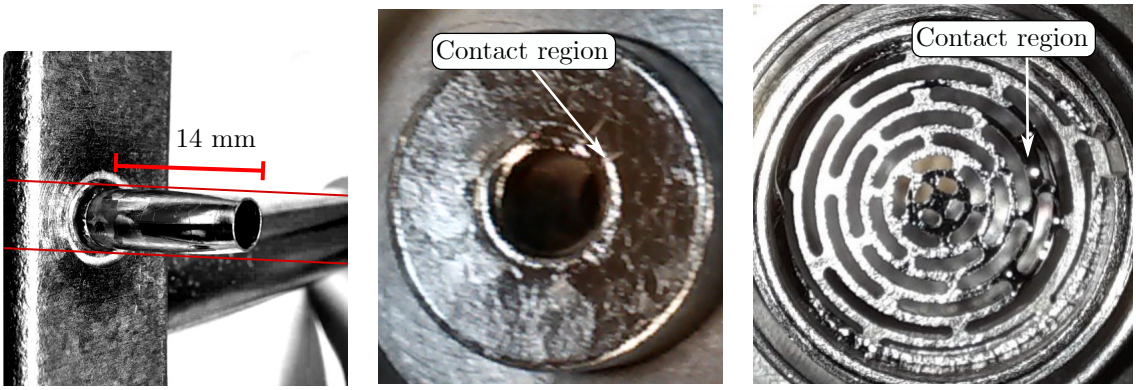

(a) Transferline broken **(b)** Cathode face **(c)** Grid partially melted

Figure 4.11: Thermo-mechanical failures found during thermal investigations. (a) The hot temperature not only caused an expansion but also caused the transfer line to break via necking (red lines help guide the eye). The hot spot from simulation and the location of the melting point differ ≈1 mm. (b)–(c) The expanded transferline caused the cathode to touch the grid causing partial melting.

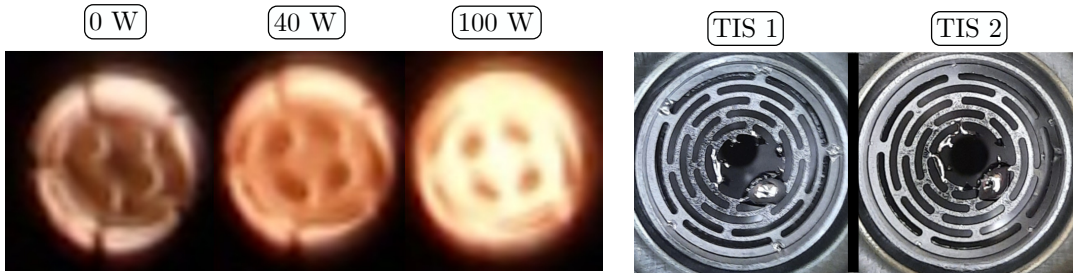

(a) Grid glowing due to different power deposition **(b)** The remarkably similar melted grids due to excesive heating

Figure 4.12: Thermo-mechanical failures observed during ionization efficiency investigations. (a) The grid glows as a consequence of the electron power deposition. (b) The increased temperature causes the center of the grid to melt.

To model the grid heating and to account for the voltage dependence observed, particle tracking simulations were performed to estimate the power deposition of the electrons into the grid (see Fig. 4.13a). The power deposited is calculated as $P_e = I_e \cdot E$, with P_e being the power deposited (W), I_e the measured electron current (A), and E is the energy of the electron (eV). The power found is coupled with thermal simulations and shows that for a voltage of 500 V and electron current of 150 mA, the center of the grid exceeds the melting point of tantalum (3017 °C [63]). This is because the grid design presents small thermal conductance paths that limit the heat transfer to the colder outer rim. Simulation results further indicate that in order to cause sufficient power deposition at the grid center, at least half of the electron

current measured must come from the cathode inner rim and the first millimeter of the transferline. This two-part contribution likely arises from the temperature gradient at the cathode face (see Fig. 4.1). By using Richardson's equation (Eq. 3.1) as explained in Sec. 3.1, the electron emission density presents a higher value at the inner cathode rim compared to the colder outer rim (see Fig 4.13b).

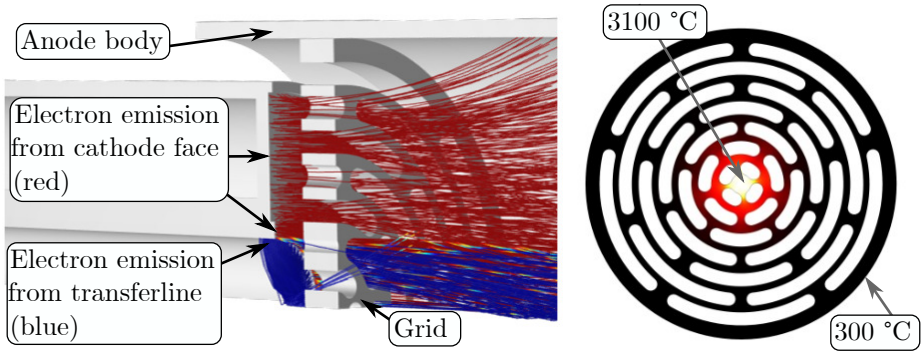

(a) Electron tracking and grid temperature

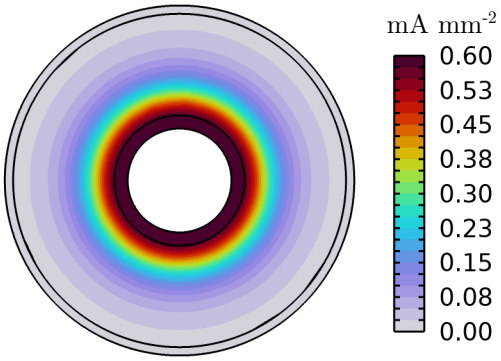

(b) Electron current density at the cathode

Figure 4.13: Grid temperature simulation from electron power deposition. (a) The electron trajectories are divided into two contributions to match the melting temperature of the tantalum grid. (b) The two-part contribution matches the spatially distributed electron current density due to the cathode temperature gradient observed in Fig. 4.1.

The deformations captured by the simulations are not only relevant from the reliability point of view but also for the ionization process itself. Section 4.1 shows the Schottky dependence on electric field through $E = V/d$. If the distance reduces as a consequence of an increased temperature, the electron emission current increases due to both effects as T^2 and $e^{\sqrt{E}}$ (Sec. 3.1), while the transport limit increases due to the factor d^{-2} (Sec. 3.2).

4.2 Magnetic Field

The magnetic field causes electron confinement that, in turn, controls the overall ion current without affecting the geometry of the cathode nor the anode body—when comparing to the cathode heating current in Sec. 4.1.1. Therefore, a combined simulation and experimental campaign was performed to characterize the impact of the magnetic field on the FEBIAD ion source. To generate the magnetic field, an electromagnetic coil made of a copper wire is wound into a three-layer cylindrical shape (Figs. 4.14a and 4.14b), and an electrical current is applied. The simulations were performed with COMSOL and the measurements were taken at the ISAC TS (see Fig. 4.14c). For the measurements with a Hall probe, a modified TIS was used for which the target, cathode, and anode were removed.

(a) CAD model of ideal coil geometry

(b) Photograph of assembled coil with insulator jacket

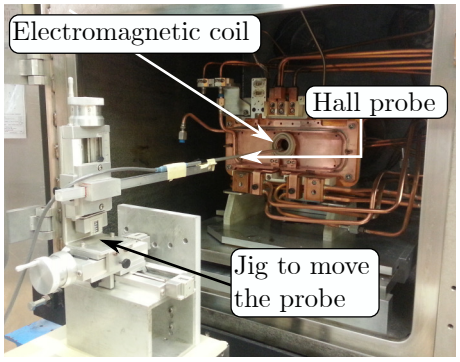

(c) Experimental setup to measure the magnetic field

Figure 4.14: FEBIAD electromagnetic coil geometry. (a) Ideal electromagnet for the magnetic field simulations. (b) Real coil manually wound. The manual construction of the coil causes variations from unit to unit. A silica insulator jacket wraps the wire to prevent electrical shorts between windings. (b) For the experiment, a jig allows sub-millimeter control on the the Hall probe displacement.

Magnetic field simulations were performed with an ideal geometry and they show a maximum axial field at ≈1 mm in front the grid (see Fig. 4.15). The simulations consist of a constant current passing through the coil geometry and Ampere's law is solved in every point of the simulated domain. Several currents were used in the simulations but only one is presented. This is because the magnetic field was found to scale linearly with current as expected from Ampere's law (see Sec. 3.5).

The magnetic field was characterized with a Hall probe (XM11 by LakeShore) and the result is compared to simulations (see Fig. 4.15). Because the electromagnet

generates a dominant axial component, an axial hall probe was used to measure the field longitudinally. For a 70 A electrical current, the resulting magnetic field shows a discrepancy towards the anode outlet that likely arises from the ideal geometry employed in the simulation. As can be observed in Figs. 4.14a and 4.14b, the coil manual construction generates an oval shape and tighter windings compared to the CAD model. Nevertheless, the maximum magnetic field measured in the ISAC geometry is 1 mm in front of the grid and decreases toward the anode outlet as predicted in the simulations. Despite using an ideal geometry for the simulations, the location and magnitude of the maximum simulated magnetic field shows good agreement with the measured values. This provides confidence into modeling different electromagnet geometries.

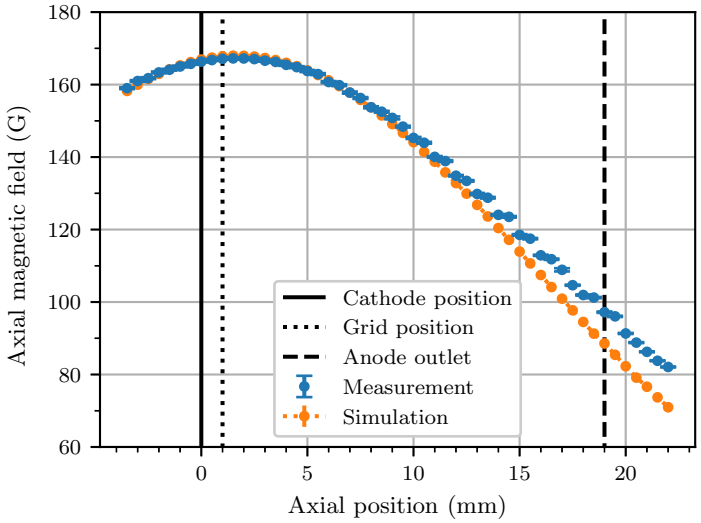

Figure 4.15: Axial magnetic field measurement for an electromagnet current of 70 A. The black lines indicate the location of the FEBIAD components. The discrepancy between measurement and simulation is noticeable downstream and likely arises due to the ideal electromagnet geometry used in the simulations.

4.3 Gas Leak Rate

The new gas system allows direct gas injection into the TIS via a calibrated leak (Sec. 2.3). This development overcomes the old system limitations consisting of no reproducible injection rate nor pure gas injection into the source. In the new paradigm, the gas enters at different rates depending on the upstream pressure. With the knowledge of the neutral injection rate, it is possible to compute the ionization efficiency.

Therefore, the leak rate was characterized prior to the ionization efficiency measurement campaign.

The leak rate was measured with a helium mass spectrometer (979 by Varian) at different helium upstream pressure (see Fig. 4.16). A linear dependency is found between the helium leak rate and upstream pressure for the measured range. However, the gas used in this research is argon and therefore a conversion factor is required. The molecular flow rate Q ($\mathrm{mbar\,L\,s^{-1}}$) is proportional to the gas kinetic mean velocity $\bar{v} = \sqrt{8k_\mathrm{B}T/\pi m}$ ($\mathrm{m\,s^{-1}}$), from which follows that $Q \propto \sqrt{T/m}$. For a system operating at the same temperature, the relation between the helium leak rate Q_He and the desired species Q_ds is therefore given by the relation

$$\frac{Q_\mathrm{He}}{Q_\mathrm{ds}} = \frac{\sqrt{m_\mathrm{ds}}}{\sqrt{m_\mathrm{He}}},$$

With argon ($m = 40$) as the gas injected into the source, the values from Fig. 4.16 have to be multiplied by the above conversion factor.

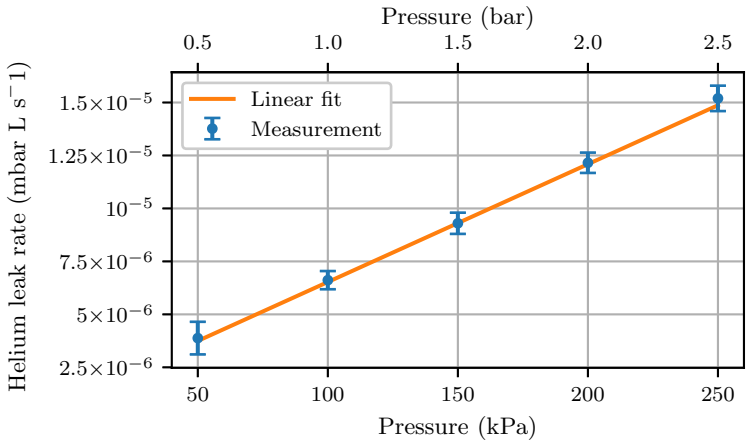

Figure 4.16: Leak rate dependency on upstream pressure. The leak rate was determined with helium and the linear behavior allows to study a larger range of leak rate as compared to the old system.

The leak rates found experimentally have been used to extend the ionization model (Sec. 3.5) by means of molecular flow simulations. In addition to the leak rate as a model input, a particle sink has been added as a boundary condition downstream of the extraction electrode system (see Fig. 3.8). The results indicate a relatively homogeneous particle density except near the outlet and near the grid. At the outlet, the depletion of neutrals causes a decrease of particle density. Conversely, near the

grid there is a large number of particles mainly because this area is in direct line of sight from the transferline emitting aperture.

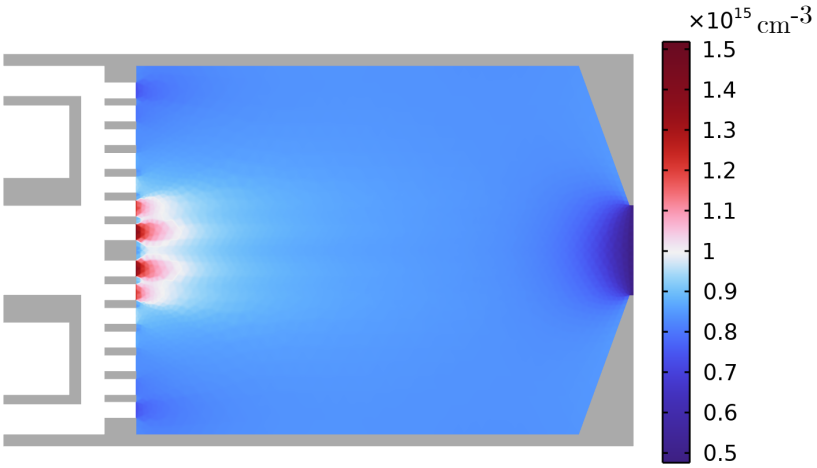

Figure 4.17: Neutral argon density inside the anode volume as found from simulations. The center of the grid presents higher neutral density as it is in direct sight from the jet exiting the transferline aperture.

The gas system presented here for the ISAC TS differs from what is currently in place at the online ISAC target stations—a system based on the old paradigm (see Sec. 2.3). The difference prevents a direct comparison for stable isotopes between the online and offline systems. However, during online operation, the partial pressure from the radioactive neutrals arriving at the anode volume is enough to generate an ion signal. For example, by studying a radioactive isotope of argon, a comparison to the offline characterization is possible. The planned FEBIAD ion source to run in June 2022 will provide the insight required to compare the intrinsic differences between the origin of the gas flowing into the anode volume, that is, the differences between stable species by continuous gas injection and species produced by nuclear reactions.

4.4 Chapter Summary

The electric field relation $E = V/d$ is only true between two infinite plane surface. The value depends on specific geometry features such as small radius or sharp edges, and also on the varying distance due to structural deformations. The deformations observed add a dependency to the distance as $d = d(T)$, which directly affect the magnitude of the electric field between anode and cathode. However, the goal of matching

deformations with simulations is outside of the scope of this thesis. Consequently, differences to the simulated electron current values are expected, and therefore the ionization model uses the experimentally measured electron currents. Nevertheless, the electron current has been divided in two contributions as found from the melted grid studies.

The ionization model requires the values of neutral density inside the anode volume to compute the ionization rate per unit volume (see Sec. 3.5). With the molecular flow simulations, the neutral density can be computed and passed onto the ionization model. In this way the model also reflects the non-ideal apertures presented along the TIS assembly (e.g Fig. 2.3).

Chapter 5

Experimental Validation of the FEBIAD Ionization Model

The intrinsic nature of the radioactive isotopes demands a highly efficient ion source as the number of isotopes is limited. To elucidate the underlying and limiting mechanisms of the source, an experimental campaign has been performed to characterize fundamental aspects of the FEBIAD source. The campaign consists of exploring the FEBIAD parameter space comprised by the cathode temperature, anode voltage, magnetic field, and geometry features. With the measured ionization efficiency as the figure of merit, the multidimensional data provides insights into the source performance.

This chapter presents and discusses the experimental results and how they can be explained based on the ionization model.

5.1 Ionization Efficiency Measurements at Nominal Cathode Temperature.

Predetermined values dictate the nominal parameters used for conditioning and operating the FEBIAD ion source (Table. 5.1). Based on the cathode calibration found in Sec. 4.1, the nominal cathode heating current corresponds to a cathode temperature of $\approx(1690 \pm 25)$ °C. Ionization efficiency measurements were performed at this fixed temperature while varying anode voltage and coil current.

Table 5.1: Legacy nominal values for the FEBIAD conditioning and operation.

Parameter	**Legacy operation value**
Cathode current [A]	290
Anode voltage [V]	200
Coil current [A]	30

High Level Application (HLA) scripts have been developed in Python to control the main parameters of the FEBIAD ion source (see Sec. 2.3). In this case, the scripts vary the anode voltage and coil current in steps of 10 V and 10 A, respectively. The scanned range for the anode voltage and coil current (anode-coil from here onwards) is defined by the power supply limits and corresponds to 500 V and 100 A. Additionally, the scripts simultaneously record the electron current measured by the anode power supply and the mass separated ion current. The electron current measurements elucidate the cathode emission regime by comparing them to the emission models described in Sec. 3.1. Complementary, the ion current measurements allow determining the ionization efficiency for all the parameter combinations investigated.

Ionization efficiency measurements were performed by injecting stable argon into the ion source and measuring ^{40}Ar, the most abundant isotope. The neutral particle rate used throughout the experiment was $\approx 1 \times 10^{13}$ pps, which is an equivalent *neutral particle current*[1] of 1.6×10^{-6} A that can be compared directly to the Faraday cup readings. During the experiment, some residual argon from the atmosphere was present; however, the background signal was constantly monitored and constituted less than 0.2 % of the total argon ion current measured. Other elements could have been used to investigate the efficiency and other aspects of the source, e.g. molecular formation; however, reported efficiencies are typical for argon and hence the values reported here are directly comparable to the FEBIAD sources at other facilities.

The results from the bi-dimensional measurements are presented as a contour plot in which the color scale indicates the ion current magnitude (see Fig. 5.1). The ion current plot shows the suboptimal anode-coil parameter combination used for the nominal heating current. Moreover, the contours are quasi-parallel to the voltage axis but perpendicular to the coil current axis. This behavior indicates the ion current exhibits almost no dependence on anode voltage but linear dependence on coil current. The voltage dependence of the ion current likely arises from the cathode operating in a temperature limited regime in which no more electrons are extracted despite a voltage increase (see Sec. 3.2). On the other hand, the ion current coil dependence likely arises due to the electron confinement, which increases the electron current density near the grid (see Fig. 3.6) and ultimately increases the number of ionization events (see Eq. 3.11). The ionization efficiency is obtained by taking the ratio of the measured ion current to the neutral particle current entering the source. For the nominal parameter combination, the efficiency found is ≈0.70 %, and the maximum efficiency is ≈1.0 %.

[1] current obtained by multiplying the rate by the elemental charge $e = 1.602 \times 10^{-19}\,\mathrm{A\,s^{-1}}$

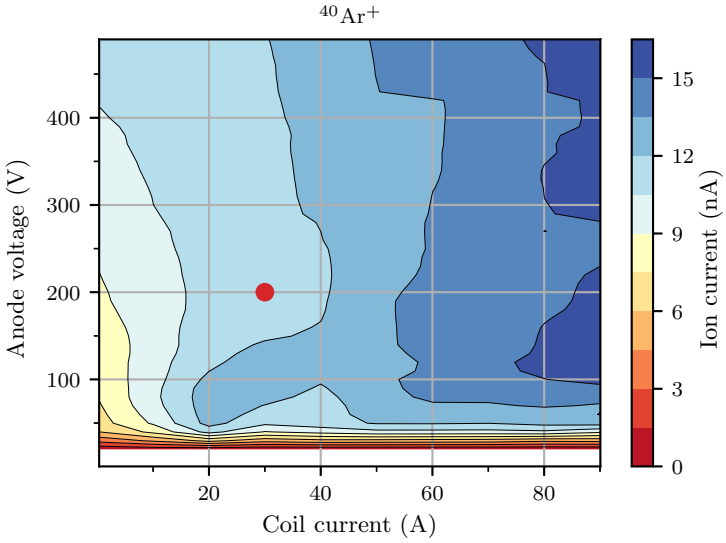

Figure 5.1: $^{40}Ar^+$ ion current contour plot as a function of anode voltage and coil current for a cathode heating current of 290 A. This current corresponds to ≈1690 °C, and the red dot indicates the nominal parameter combination commonly used for operation.

5.2 Multiparameter Ionization Efficiency Measurements

The HLA implementation enables the exploration of the multiparameter space of the FEBIAD ion source (see Sec. 2.3). However, in the previous section only the anode voltage and the coil current were varied and recorded. Now, the cathode heating current has been also varied, and a dominant effect on the ionization efficiency has been observed. This effect is expected from the thermionic emission, which increases the available number of electrons for ionization (see Sec 3.1); however, the anode voltage also affects the ionization efficiency as the electron transport is affected by the space-charge limited emission (see Sec. 3.2). The ionization efficiency dependency on temperature and voltage is first discussed separately, with a combined discussion following.

Variations on the cathode heating current were performed from 290 A to 335 A, corresponding to a temperature ranging from ≈1640 °C to ≈1940 °C (see Sec. 4.1). The thermionic emission equation (Eq. 3.1) used in a fitting routine shows good agreement with the electron current as a function of temperature (see Fig. 5.2a). Additionally, the $^{40}Ar^+$ ionization efficiency as a function of cathode temperature shows a maximum efficiency for the highest cathode temperature except for 50 V (see Fig. 5.2b).

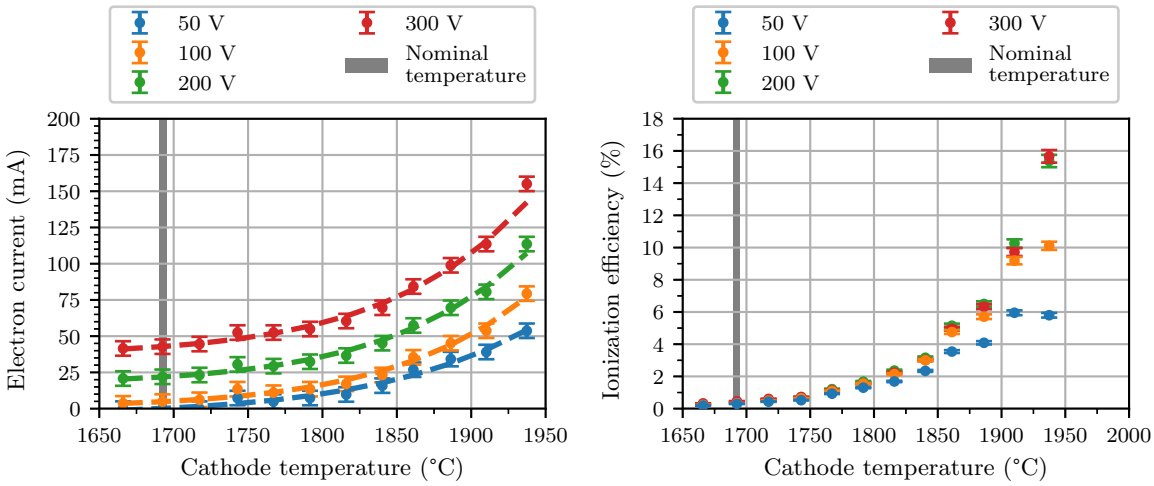

(a) Electron current **(b)** Ionization efficiency

Figure 5.2: Electron current I_e and ionization efficiency as a function of temperature for a few anode voltages. The gray rectangle indicates the nominal temperature of ≈1690 °C. In (a), the electron current follows the thermionic emission equation (Eq. 3.1) as shown by the fitted dashed curves. In (b), at 50 V the efficiency saturates, but at higher voltages the efficiency increases with temperature.

The results at 50 V indicate a saturation in efficiency as the temperature increases (similar to [4]). This saturation likely arises from the cathode operation transition to the space charge limit regime where despite a temperature increase, the electron current is determined by the anode voltage (see Sec. 3.2). The plot also shows the relatively low nominal cathode temperature and explains why during preliminary measurements, the efficiency at nominal parameters was below 1 %.

The voltage dependency measurements (see Fig. 5.3) also allow investigating both the cathode emission regime and the role of the Schottky emission regime on the ionization efficiency (see Sec. 4.1). First, the electron emission shows two regimes as a function of voltage: the space-charge limited regime for values below ≈300 V and the Schottky regime for higher values (see Fig. 5.3a). Next, to correlate the electron current and the ionization efficiency, the electron impact ionization cross section (see Sec. 3.3) is also plotted as a function of $V = E_k/q$. The ionization efficiency onset at ≈20 V matches the cross section threshold value (see Fig. 5.3b). For values between 150 V to 350 V, the ionization efficiency is relatively flat due to an electron current increase and a cross section decrease. The ionization efficiency decrease observed above ≈350 V at the temperatures 1886 °C (pink) and 1937 °C (gray) arises from the decrease in cross section at these energies. This efficiency decrease contrasts with the electron current that still increases for voltages higher than 300 V.

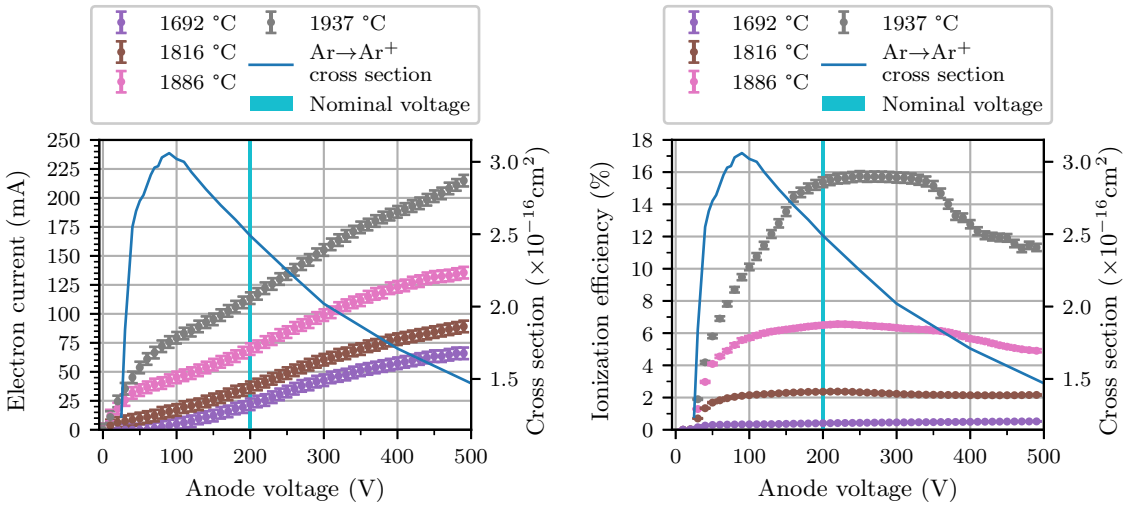

(a) Electron current **(b)** Ionization efficiency

Figure 5.3: Electron current I_e and ionization efficiency as a function of anode voltage for a few cathode temperatures. The cyan line indicates the nominal voltage of 200 V. In (a), the electron current increases linearly as of 300 V. In (b), the efficiency decreases as of 300 V.

The results suggest that for anode voltages >300 V, not all the electrons are available for the ionization process (as it is also observed in figure 5.2). This distinction is explained by considering the surface electric field at the two rims of the FEBIAD cathode: one facing the central part of the grid and the other facing the outer grid radius connected to a section of the anode body (see Fig. 5.4). The surface electric field has been simulated by assuming a perfect parallel gap of 1 mm and perfect concentricity. However, thermal-induced deflections likely cause shorter gaps between the cathode and the anode-grid bodies (see Sec. 4.1.1). These deflections increase the electric field at the rims, and the electrons emitted at these locations are registered in the power supply; however, these electrons do not necessarily enter the anode volume to cause ionization.

The ionization efficiency dependency on both temperature and anode voltage are combined to present a 2D contour plot (see Fig. 5.5). The explanations presented so far are observed in the marginal plots; nevertheless, the contour plot shows the increased efficiency with increasing temperature at voltages ranging between 200 V to 300 V. The efficiency at nominal parameters (red point) has a value <1 %, while the maximum efficiency shown is ≈16 %. At all temperatures, a complementary coil current scan finds a 2D contour plot similar to the one shown in Fig. 5.5 but with a maximum efficiency of ≈20 %.

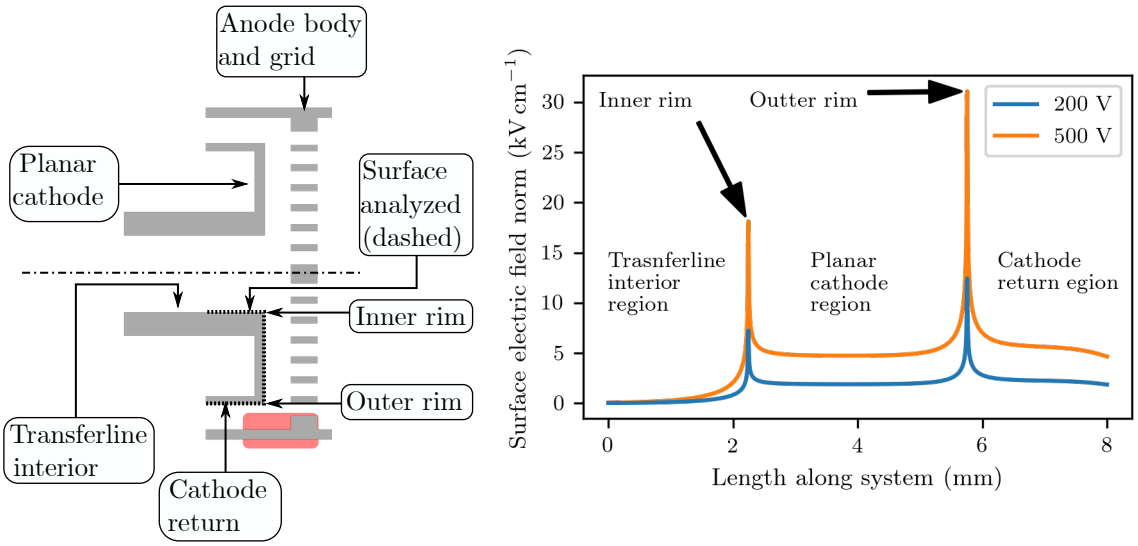

Figure 5.4: Electrostatic simulation showing an increased surface electric field at the edges of the inner and outer rims of the cathode, from which enhanced thermionic emission occurs. The electrons generated at the outer rim strike the grid and part of the anode body (red rectangle).

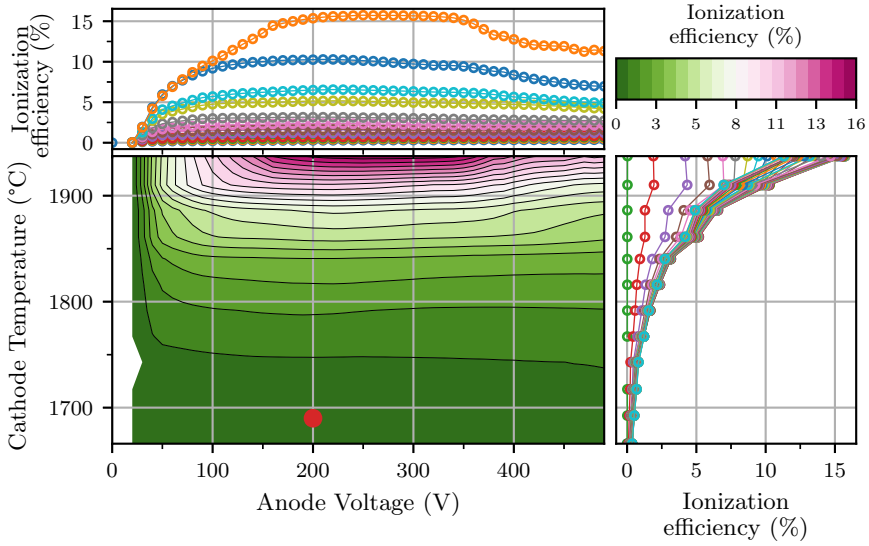

Figure 5.5: Ionization efficiency contour plot as a function of cathode temperature and anode voltage. The marginal plot on top corresponds to the voltage dependence only, and the marginal plot to the right corresponds to the temperature dependence only.

Ionization efficiency measurements were further performed with a modified grid. As explained in Sec. 4.1.1, the center of the grid melted upon intense heating. Nevertheless, an open grid facilitates validating the ionization model with a different geometry, and understanding the role of the grid design used for ARIEL and ISOLDE. For this new geometry, electron current and ionization efficiency contour plots are presented.

The measured electron current is shown as a contour plot alongside the marginal plots for both temperature and voltage (see Fig. 5.6). At the top marginal plot, the electron emission follows the space charge regime for voltages <350 V and the Schottky regime above that voltage. On the other hand, the right marginal plot shows the temperature dependence that follows the thermionic emission regime. The contour plot shows directly how the electron current increases simultaneously with increasing temperature and voltage.

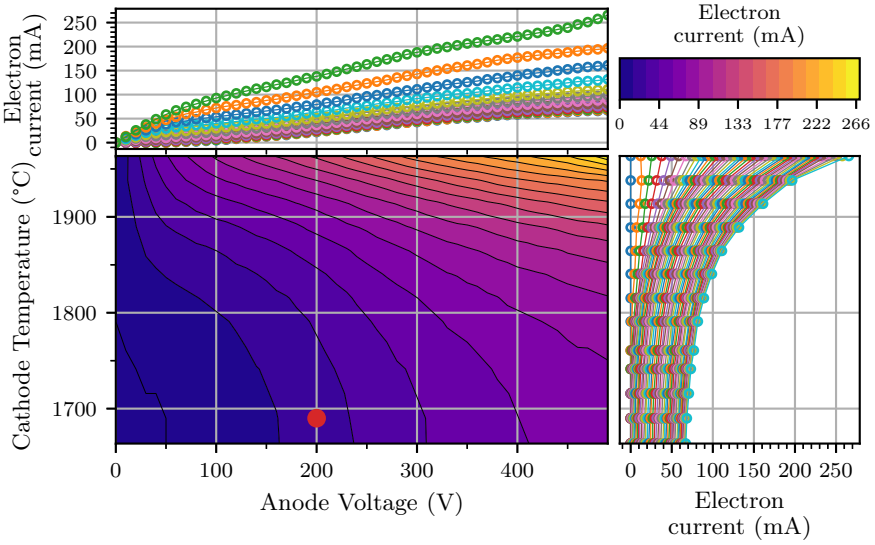

Figure 5.6: Electron current contour plot as a function of cathode temperature and anode voltage for coil current=0 A with an open grid. The electron emission follows the same behavior as the nominal geometry (compared marginal plots to Figs. 5.2a and 5.3a).

The ionization efficiency for the open grid geometry is shown as a function of cathode temperature and anode voltage (see Fig. 5.7a). The efficiency flattens as of 350 V while the electron current increases (see Fig. 5.6), suggesting that the Schottky effect is still present at lower temperatures and higher anode voltages. Moreover, this behavior also indicates the electron current is not fully used to cause ionization. Conversely, for values below 350 V, both electron current and ionization efficiency increase linearly together as expected from Eq. 3.11. Without the magnetic field present, the open grid geometry shows a maximum efficiency of 6 %, while the closed grid presents an efficiency of ≈16 %. The ionization efficiency is almost a factor of 2.5 larger for the closed geometry with respect to the open geometry.

The magnetic field in the open grid geometry plays a contrasting role with respect to the closed grid; the ionization efficiency increases from 6 % to ≈21 % when going from a coil current of 0 A to 60 A (see Fig. 5.8). As explained in section 4.1, the hottest part of the cathode is located inside the transferline. This temperature profile

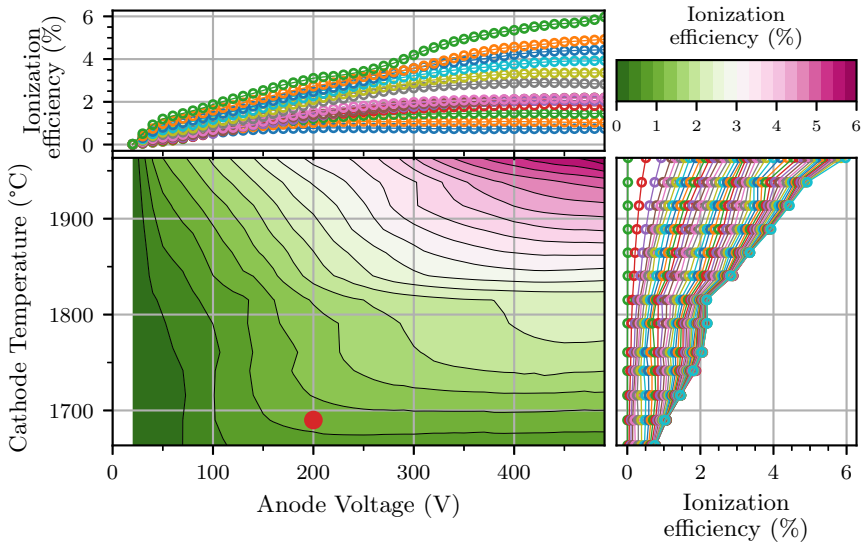

(a) Open grid with no coil current

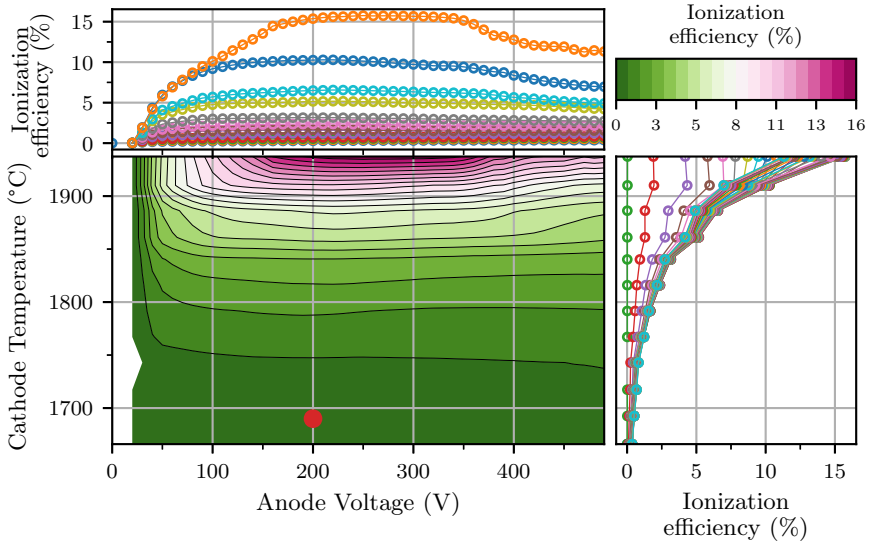

(b) Closed grid and no coil current

Figure 5.7: Ionization efficiency contour plot comparison for two geometries with no coil current. In (a), the overall trends match those of the electron current (Fig 5.6). In (b), the previous Fig. 5.5 is reproduced for comparison.

means more electrons are extracted from the transferline region with perpendicular velocity to the axial magnetic field. Therefore, the electrons collide into a closed grid geometry, but otherwise, the electrons enter the anode volume to cause ionization (see Fig. 5.9). The electron trajectories explain why the magnetic field does not seem to play a relevant role in the efficiency of the ISAC FEBIAD nominal geometry[2].

[2]in 2017, the SiC#37 FEBIAD had no coil and ran without detrimental performance.

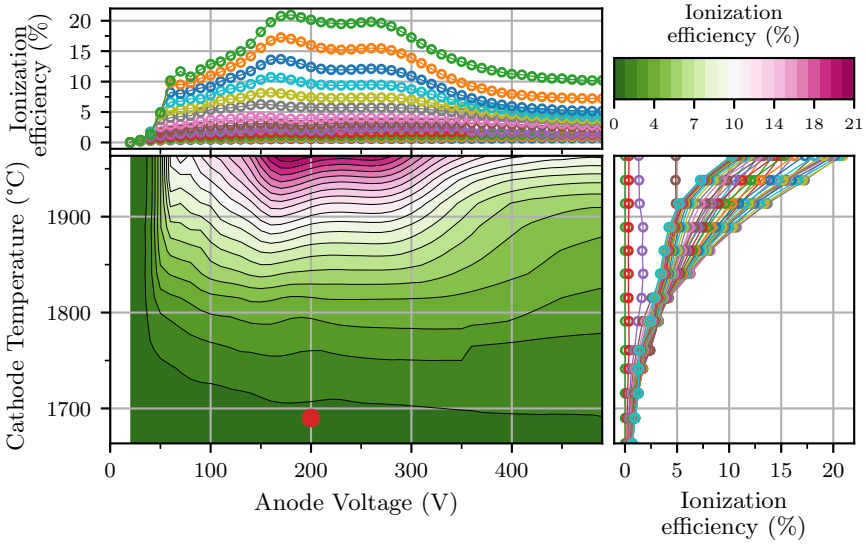

(a) Open grid and coil curent=60 A

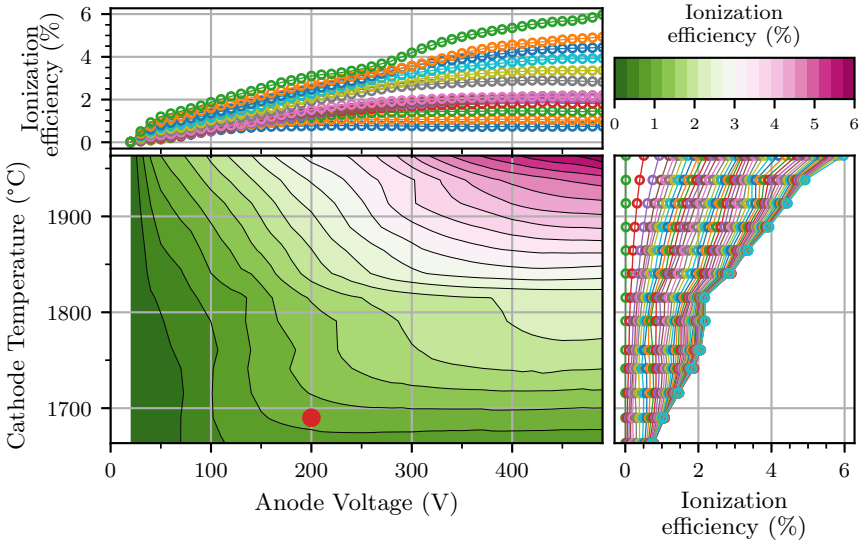

(b) Open grid with no coil current

Figure 5.8: Ionization efficiency contour plot for the open grid geometry and two coil currents. In (a), a coil current of 60 A modulates the efficiency which reaches a maximum value of ≈21 %. In (b), the no coil current plot from Fig. 5.7a is reproduced for easier comparison.

The measurements presented so far indicate some limitation on the ISAC FEBIAD design. For example, a maximum cathode heating current of about 335 A, corresponding to ≈1940 °C. The ionization efficiency for nominal values (see Table 5.1) is less than 1%, while the maximum efficiency for the closed grid before melting is around 10%; with an open grid the maximum efficiency reaches around 20%. Therefore by operating the source at different setting there is a ten-fold increase on ionization ef-

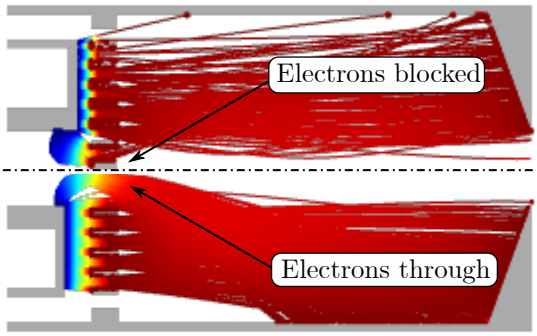

Figure 5.9: Electron trajectories at 500 V and 30 A for two grid geometries. More electrons enter the anode with an open grid, but the beam expands, reducing both the electron current density and the ionization rate. By adjusting the magnetic field is possible to increase the ionization rate.

ficiency; however, higher values are possible by proposing optimal designs (as shown in Chapter 6).

To understand how the efficiency at the maximum temperature changes with anode voltage and magnetic field, the measured anode-coil scan for both geometries are compared to simulations, and they qualitatively agree (see Fig. 5.10). Two simulations results are compared to the measurements; the first consists of the ionization rate I_{n_i} (see Eq. 3.12), and the second shows the extracted ions from the anode as depicted in Fig. 3.8. All quantities are normalized to their maximum value for easier comparison. For the closed grid (see Figs. 5.10a–5.10c), an increased efficiency island is found experimentally between 100 V to 200 V and between 20 A to 40 A, but the ion extracted prediction is shifted towards 150 V to 250 V and between 30 A to 60 A. The general feature of the closed grid is that as of 100 V the efficiency is mostly above 0.6 and this is captured by the simulations. To obtain this qualitative trend, the cathode-anode distance was reduced from 1 mm to 0.75 mm, which suggests a deformation in this range (see Sec. 4.1.1). This geometrical change also suggests that the angle between cathode and anode (see Fig. 4.10a) likely causes a different condition to enter the anode volume, arising from the electron velocity and magnetic field ($\vec{v} \times \vec{B}$). Complementary, the anode-coil scan for the open grid is also compared to simulation and they show good agreement (see Figs. 5.10d–5.10f). The simultaneous efficiency increase with anode and coil is a consequence of more electrons available for ionization, corresponding to an increased ionization rate in regions that favors ion extraction (as in Fig. 3.6). Consequently, the results confirm that the relevant areas assumed in the ionization model are valid, and specifically that most of the ions are generated at the back of the anode near the grid (see Sec. 3.5 and Fig. 3.7).

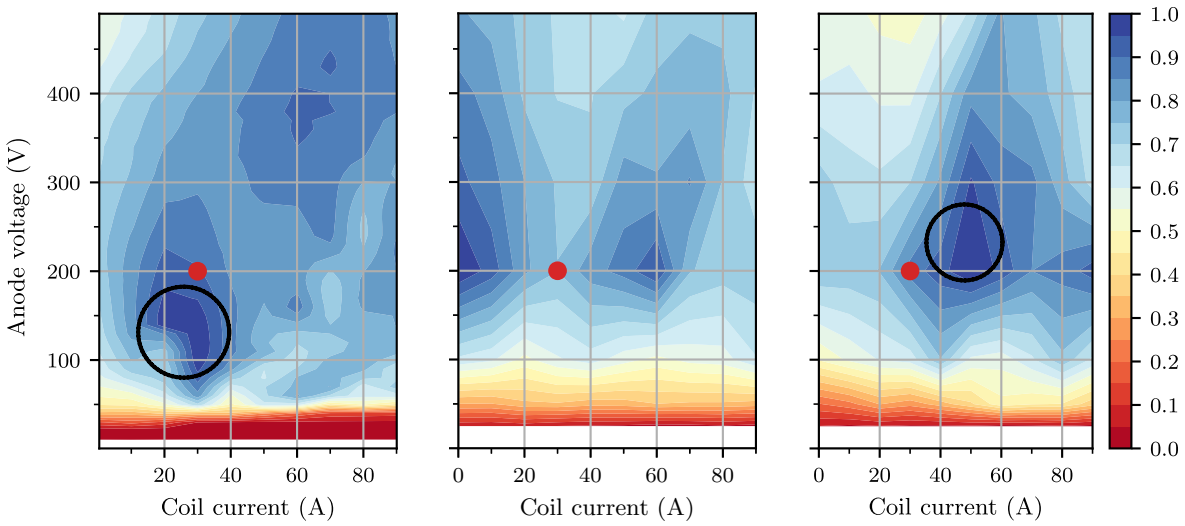

(a) Closed grid: Normalized measured efficiency

(b) Closed grid: Normalized ionization rate (I_{n_i})

(c) Closed grid: Normalized simulated ions extracted

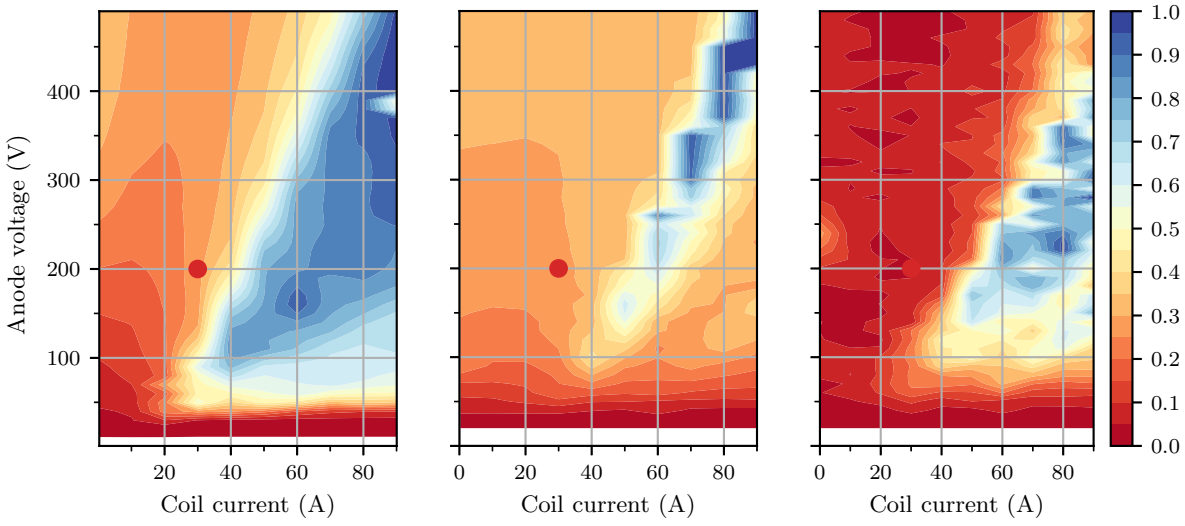

(d) Open grid: Normalized measured efficiency

(e) Open grid: Normalized ionization rate (I_{n_i}))

(f) Open grid: Normalized simulated ions extracted

Figure 5.10: Anode-coil scan comparison between measurements and simulation for both closed (top row) and open (bottom row) grid at a temperature of ≈1950 °C. With the closed grid [(a)-(c)], above 100 V most of the values found are above 0.6 and an island of increased efficiency exists as a consequence of blocked electrons that can only enter the anode under specific coil current values. With the open grid [(d)-(f)], all plots share the same trend of increasing simultaneously with coil current and anode voltage as those combinations allow most of the electrons to enter the anode volume with higher current density. In all ion extracted simulations, the particles are mostly created adjacent to the grid and the overall trends shown validate the assumption presented in the model of Sec. 3.5.

5.3 Anomalous Ionization Regime

During measurements at the limiting values of cathode temperature (>1950 °C) and anode voltage (>350 V) (see Sec.4.1.1), an anomalously high electron current correlates to an increased ionization efficiency (see Fig. 5.11). The onset of the anomalous electron current starts at ≈1900 °C and matches the grid failure of an open center, and this has been confirmed on a second TIS unit (see Sec. 4.1.1).

The electron current as a function of cathode temperature follows the thermionic emission regime in the temperature range of 1600 °C to 1900 °C as they match the fitted dashed curves (see Fig. 5.11a). Moreover, for temperatures >1900 °C and voltages ≤100 V, the electron current seems to transition from the thermionic emission regime to the space charge regime. However, for cathode temperatures >1900 °C and for voltages ≥200 V, the electron current sharply increases and the fitting routine cannot describe the data despite the material properties being unconstrained. This anomalously high electron current causes an ionization efficiency increase from 7 % to 21 % at a fixed anode voltage of 300 V (see Fig. 5.11b).

The voltage dependency of the electron current also presents the anomalously high electron current at the temperatures 1912 °C (brown) and 1927 °C (pink) (see Fig. 5.11c). The sharp rise at the mentioned temperatures contrasts with the gradual increase shown in Fig. 5.3. In this anomalous case, the electron current is limited to protect the power supply, and they share a maximum value of 500 mA. Conversely, the voltage dependency of the ionization efficiency (see Fig. 5.11d) at those temperatures differs from 21 % (pink) to 27 % (brown). Moreover, the ionization efficiency at 1912 °C (brown) varies from 10 % at 300 V to 28 % at 390 V. At the cathode temperature 2062 °C (yellow), the power supply current limit was increased to 800 mA, and the maximum increase is from 10 % to 20 % at voltages of 100 V and 150 V, respectively. This behavior indicates higher voltages correlate to higher efficiencies regardless of the cathode temperature.

The observations on the anomalous regime suggest that after the grid becomes open, the sharp points created sustain increased localized electric fields between the transferline/inner rim to the center of the grid (similar to Fig. 5.4). Additionally, the thermal expansion likely causes the cathode to get closer to the anode, and these areas contribute more to the number of electrons entering the anode volume (as in Fig. 5.9). Both effects sharply increase the electron current extracted (see Fig. 5.11a and 5.11c) and show how this enhancement can improve the ionization efficiency (see Fig. 5.11b and 5.11d). However, the anomalous regime vanished after intense heating in both

sources investigated. The results suggests that a grid featuring both enhanced electric fields and thermal robustness at the grid center can extract more electrons from the cathode center, and consequently improve the ionization efficiency.

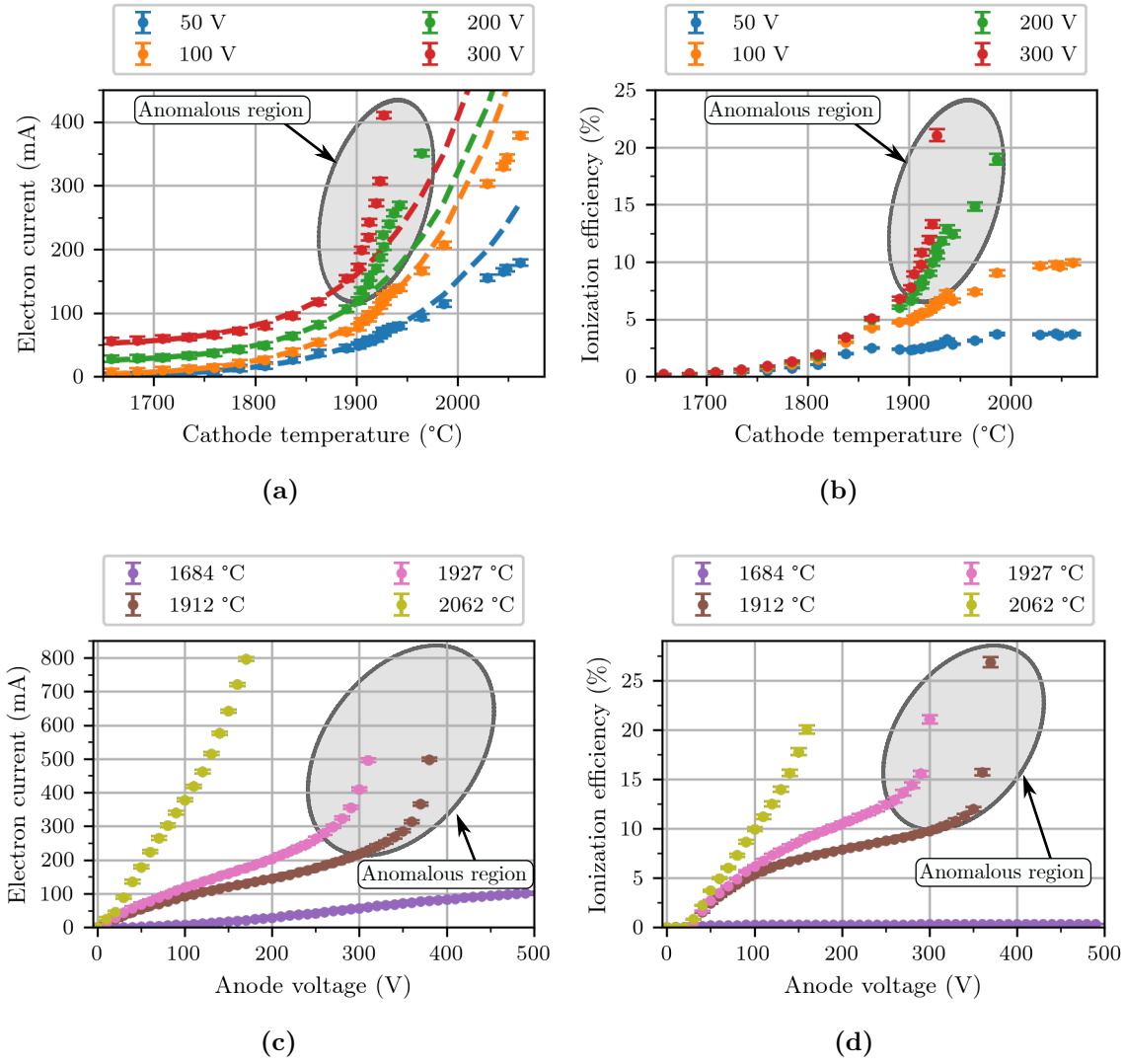

Figure 5.11: Electron current and ionization efficiency for the anomalous ionization regime. In (a)–(b), the electron current and the ionization efficiency sharply increase as of 1900 °C, which matches the grid failure. In (c)–(d), the electron current after the grid failure increases with increasing voltage but is limited to protect the power supply. Despite a similar (or higher) electron current measured, the ionization efficiency is higher for the temperature 1912 °C despite higher cathode temperatures measured.

5.4 Ion Current Measurements for Other Ion Species

Different species were investigated during the ionization efficiency campaign to provide further insight into the ion source performance. For this, a mass spectrometry analysis was performed at each cathode temperature and nominal anode voltage=200 V and coil current=30 A (e.g. Fig. 5.12) . The analysis confirms that the dominant beam is the injected argon in both single and double charge states. The second most dominant species is water (H_2O at $^m/_q$=18), followed by its fragments OH, O, and H_2 at 17, 16, and 2, respectively. At $^m/_q$=28, the peak corresponds to either Si, N_2, or CO. The large peaks at $^m/_q$=90 and $^m/_q$=98, correspond to the doubly charged Ta and TaO, respectively. The rest of the masses typically originate from components near hot areas, for example, stainless steel screws, aluminum nitride insulators, or any other impurities within the TIS assembly. Species two orders of magnitude smaller relative to the highest peak were not analyzed further; however, species of interest were investigated by performing an anode-coil measurement.

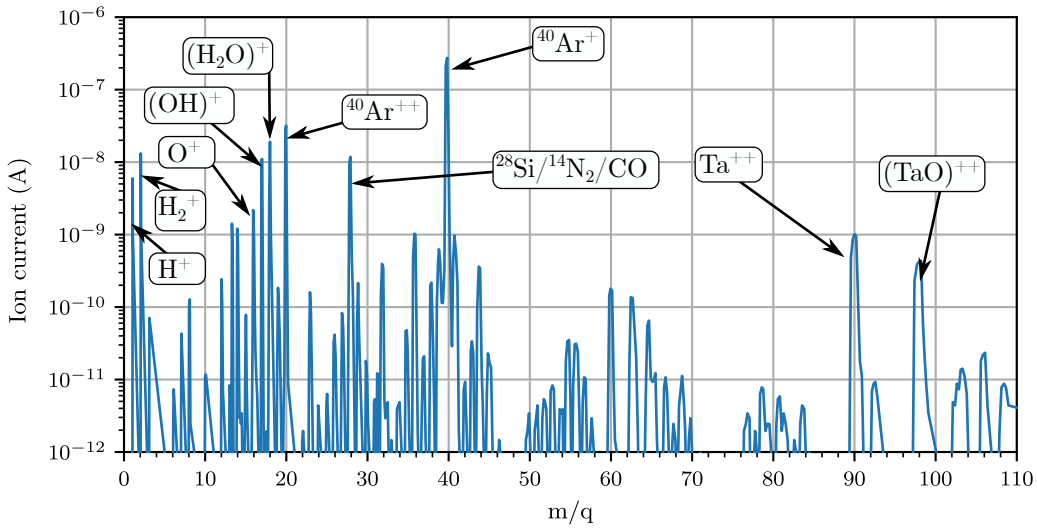

Figure 5.12: Mass spectrometry analysis at 1950 °C, 200 V, and 30 A.

The anode-coil scans on different ion species help to correlate different parameter combinations with the distinct material components of the ion source (see Fig. 5.13). For example, O_2^+ increases with coil current as the coil insulator jacket consists of SiO_2, which evaporates upon heating. The Si^+ signal, as explained previously, is a combination of three possible masses measured at $^m/_q$=28; however, a portion of the signal increases with coil current and likely originates from the coil insulator jacket

(N_2 and CO are explained in the next paragraph). Additionally, the Ta^{++} increases linearly with voltage due to the electron power deposition into the tantalum grid (see Sec. 4.1.1) and the consequent evaporation, which increases the number of neutrals to ionize.

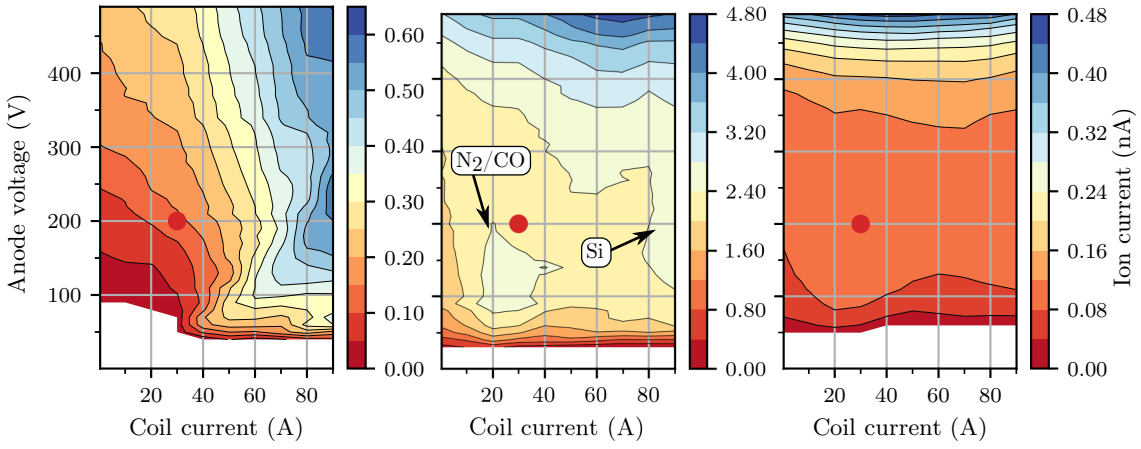

(a) O_2^+ **(b)** $Si^+/N_2^+/CO^+$ **(c)** Ta^{++}

Figure 5.13: Ion source material species investigated at a temperature of ≈1950 °C showing the ion current measured in nA. A red point denotes the nominal operation parameters. In (a), molecular oxygen increases with coil current because the coil insulator jacket consists of SiO_2, and upon heating, the material evaporates with subsequent break up into O_2 and Si. In (b), the $^m/_q$=28 increases with voltage as it increases the heating in the anode body, and hence increased desorption occurs; the coil current dependence originates from the Si arising from the coil insulator jacket. In (c), the linear increase with voltage is due to the intense grid heating, which evaporates the tantalum material.

Residual gases are ever-present in the system and were also investigated with an anode-coil scan (see Fig. 5.14). Water, nitrogen, and carbon dioxide originate from the ambient because the vacuum chamber is necessarily open for every TIS unit exchange. Water molecules tend to remain on the inner chamber walls, and they are constantly desorbed as the pressure decreases inside the vacuum chamber. On the other hand, $^m/_q$=28 comprises Si (explained previously), N_2, and CO. The CO arises from thermal dissociation with subsequent electron impact ionization or from dissociative ionization of CO_2 [64]. For easier comparison, Ar^+ is plotted as well as the doubly charged state, Ar^{++}. With this, the species arising from residual gases seem to follow a similar trend to the Ar^+ anode-coil scan. Specifically, they show an increased efficiency island and higher currents towards larger anode voltage and coil current values. The overall ion current dependence indicates that the ion generation

follows a similar ionization map as found from argon (see Fig. 3.7). Finally, the results across species suggest the possibility of chemical selectivity as different trends and ion current values are obtained for different parameters. An anode-coil scan could show where the beam of interest is enhanced or where an undesired species is reduced.

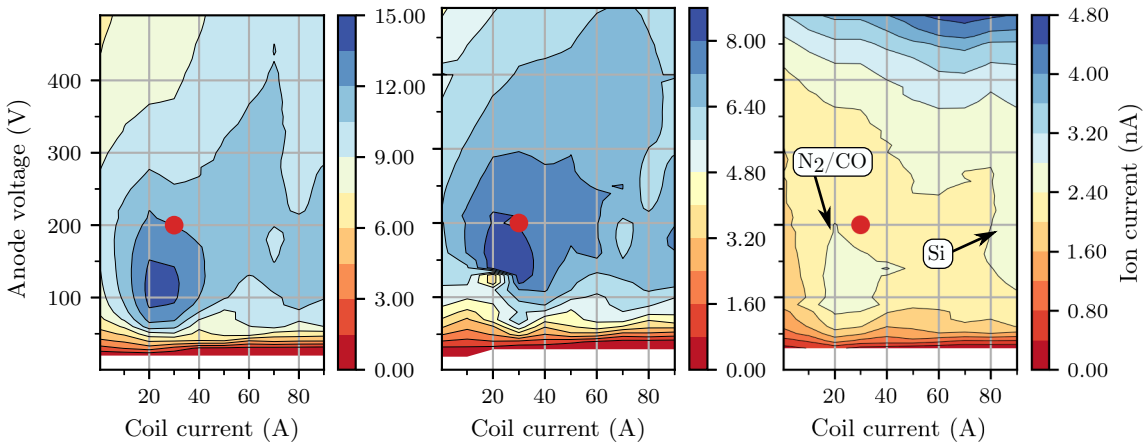

(a) H_2O^+ **(b)** OH^+ **(c)** $Si^+/N_2{}^+/CO^+$

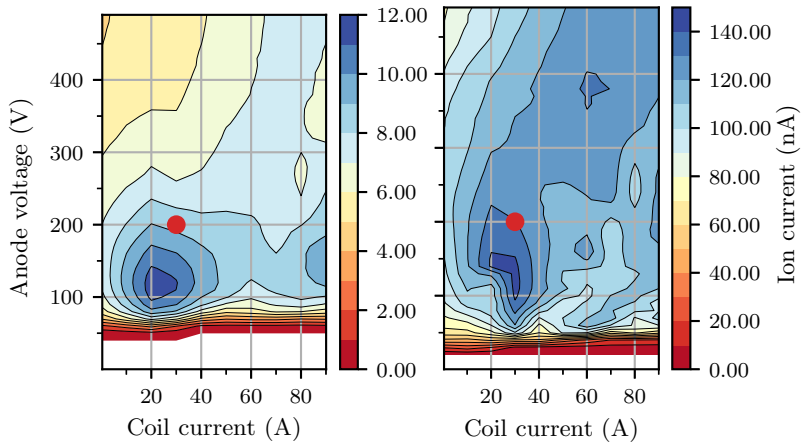

(d) $^{40}Ar^{++}$ **(e)** $^{40}Ar^+$

Figure 5.14: Residual gas species investigated showing the ion current measured in nA. A red point denotes the nominal operation parameters. In (a) and (b), water and OH present an increased island efficiency and larger values towards higher anode voltage and coil current. In (c), a similar island appears and this is likely N_2 or CO. In (d), the doubly charge argon ion presents a higher efficiency island similar to the singly charge ion (e). The similar trends indicate similar initial conditions for the ions generation.

5.5 Beam Emittance

Emittance measurements were performed with an Allison-type meter at a cathode temperature of ≈1940 °C (see Fig. 5.15). The simulated ion beam 4RMS-emittance ($\epsilon_{4_{\mathrm{rms}}}$, Sec. 3.5) is computed and compared to the measured ion beam 90 %-intensity-emittance $\epsilon_{90\%}$. The 90 % emittance corresponds to the phase-space area containing approximately 90 % of the ion current. The comparison of different emittance definitions arises from the different planes in the beamline where values are simulated and measured [65]. The measured and simulated emittance shows good agreement validating the ion beam extraction model (see Table 5.2). According to ion tracking simulations, the beam 4RMS-emittance for the closed grid is determined by the ions generated on axis, while for the open grid there is a contribution from the larger initial radial position in which the ions are created.

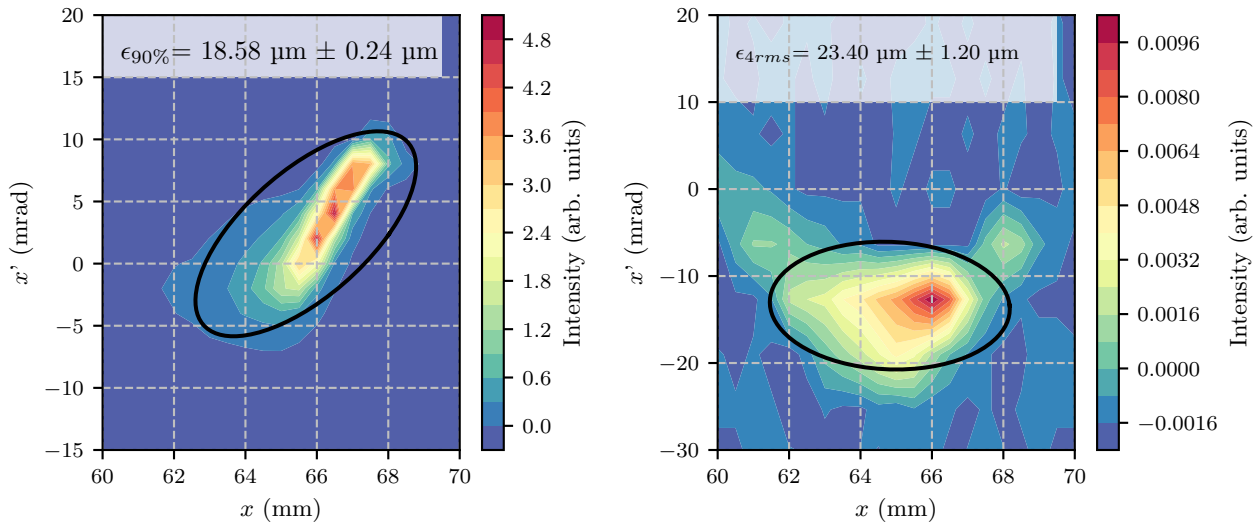

(a) Closed grid **(b)** Open grid

Figure 5.15: Measured phase space for 200 V and 30 A for the nominal grid geometry. The x axis is the reference of the emittance meter with respect to the beam path.

Table 5.2: Measured and simulated emittance comparison for two grid geometries. Both values correspond to a cathode temperature of ≈1940 °C, anode voltage of 200 V, and coil current of 30 A.

Geometry	**Measured $\epsilon_{90\%}$ (µm)**	**Simulated $\epsilon_{4_{rms}}$ (µm)**
Closed grid	18.58 ± 0.24	18.45
Open grid	23.4 ± 1.2	23.02

5.6 Beam Energy Spread: Ionization Model in an ARIEL-Like Geometry

The simulations implemented to describe the FEBIAD multiparameter behavior have been developed assuming an electron dominant regime (see Sec. 3.5). In this regime, positive ions not extracted as beam do not affect the ionization maps described in section 3.5. Consequently, the beam energy spread and mean energy are defined from the initial position inside the anode volume as explained and shown in Table 3.1. The remaining ions are either lost to the cathode and anode body walls, or move inside the potential well with energies from ≈0.2 eV to ≈30 eV. Any influence by those trapped positive ions on the electric potential can therefore change the beam energy spread and mean energy. For ARIEL, the energy spread limits the maximum resolution for momentum separation of the isotopes [9]. By measuring the energy of the beam, it is possible to both characterize the lower limit for energy spread and verify the electron dominant regime.

The FEBIAD's ion beam energy has been investigated as a function of the magnetic field to further validate the ionization model. Data previously reported in [38] indicates that the ion beam mean energy is always lower than expected from the voltage defined between anode body to extraction ground electrode. The trend indicates that only a partial positive charge compensation could exist, and this has been investigated for an ARIEL-like geometry (see Fig. 1.7). The measurements were taken at the GANIL facility as they operate a FEBIAD with an identical geometry to the ARIEL one.

Energy spread measurements were performed with a retarding field analyzer. In this device, a fine mesh is placed in the beam path, and a voltage V_m is applied. Particles with energy $E \geq q \cdot V_\mathrm{m}$ can pass through, but with increasing voltage, the particles with the energy $E \leq q \cdot V_\mathrm{m}$ are repelled back and are not measured.

The energy distribution can be approximated by a Gaussian function

$$n(E) = \frac{A}{\sqrt{2\pi}\sigma_\mathrm{E}} \exp\left(-\frac{(E-E_0)^2}{2\sigma_\mathrm{E}^2}\right),$$

where E is the particle energy (eV), E_0 the mean energy (eV), and σ_E the energy standard deviation (eV). The measurement, however, corresponds to the cumulative of a Gaussian, the so-called error function as a function of the mesh applied voltage $V_\mathrm{m} = E/q$:

$$N(V_\mathrm{m}) = 0.5A\left(1 - \mathrm{erf}\left(\frac{V_\mathrm{m} - E_0}{\sigma_\mathrm{E}\sqrt{2}}\right)\right). \tag{5.1}$$

Figure 5.16 exemplifies the distributions but given how sensitive numerical derivatives are, it is common to fit the raw data with the error function rather than transforming the data to a Gaussian and then fitting it.

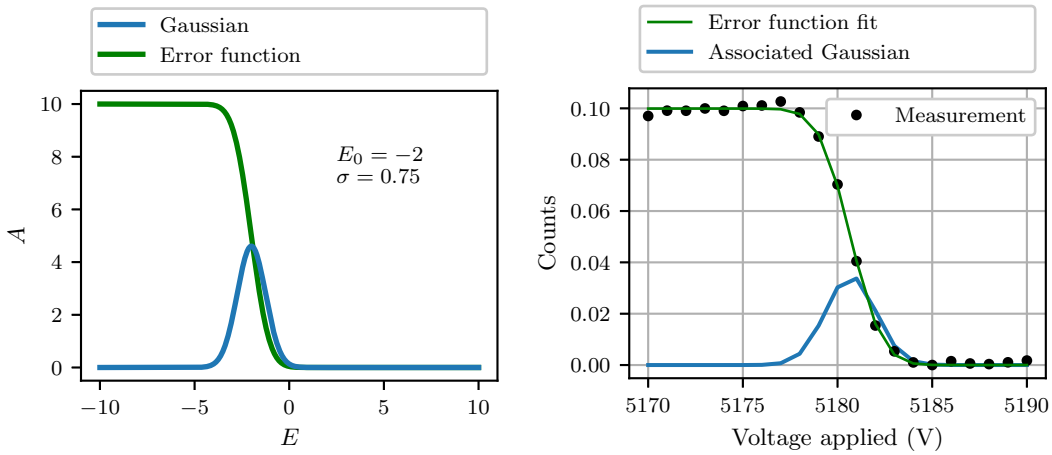

(a) Distributions with same parameters

(b) Measured data with fit

Figure 5.16: By knowing the error function parameters the associated Gaussian distribution is reconstructed. The measurements were fitted directly with the error function (Eq. 5.1) to obtain the mean (E_0) and standard deviation (σ) of the corresponding Gaussian distribution.

The beam mean energy and the energy spread presents an almost linear dependence with coil current and match the simulated values (see Fig. 5.17). First, the energy offset is defined as the difference between the fitted parameter E_0 and the total applied voltage to the source V_s, that is

$$E_{off} = E_0 - q \cdot V_s.$$

In these measurements, the expected energy corresponds to the applied voltages $V_s = 5034\,\text{kV} + 150\,\text{V} = 5184\,\text{V}$, corresponding to the high voltage platform plus the anode voltage, respectively. The results show that the beam mean energy is consistently lower than the expected ion beam energy as indicated by the negative energy offset (Fig. 5.17a). Moreover, the reported energy spread is the Full Width at Half Maximum (FWHM) obtained by the relation $\text{FWHM} = 2 \cdot \sqrt{2 \ln 2}\,\sigma_E$. The energy spread exhibits an almost linear increase as a function of coil current with a higher spread for higher coil current (Fig. 5.17b).

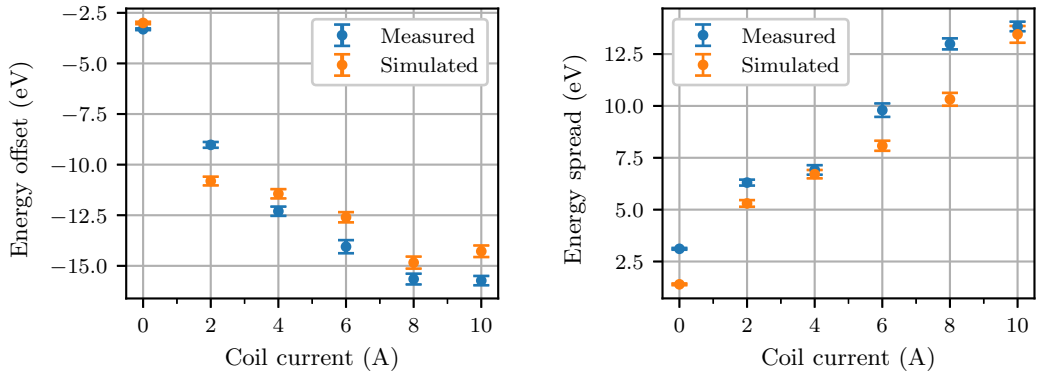

(a) Mean energy offet

(b) Energy spread

Figure 5.17: Ion beam energy measurements in an ARIEL-like geometry. In (a) the energy offset increases with coil current and a saturation seems to arise as of 8 A. In (b) the energy spread increases linearly with coil current as predicted from simulations.

The behavior on mean energy and energy spread can be explained from the ionization maps of Sec. 3.5. The ionization map shows that the ions are mostly created between the grid and the potential well. In this region, the voltage difference corresponds to the energy spread and the potential average corresponds to the energy offset. The magnitude of these quantities change with coil current because the generated magnetic field increases the electron current density linearly and its space charge effects lower the electric potential (see Fig. 5.18).

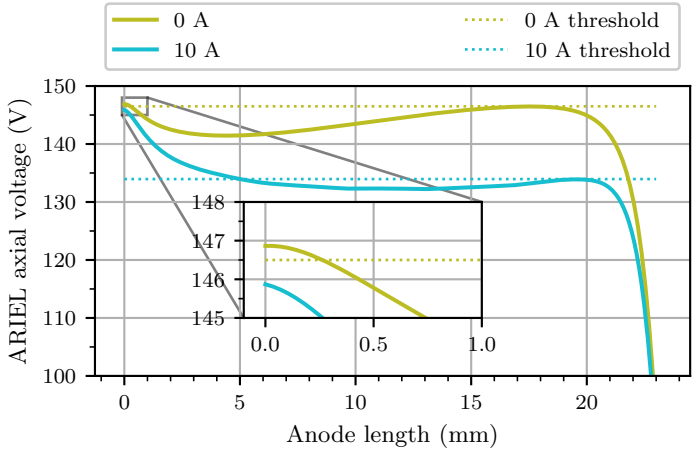

Figure 5.18: Simulated axial electric potential for two coil current values at an anode voltage of 150 V. The threshold dashed line corresponds to the delimiting potential barrier contour. The inset facilitate to note the threshold for the coil value of 0 A. With increasing coil current the potential where the ions are created causes higher energy spread.

Given that the energy offset is negative, the potential well must exist and the possible ion charge compensation is not enough to distinguish it from an electron dominant regime. Moreover, during the experimental campaign, the second most intense species was water (and its fragments). Water is known for also producing negative ions in the form of O_2^- and OH^- for electron energies below 15 eV [66, 67]. The secondary electrons arising from the ionization, move at energies ranging from $\approx$0.2 eV to $\approx$30 eV, which is the difference from the potential well towards the anode walls. Therefore, these electrons could interact with the water molecules to generate negative ions that likely compensate the positive ions not extracted, and effectively reduce any significant ion charge imbalance inside the anode volume. This indicates that the FEBIAD performs as an electron impact ion source with space charge effects but not as an arc discharge as the name suggests. Nevertheless, under the appropriate condition, it could be possible to ignite a discharge but this can be catastrophic for the source as the grid will likely melt as shown in Sec. 4.1. With the validated numerical model, simulation-based optimizations are performed to increase the ion creation and extraction.

Chapter 6

Simulation-Based Optimization Proposed for ISAC and ARIEL

The goal of the ionization numerical model is not only to fundamentally understand the inner mechanisms of the source but also to propose new designs that increase the overall ionization efficiency performance, reliability, and ease of operation. With the validated model shown in previous chapters, simulation-based optimizations are performed for ISAC and ARIEL. This chapter shows the design changes arising from optimizing the electron transport and the ion extraction.

6.1 Electron Emission

The electron emission is defined by the cathode temperature and the electric field between the cathode emitting surface and the grid (see Sec. 3.1). In order to optimize the electron emission and extraction, two aspects need to be optimized. As explained in Secs. 4.1 and 5.3, the cathode is subjected to deflections and the grid to intense heating. With these limitations, the optimization goal for the transferline is to reduce the deflections and move the transferline hotstpot (see Sec. 4.1.1) closer to the transferline outlet to contribute to useful thermal electron emission. The goal for the grid is to increase the heat conduction from the center to the edges while reducing deflections. The simulations have been developed with COMSOL multiphysics as it incorporates optimization routines within the numerical solver.

The transferline has been studied with a so-called shape optimization routine. In this routine, the software allows to vary the outer boundaries to reach the optimization goal. The goal for the transferline optimization is to have a homogeneous temperature, move the hotspot towards the cathode and increase its stiffness. Preliminary

simulations were performed to obtain suitable initial conditions for the optimization routine. The results show a thicker transferline that helps prevent deflections (see Fig. 6.1). By applying 25 A more heating current, the transferline outlet presents an ≈30 °C higher temperature but the overall transferline temperature is lower compare to the nominal geometry; moreover, the temperature is more homogeneous and shows a gradient of only 25 °C compared to the almost 110 °C with the nominal geometry (see Fig. 6.2).

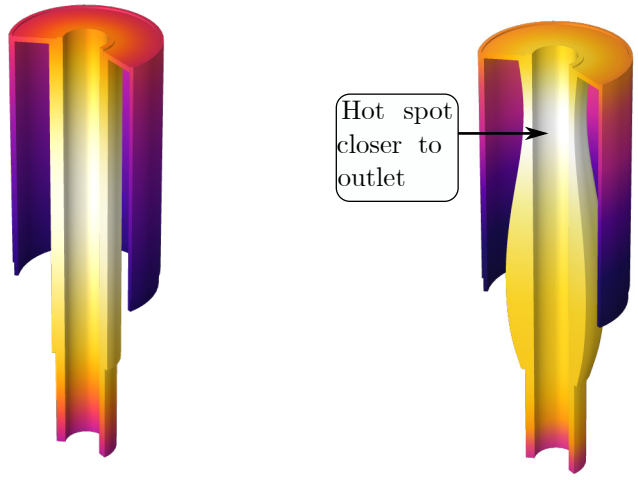

(a) Nominal geometry **(b)** Optimized geometry

Figure 6.1: Shape optimization performed to move the hotspot closer to the cathode face.

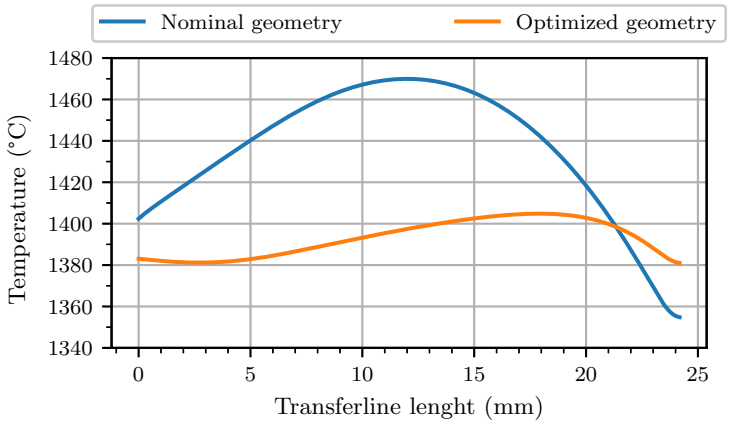

Figure 6.2: Temperature comparison along the transferline between nominal and optimized geometry. The nominal geometry shows a higher gradient compared to the optimized cased. Furthermore, the hotspot in the optimized geometry has been moved towards the transferline outlet. The extra heating current required is of only 25 A and easily achievable with the present infrastructure.

To increase the electron extraction, a new grid is proposed by means of a so-called generative design optimization (see Fig. 6.3). In this case, by defining the objective goals for a heat transfer analysis, the software develops an optimal geometry in a given volume. For the grid, the main goal is to increase the conductive paths from the center to the cooler edge while maintaining enough transparency. Based on the melted grid radius (see Sec. 4.1.1), the center of the grid has been removed to allow a better tunable source from the magnetic field (see Sec. 5.2). The goal is to still have a metal piece in front of the hottest part of the cathode to maintain an electric field and keep the same electron transport profile as for the open grid geometry. This objective has an extra constriction of keeping the material to void ratio at 30% to prevent blocking the electrons.

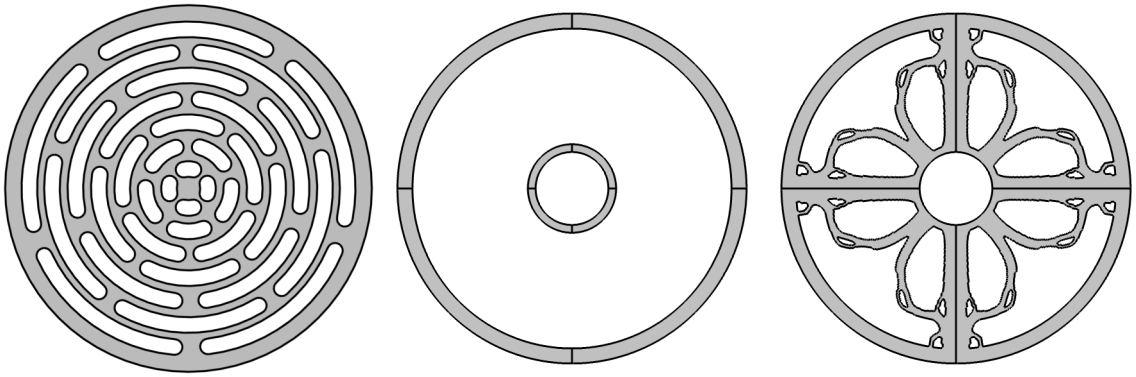

(a) Nominal geometry **(b)** Initial geometry **(c)** Optimized geometry

Figure 6.3: Geometry comparison for the generative design of the grid. In (a), the nominal grid is reproduced for comparison. In (b), the initial material is only defined at the center and the outer edge of the grid. In (c), the goals defined generate a pattern that increases heat conduction towards the colder edge.

The heat transfer simulation confirms the reduction of the grid temperature from 3100 °C (see Fig. 4.13) to 2350 °C for a voltage of 500 V and electron current of 150 mA (see Fig. 6.4). The increased conductance paths from the center to the colder edge enable better cooling. In this way, higher power deposition into the grid is achievable.

The optimization performed for the transferline and the grid enables higher electron current into the anode volume. With this higher current, the number of ionization events is expected to increase as indicated in Eq. 3.11 and observed in Sec. 5.3. The optimization of both grid and transferline, arises due to the coupled heating, electric field, and power deposition. Optimizing one without the other develops in overall suboptimal performance.

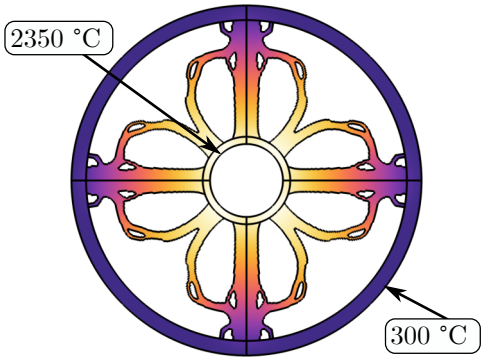

Figure 6.4: Optimized temperature profile with the new grid design.

6.2 Ion Extraction

The ions extracted, as predicted by the numerical model, originate in the vicinity of the grid (see Sec. 3.5). To enhance the number of ions extracted from this region, two different strategies have been simulated. The first consists of increasing the anode outlet to define a different electric potential inside the anode volume. The second consists of applying a specific magnetic field to control the electrons and in this way increase the ionization rate in areas of interest.

The ISAC anode outlet has been increased from the nominal radius of 1.5 mm to 2.5 mm. With this change, the number of ions extracted almost doubles compared to the nominal geometry, from 44 % to 86 %; however, the 4RMS-emittance increases almost 40 %, which could prevent optimal beam transport. Specifically, the emittance increases from 27 µm to 38 µm. The large extraction factor and the large emittance value arise from the initial position of the ions that are distributed over most of the anode volume. This can be seen from an axial electric potential plot where the potential well reduction increases the available area for ionization and extraction (see Fig. 6.5).

To increase the ion extraction while maintaining the beam quality, the ARIEL anode outlet remains at the nominal radius but a customized magnetic field is proposed for shaping the electric potential inside the anode volume (see Fig. 6.6). The magnetic field proposed consists of two peaks and one valley at the center of the anode volume (see Fig. 6.6a). In this way, the magnetic field proposed focuses the electron at two different locations. The first location is at the grid, which contributes to the area of higher extraction. The second location is near the outlet, which decreases the electric potential barrier. Furthermore, the electron beam is defocused

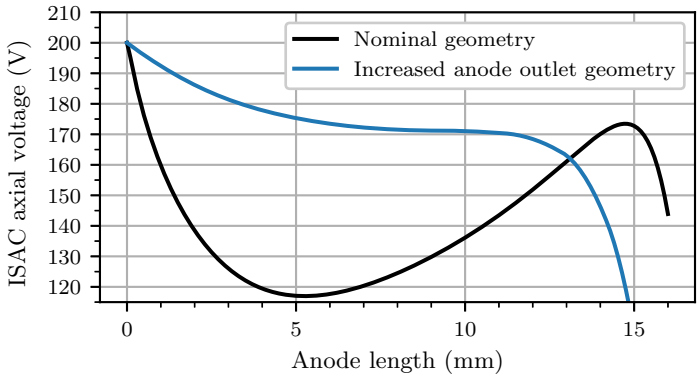

Figure 6.5: Electric potential showing a smaller potential well from which more ions are extracted.

at the anode volume center, reducing the space charge effects at this location. This magnetic field not only reduces the potential at the anode outlet but also reduces the well's depth (see Fig. 6.6b). Consequently, the beam emittance remains almost the same as the nominal geometry, that is 28 µm. The overall extraction increases to 84 % and Table 6.1 summarizes the modification and improvements.

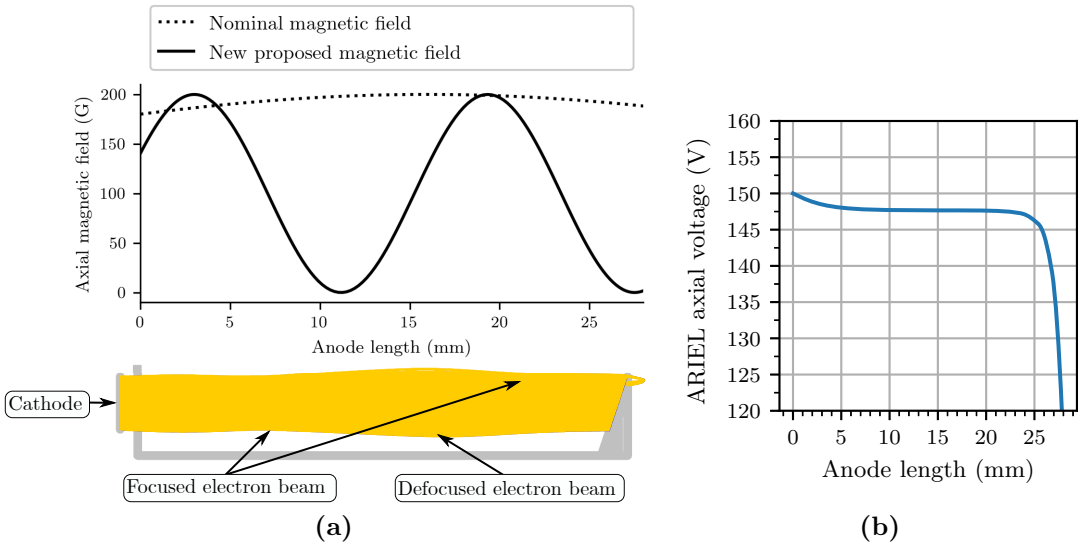

Figure 6.6: Proposed magnetic field with its effect on the electron trajectories and the resulting electric potential. In (a), a two-peak magnetic field controls the electron trajectories, defining the electric potential. In (b), the electric potential shows a smaller well, and hence more ions are extracted.

As a proof of principle, one way to obtain such a magnetic field is by using three separate electromagnets and two power supplies (see Fig. 6.7). The electromagnets are concentric to each other and spaced 5 mm apart, and the middle one has half the

Table 6.1: Comparison between proposed changes to increase ion extraction.

Modification	Outlet diameter (mm)	Emittance (µm)	Extraction (%)
None	3	27	44
Outlet	5	37	86
$\vec{B}$ field	3	28	84

radius of the outer electromagnets. Additionally, the middle electromagnet runs the current in the opposite direction with respect to the other two. To cancel out the field, the middle current value is around 80 % to 90 % of the exterior electromagnet current. The magnetic field is easier to implement in the ARIEL geometry as there is more space available for development. For ISAC, a new heatshield with better cooling needs to be developed to accommodate a larger coil current, as well as increasing the length of the anode volume.

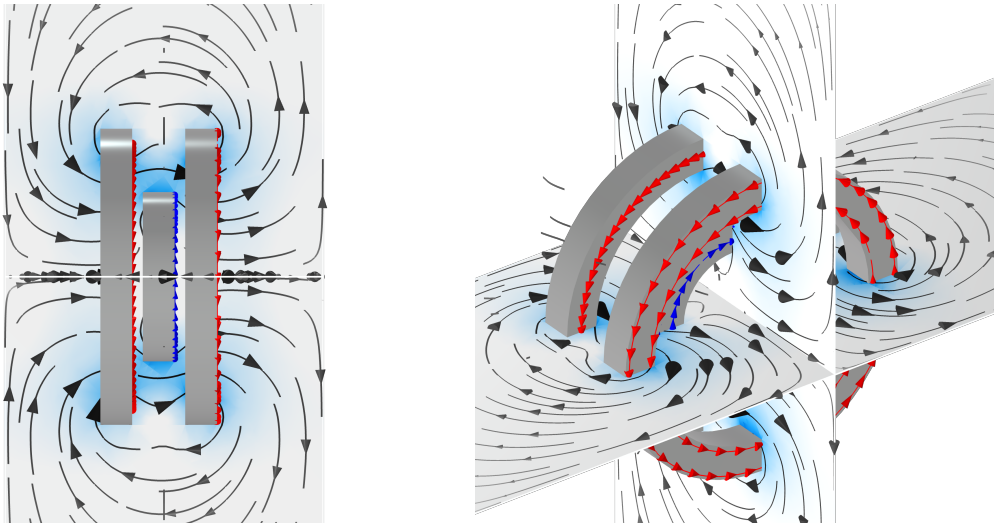

(a) Electromangets side view **(b)** Electromangets isometric view

Figure 6.7: Magnetic field realization with three electromagnet coils. In (a), the middle electromagnet has a smaller radius. In (b), the red and blue arrows indicate the direction in which the current is flowing. In both images, the black arrow lines indicate the magnetic field streamlines; the surface plots indicate the magnitude of the magnetic field, where the highest value is located near the electromagnetic coils.

Chapter 7

Conclusions

The simulation and experimental results for a FEBIAD ion source have been presented and they provide insight into the driving and limiting mechanisms of performance. The FEBIAD is a well established ion source for producing radioactive ion beams, but performance improvements are required for existing and new ISOL facilities. Increased performance on the ISAC-FEBIAD and in-depth understanding of FEBIAD-type ion sources are obtained from this research.

A numerical model has been developed comprising the relevant operational parameters of the FEBIAD ion source and from fundamental principles. The model can be considered a multiphysics approach as the different phenomena are affected by each other. Specifically, the attention on electron transport and its interaction with the electric and magnetic fields has led to improved modeling fidelity. As part of the fidelity, the FEBIAD numerical model has included the magnetic field for the first time in these types of studies.

The ancillary services' experimental and numerical characterization has led to infrastructure upgrades. The characterization results not only have defined the current status of the FEBIAD ion source but have also opened new avenues for offline characterization. Specifically, the implementation of HLA scripts to control and record the FEBIAD parameters enable automatic, consistent, and systematic characterization prior to online operations.

The multiparameter ion beam investigations have provided a broader picture of the competing phenomena at play in the ion source. In this research, the fine granularity of the measured ionization efficiency allows to directly observe the interconnected trends between anode voltage and cathode temperature. Moreover, the multiparameter measurements can be applied both offline and online to identify the exact values that optimize the ionization efficiency for an isotope of interest. Furthermore, beam energy measurement as a function of the magnetic field provides a lower limit for the magnitude of the ion beam energy spread.

The established methodology not only helps TRIUMF to achieve improved ion source characterization but also can be applied in other facilities. The correlation of anomalous current could be used to determine geometrical changes of the source during operation. Moreover, with a detailed offline scan parametrization it could be possible to achieve chemical selectivity by operating the source at different settings. Furthermore, by injecting a mixture of gases to react inside the anode volume, the parametrization could also be used to study the optimal setting at which molecular formation and/or break-up occurs. These molecular reactions can potentially be included within the current COMSOL model because the software can model reaction rates either by customized coupled ordinary differential equations, or directly by using the dedicated chemical reaction module. With the possibility of more data collection, the numerical model can be further refined to improve the source assemblies to ultimately enable routine online operation of the FEBIAD ion source.

In this last regard, the lack of reliability of the FEBIAD source prevented systematic online characterization and optimization. The main differences expected are the number of neutrals to ionize and the temperature profile, originating from the radioactive isotopes neutral density and the extra heat deposition from the driver beam, respectively. However, with the established methodology, FEBIAD ion sources can now be tested online. These measurements will serve as a benchmark for the development and open avenues to apply the methodology to short-lived isotope species.

Finally, the FEBIAD ion source is driven by electron impact ionization under strong space charge effects. Ionization efficiency measurements confirm that most of the ions observed experimentally are created just beside the grid as predicted by the simulation. The energy spread measurements in an ARIEL-like geometry indicate that the electron dominant regime is valid within the studied parameter space. The ionization model allows proposing geometrical and operational changes to increase the ionization efficiency while maintaining beam quality. At ISAC, the FEBIAD performance can now be improve by allowing more electrons into the anode and operating a more reliable cathode to higher temperatures. With the simulation-based optimization obtained, the geometrical changes can potentially increase the ionization efficiency ten-fold.

Bibliography

[1] Köster U, Arndt O, Bouquerel E *et al.* "Progress in ISOL target-ion source systems". *Nucl. Instruments Methods Phys. Res. Sect. B Beam Interact. with Mater. Atoms* **266**(19-20) 2008, pp. 4229–4239. DOI: 10.1016/j.nimb.2008.05.152.

[2] Stora T. "Radioactive ion sources". *CAS-CERN Accel. Sch. Ion Sources - Proc.* 2013, pp. 331–349. DOI: 10.5170/CERN-2013-007.331.

[3] Kirchner R and Roeckl E. "A novel isol ion source". *Nucl. Instruments Methods* **139**(C) 1976, pp. 291–296. DOI: 10.1016/0029-554X(76)90687-X.

[4] Penescu L. "Techniques to produce and accelerate radioactive ion beams". PhD thesis. Universitatea Politehnica din Bucarest, 2009. URL: http://cds.cern.ch/record/2259078.

[5] Martinez Palenzuela Y. "Characterization and optimization of a versatile laser and electron-impact ion source for radioactive ion beam production at ISOLDE and MEDICIS". PhD thesis. KU Leuven, 2019. URL: https://cds.cern.ch/record/2672954?ln=en.

[6] Maldonado Millan F, Day Goodacre T, and Gottberg A. "Multiphysics simulation of a FEBIAD ion source". *Nucl. Instruments Methods Phys. Res. Sect. B Beam Interact. with Mater. Atoms* **463** 2020, pp. 302–304. DOI: 10.1016/j.nimb.2019.04.078.

[7] Maldonado Millan F, Babcock C, Day Goodacre T, and Gottberg A. "Anomalous Ionization Regime in a Forced Electron Beam Induced Arc Discharge Ion Source for Singly Charged Radioactive Ion Beam Production". *J. Phys. Conf. Ser.* **2244**(1) 2022, p. 012074. DOI: 10.1088/1742-6596/2244/1/012074.

[8] Floettmann K. "Some basic features of the beam emittance". *Phys. Rev. ST Accel. Beams* **6**(3) 2003, p. 034202. DOI: 10.1103/PhysRevSTAB.6.034202.

[9] Marchetto M, Ames F, Baartman R *et al.* "Status of the CANREB high-resolution separator at TRIUMF". *Nucl. Instruments Methods Phys. Res. Sect. B Beam Interact. with Mater. Atoms* **463** 2020, pp. 227–231. DOI: 10.1016/j.nimb.2019.05.032.

[10] Roth JR. *Industrial Plasma Engineering*. 1st ed. Boca Raton, FL: CRC Press/Taylor & Francis, 1995, p. 339. DOI: 10.1201/9780367802615.

[11] Lamar ES, Samson EW, and Compton KT. "High current ion sources for nuclear investigations". *Phys. Rev.* **48**(11) 1935, pp. 886–892. DOI: 10.1103/PhysRev.48.886.

[12] Koch J. "Electromagnetic Separation of Noble Gas Isotopes and Their Use in Some Nuclear and Spectroscopic Experiments". *Mass Spectrosc. Phys. Res. Proc. NBS Semicentennial Symp. Mass Spectrosc. Phys. Res. Held NBS Sept. 6, 7, 8, 1951*. National Bureau of Standards, Circular 522, 1953, pp. 165–178. URL: http://nvlpubs.nist.gov/nistpubs/Legacy/circ/nbscircular522.pdf.

[13] Kofoed-Hansen O and Nielsen KO. "Short-lived krypton isotopes and their daughter substances". *Phys. Rev.* **82**(1) 1951, pp. 96–97. DOI: 10.1103/PhysRev.82.96.2.

[14] Kofoed-Hansen O and Nielsen K. "Measurements on short-lived radioactive krypton isotopes from fission after isotopic separation". *Dan. Mat. Fys. Medd.* **26**(7) 1951. URL: http://gymarkiv.sdu.dk/MFM/kdvs/mfm%2020-29/mfm-26-7.pdf.

[15] Blumenfeld Y, Nilsson T, and Van Duppen P. "Facilities and methods for radioactive ion beam production". *Phys. Scr.* **T152**(T152) 2013. DOI: 10.1088/0031-8949/2013/T152/014023.

[16] Gottberg A. "Target materials for exotic ISOL beams". *Nucl. Instruments Methods Phys. Res. Sect. B Beam Interact. with Mater. Atoms* **376** 2016, pp. 8–15. DOI: 10.1016/J.NIMB.2016.01.020.

[17] Kirchner R and Roeckl E. "Investigation of small-volume gaseous discharge ion sources for isotope separation on-line". *Nucl. Instruments Methods* **131**(2) 1975, pp. 371–374. DOI: 10.1016/0029-554X(75)90342-0.

[18] Gales S. "SPIRAL2 at GANIL: Next Generation of ISOL Facility for Intense Secondary Radioactive Ion Beams". *Nucl. Phys. A* **834**(1-4) 2010, pp. 717c–723c. DOI: 10.1016/j.nuclphysa.2010.01.130.

[19] Dilling J, Krücken R, and Merminga L. "ARIEL overview". *ISAC ARIEL TRIUMF Radioact. Beam Facil. Sci. Progr.* (October 2013) 2014, pp. 253–262. DOI: 10.1007/978-94-007-7963-1_30.

[20] Woo HJ, Kang BH, Tshoo K *et al.* "Overview of the ISOL facility for the RISP". *J. Korean Phys. Soc.* **66**(3) 2015, pp. 443–448. DOI: 10.3938/jkps.66.443.

[21] Monetti A, Andrighetto A, Petrovich C *et al.* "The RIB production target for the SPES project". *Eur. Phys. J. A* **51**(10) 2015. DOI: 10.1140/epja/i2015-15128-6.

[22] Borge MJ. "Highlights of the ISOLDE facility and the HIE-ISOLDE project". *Nucl. Instruments Methods Phys. Res. Sect. B Beam Interact. with Mater. Atoms* **376** 2016, pp. 408–412. DOI: 10.1016/j.nimb.2015.12.048.

[23] Giles T. "Isolde V". *Nucl. Instruments Methods Phys. Res. Sect. B Beam Interact. with Mater. Atoms* **463** 2020, pp. 254–257. DOI: 10.1016/j.nimb.2019.05.025.

[24] Ames F, Bricault P, Heggen H *et al.* "Ion source developments for the production of radioactive isotope beams at TRIUMF". *Rev. Sci. Instrum.* **85**(2) 2014, pp. 2014–2017. DOI: 10.1063/1.4833926.

[25] Langmuir I and Kingdon KH. "Thermionic effects caused by vapours of alkali metals". *Proc. R. Soc. Lond. A* **107**(741) 1925, pp. 61–79. DOI: 10.1098/rspa.1925.0005.

[26] Kirchner R. "Progress in ion source development for on-line separators". *Nucl. Instruments Methods Phys. Res.* **186**(1-2) 1981, pp. 275–293. DOI: http://dx.doi.org/10.1016/0029-554X(81)90916-2.

[27] Kirchner R. "On the thermoionization in hot cavities". *Nucl. Inst. Methods Phys. Res. A* **292**(2) 1990, pp. 203–208. DOI: 10.1016/0168-9002(90)90377-I.

[28] Rumble JR, ed. *Electron Work Function of the Elements in CRC Handbook of Chemistry and Physics (Internet Version)*. 102nd ed. Boca Raton, FL: CRC Press/Taylor & Francis, 2021.

[29] *Yield Search - Yield Database*. URL: http://isys01.triumf.ca/search/yield/data (visited on 11/02/2021).

[30] Li R, Mostamand M, Romans J, Reich BB, and Lassen J. "Recent RILIS developments at the TRIUMF offline laser ion source test stand". *Hyperfine Interact.* **241**(1) 2020, pp. 1–8. DOI: 10.1007/s10751-020-1694-4.

[31] Mostamand M, Li R, Romans J *et al.* "Production of clean rare isotope beams at TRIUMF ion guide laser ion source". *Hyperfine Interact.* **241**(1) 2020, pp. 1–9. DOI: 10.1007/s10751-020-1704-6.

[32] Nielsen KO. "The development of magnetic ion sources for an electromagnetic isotope separator". *Nucl. Instruments* **1**(6) 1957, pp. 289–301. DOI: 10.1016/0369-643X(57)90025-7.

[33] Almén O and Nielsen KO. "Systematic investigation of a magnetic ion source for an electromagnetic isotope separator". *Nucl. Instruments* **1**(6) 1957, pp. 302–322. DOI: 10.1016/0369-643X(57)90026-9.

[34] Kirchner R and Roeckl E. "A cathode with long lifetime for operation of ion sources with chemically aggressive vapours". *Nucl. Instruments Methods* **127**(2) 1975, pp. 307–309. DOI: 10.1016/0029-554X(75)90504-2.

[35] Kirchner R and Roeckl E. "Investigation of gaseous discharge ion sources for isotope separation on-line". *Nucl. Instruments Methods* **133**(2) 1976, pp. 187–204. DOI: 10.1016/0029-554X(76)90607-8.

[36] Sundell S and Ravn H. "Ion source with combined cathode and transfer line heating". *Nucl. Instruments Methods Phys. Res. Sect. B Beam Interact. with Mater. Atoms* **70**(1-4) 1992, pp. 160–164. DOI: 10.1016/0168-583X(92)95926-I.

[37] Bricault P, Ames F, Achtzehn T *et al.* "An overview on TRIUMF's developments on ion source for radioactive beams (invited)". *Rev. Sci. Instrum.* **79**(2) 2008. DOI: 10.1063/1.2801344.

[38] Penescu L, Catherall R, Lettry J, and Stora T. "Development of high efficiency Versatile Arc Discharge Ion Source at CERN ISOLDE". *Rev. Sci. Instrum.* **81**(2) 2010, pp. 2–6. DOI: 10.1063/1.3271245.

[39] Day Goodacre T, Billowes J, Catherall R *et al.* "Blurring the boundaries between ion sources: The application of the RILIS inside a FEBIAD type ion source at ISOLDE". *Nucl. Instruments Methods Phys. Res. Sect. B Beam Interact. with Mater. Atoms* **376** 2016, pp. 39–45. DOI: 10.1016/j.nimb.2016.03.005.

[40] Martinez Palenzuela Y, Marsh B, Ballof J *et al.* "Enhancing the extraction of laser-ionized beams from an arc discharge ion source volume". *Nucl. Instruments Methods Phys. Res. Sect. B Beam Interact. with Mater. Atoms* **431** 2018, pp. 59–66. DOI: 10.1016/J.NIMB.2018.06.006.

[41] Manzolaro M, Meneghetti G, Andrighetto A, and Vivian G. "Electrical-thermal-structural finite element simulation and experimental study of a plasma ion source for the production of radioactive ion beams". *Rev. Sci. Instrum.* **87**(3) 2016, p. 033303. DOI: 10.1063/1.4943209.

[42] Bajeat O, Delahaye P, Couratin C *et al.* "Development of target ion source systems for radioactive beams at GANIL". *Nucl. Instruments Methods Phys. Res. Sect. B Beam Interact. with Mater. Atoms* **317**(PART B) 2013, pp. 411–416. DOI: 10.1016/j.nimb.2013.07.049.

[43] Tang B, Cui B, Chen L *et al.* "The commissioning of the BRISOL facility". *Nucl. Instruments Methods Phys. Res. Sect. B Beam Interact. with Mater. Atoms* **376** 2016, pp. 429–433. DOI: 10.1016/J.NIMB.2016.01.016.

[44] Tang B, Cui B, Chen L *et al.* "The development of the FEBIAD ion source for BRISOL". *Nucl. Instruments Methods Phys. Res. Sect. B Beam Interact. with Mater. Atoms* **463** 2020, pp. 154–157. DOI: 10.1016/j.nimb.2019.06.003.

[45] Dilling J, Krücken R, and Ball G. "ISAC overview". *ISAC ARIEL TRIUMF Radioact. Beam Facil. Sci. Progr.* (October 2013) 2014, pp. 1–8. DOI: 10.1007/978-94-007-7963-1_1.

[46] Schultz BE, Sandor J, Kunz P, Mjøs A, Kester O, and Ames F. "FEBIAD Ion Source Development At TRIUMF-ISAC". *9th Int. Part. Accel. Conf. (IPAC '18)* 2018, THPML041. DOI: 10.18429/JACoW-IPAC2018-THPML041.

[47] Delahaye P, Dubois M, Maunoury L *et al.* "New exotic beams from the SPIRAL 1 upgrade". *Nucl. Instruments Methods Phys. Res. Sect. B Beam Interact. with Mater. Atoms* 2019. DOI: 10.1016/J.NIMB.2019.04.063.

[48] Dombsky M, Baartman R, Doornbos J *et al.* "An ion source test stand for the ISAC facility at TRIUMF". *Nucl. Instruments Methods Phys. Res. Sect. B Beam Interact. with Mater. Atoms* **126**(1-4) 1997, pp. 50–54. DOI: 10.1016/S0168-583X(96)01072-5.

[49] Allison PW, Sherman JD, and Holtkamp DB. "An emittance scanner for intense low-energy ion beams". *IEEE Trans. Nucl. Sci.* **30**(4) 1983, pp. 2204–2206. DOI: 10.1109/TNS.1983.4332762.

[50] Donaldson C. *Pyrometer Calibration for Use on High-Power Tantalum Target Containers at TRIUMF*. Tech. rep. TRIUMF, 2019, pp. 1–11.

[51] *EPICS - Experimental Physics and Industrial Control System*. URL: https://epics.anl.gov/index.php (visited on 11/15/2021).

[52] *TRIUMF High Level Application*. URL: https://devel.hla.triumf.ca/high-level-apps/ (visited on 03/19/2022).

[53] Kluyver T, Ragan-Kelley B, Pérez F *et al.* "Jupyter Notebooks – a publishing format for reproducible computational workflows". *Position. Power Acad. Publ. Play. Agents Agendas*. Ed. by Loizides F and Schmidt B. IOS Press. 2016, pp. 87–90.

[54] Baartman R. *TRANSOPTR: Changes since 1984*. Tech. rep. 2016, pp. 1–16. URL: www.triumf.ca%20http://lin12.triumf.ca/text/design%7B%5C_%7Dnotes/b2016%7B%5C_%7D06/TRI-BN-16-06%7B%5C_%7DTRANSOPTR.pdf.

[55] *COMSOL - Software for Multiphysics Simulation*. URL: https://www.comsol.com/ (visited on 11/06/2021).

[56] Dushman S. "Electron Emission from Metals as a Function of Temperature". *Phys. Rev.* **21**(6) 1923, pp. 623–636. DOI: 10.1103/PhysRev.21.623.

[57] Humphries S. *Charged Particles Beams*. New York: Wiley, 1990.

[58] Child CD. "Discharge from hot platinum wires". *Science* **15**(379) 1902, pp. 553–554. DOI: 10.1126/science.15.379.553-a.

[59] Lotz W. "Electron-impact ionization cross-sections and ionization rate coefficients for atoms and ions from hydrogen to calcium". *Zeitschrift für Phys.* **216**(3) 1968, pp. 241–247. DOI: 10.1007/BF01392963.

[60] Vályi L. *Atom and ion sources*. New York: Wiley, 1977, p. 429. URL: https://inis.iaea.org/search/10485544.

[61] Ivanov D and Bourdon B. "Numerical simulations of magnetic electron-impact ion source". *Int. J. Mass Spectrom.* **442** 2019, pp. 35–43. DOI: 10.1016/j.ijms.2019.05.005.

[62] Park CJ and Ahn JR. "Effect of magnetic field in electron-impact ion sources and simulation of electron trajectories". *Rev. Sci. Instrum.* **77**(8) 2006. DOI: 10.1063/1.2336756.

[63] Rumble JR, ed. *Melting, Boiling, Triple, and Critical Point Temperatures of the Elements in CRC Handbook of Chemistry and Physics (Internet Version)*. 102nd ed. Boca Raton, FL: CRC Press/Taylor & Francis, 2021.

[64] Seiffert C. "Production of radioactive molecular beams for CERN-ISOLDE". PhD thesis. Technische Universität Darmstadt, 2015. URL: https://cds.cern.ch/record/2064456.

[65] Baartman R, personal communication, 2019.

[66] Song MY, Cho H, Karwasz GP *et al.* "Cross Sections for Electron Collisions with H2O". *J. Phys. Chem. Ref. Data* **50**(2) 2021, p. 023103. DOI: 10.1063/5.0035315.

[67] Compton RN and Christophorou LG. "Negative-ion formation in H2O and D2O". *Phys. Rev.* **154**(1) 1967, pp. 110–116. DOI: 10.1103/PhysRev.154.110.

Appendix A

Electron Emission Derivations

A.1 Richardson-Dushman Equation

A hot cathode is a fundamental aspect of current FEBIAD designs (see Sec. 3.1). In such cathodes, electrons are emitted in a process called thermionic emission. This process is driven by the temperature of the cathode and it is described by the Richardson-Dushman equation.

The derivation of the Richardson-Dushman equation starts by recalling that electrons follow the well-known Fermi-Dirac statistic distribution:

$$f_{\mathrm{FD}} = \frac{1}{\mathrm{e}^{\frac{\varepsilon - E_{\mathrm{F}}}{k_{\mathrm{B}} T}} + 1}, \tag{A.1}$$

where E_{F} is the Fermi Energy level (eV), ε the electron energy (eV), k_{B} the Boltzmann constant ($\mathrm{eV\,K^{-1}}$), and T the temperature (K).

Assuming the electrons are bound to a box and that only electrons perpendicular to one of the faces can escape, a threshold momentum can be defined based on the potential barrier ϕ (eV):

$$p_{\mathrm{zmin}} > \sqrt{2m\phi}. \tag{A.2}$$

The number of electrons in a metal with momentum in the interval $(p, p + dp)$ is given by the integral of the electron distribution multiplied by the number of states:

$$n_{\mathrm{e}} = \frac{2}{h^3} \int_{-\infty}^{\infty} dp_x \int_{-\infty}^{\infty} dp_y \int_{p_{\mathrm{zmin}}}^{\infty} dp_z \frac{1}{\mathrm{e}^{\frac{\varepsilon - E_{\mathrm{F}}}{k_{\mathrm{B}} T}} + 1}. \tag{A.3}$$

By definition, $J = e \cdot v \cdot n_{\mathrm{e}}$, or using momentum, $J = e \cdot (p/m) \cdot n_{\mathrm{e}}$. Therefore,

assuming that the escape direction is z:

$$J = \frac{e}{m} \cdot p_z \cdot n_\mathrm{e} = \frac{2e}{mh^3} \int_{-\infty}^{\infty} dp_x \int_{-\infty}^{\infty} dp_y \int_{p_\mathrm{zmin}}^{\infty} dp_z \frac{p_z}{\mathrm{e}^{\frac{\varepsilon - E_\mathrm{F}}{k_\mathrm{B}T}} + 1}, \tag{A.4}$$

In the so-called high-temperature limit, the exponential factor dominates due to $\varepsilon - E_\mathrm{F} \gg k_\mathrm{B}T$, and the Fermi-Dirac distribution effectively becomes the Maxwell-Boltzmann distribution:

$$\frac{1}{\mathrm{e}^{\frac{\varepsilon - E_\mathrm{F}}{k_\mathrm{B}T}} + 1} \approx \frac{1}{\mathrm{e}^{\frac{\varepsilon - E_\mathrm{F}}{k_\mathrm{B}T}}}, \tag{A.5}$$

from which Eq. A.4 becomes

$$\begin{aligned} J = \frac{e}{m} \cdot p_z \cdot n_\mathrm{e} &= \frac{2e}{mh^3} \int_{-\infty}^{\infty} dp_x \int_{-\infty}^{\infty} dp_y \int_{p_\mathrm{zmin}}^{\infty} \frac{p_z}{\mathrm{e}^{\frac{\varepsilon - E_\mathrm{F}}{k_\mathrm{B}T}}} dp_z, \\ &= \frac{2e}{mh^3} \int_{-\infty}^{\infty} dp_x \int_{-\infty}^{\infty} dp_y \int_{p_\mathrm{zmin}}^{\infty} p_z \cdot \mathrm{e}^{-\frac{\varepsilon - E_\mathrm{F}}{k_\mathrm{B}T}} dp_z, \\ &= \frac{2e}{mh^3} \cdot \mathrm{e}^{\frac{E_\mathrm{F}}{k_\mathrm{B}T}} \int_{-\infty}^{\infty} dp_x \int_{-\infty}^{\infty} dp_y \int_{p_\mathrm{zmin}}^{\infty} p_z \cdot \mathrm{e}^{-\frac{\varepsilon}{k_\mathrm{B}T}} dp_z. \end{aligned} \tag{A.6}$$

where the last step simply separated the subtraction on the exponential and was moved outside the integral. Furthermore, by expressing ε as a function of momentum, it follows that:

$$\varepsilon = \frac{p^2}{2m} = (p_x^2 + p_y^2 + p_z^2)/2m. \tag{A.7}$$

By substituting A.7 into A.6, it follows that:

$$J = \frac{2e}{mh^3} \cdot \mathrm{e}^{\frac{E_\mathrm{F}}{k_\mathrm{B}T}} \int_{-\infty}^{\infty} dp_x \int_{-\infty}^{\infty} dp_y \int_{p_\mathrm{zmin}}^{\infty} p_z \cdot \mathrm{e}^{-\frac{(p_x^2 + p_y^2 + p_z^2)}{2mk_\mathrm{B}T}} dp_z \tag{A.8}$$

$$= \frac{2e}{mh^3} \cdot \mathrm{e}^{\frac{E_\mathrm{F}}{k_\mathrm{B}T}} \int_{-\infty}^{\infty} \mathrm{e}^{-\frac{p_x^2}{2mk_\mathrm{B}T}} dp_x \int_{-\infty}^{\infty} \mathrm{e}^{-\frac{p_y^2}{2mk_\mathrm{B}T}} dp_y \int_{p_\mathrm{zmin}}^{\infty} p_z \cdot \mathrm{e}^{-\frac{p_z^2}{2mk_\mathrm{B}T}} dp_z \tag{A.9}$$

The integrals over dp_x and dp_y are known as Gaussian integrals, and for any real-valued parameter α they compute to the following:

$$\int_{-\infty}^{\infty} \mathrm{e}^{-\alpha \cdot x^2} dx = \sqrt{\frac{\pi}{\alpha}}. \tag{A.10}$$

Therefore, Eq. A.9 becomes

$$J = \frac{4ek_{\mathrm{B}}T}{h^3} \cdot \mathrm{e}^{\frac{E_{\mathrm{F}}}{k_{\mathrm{B}}T}} \int_{p_{\mathrm{zmin}}}^{\infty} p_z \cdot \mathrm{e}^{-\frac{p_z^2}{2mk_{\mathrm{B}}T}}\, dp_z. \tag{A.11}$$

The last equation can be solve by a change of variable $u = \dfrac{p_z^2}{2mk_{\mathrm{B}}T}$, and using A.2, from which is found that

$$\begin{aligned}
J &= \frac{4ek_{\mathrm{B}}T}{h^3} \cdot \mathrm{e}^{\frac{E_{\mathrm{F}}}{k_{\mathrm{B}}T}} mk_{\mathrm{B}}T \mathrm{e}^{\frac{-p_{\mathrm{zmin}}^2}{2mk_{\mathrm{B}}T}}, \\
J &= \frac{4ek_{\mathrm{B}}T}{h^3} \cdot \mathrm{e}^{\frac{E_{\mathrm{F}}}{k_{\mathrm{B}}T}} mk_{\mathrm{B}}T \mathrm{e}^{\frac{-(\sqrt{2m\phi})^2}{2mk_{\mathrm{B}}T}}, \\
J &= \frac{4mek_{\mathrm{B}}^2T^2}{h^3} \cdot \mathrm{e}^{\frac{E_{\mathrm{F}}}{k_{\mathrm{B}}T}} \mathrm{e}^{\frac{-\phi}{k_{\mathrm{B}}T}}, \\
J &= \frac{4mek_{\mathrm{B}}^2}{h^3} \cdot T^2 \cdot \mathrm{e}^{\frac{-(\phi - E_{\mathrm{F}})}{k_{\mathrm{B}}T}}.
\end{aligned} \tag{A.12}$$

By definition, the work function is the difference between the Fermi energy and the potential barrier, that is $W = (\phi - E_{\mathrm{F}})$, moreover, by collecting all the constants into A, it is found:

$$J = A \cdot T^2 \mathrm{e}^{\frac{-W}{k_{\mathrm{B}}T}}. \tag{A.13}$$

A.2 Schottky Correction

The thermionic emission from a hot cathode is enhanced by the presence of an electric field as is the case for the FEBIAD cathode (see Sec. 3.1). This electric field in the FEBIAD is defined by the voltage difference between the cathode and anode, and it increases because of geometrical changes during operation. Therefore, the electron current emitted by the FEBIAD cathode at high cathode temperatures and anode voltages can be described by the enhanced thermionic emission arising from the Schottky effect.

The Schottky effect consists of lowering the work function of the cathode material and therefore increases the total thermionic electron current emitted. In this effect, a constant electric field accelerates the thermally emitted electrons but in addition, an electric field arises from the image charges. The electric field of image charges

separated by a distance x is given by

$$E_{\mathrm{i}}(x) = -\frac{e}{4\pi\varepsilon_0}\frac{1}{(2x)^2} = -\frac{e}{16\pi\varepsilon_0}\frac{1}{x^2}. \tag{A.14}$$

For a metal boundary located at $x = 0$ the lowering in potential can be described as:

$$\delta\varphi = \int_0^{x_{\mathrm{c}}} E_{\mathrm{c}}\, dx + \int_{x_{\mathrm{c}}}^{\infty} E_{\mathrm{i}}\, dx, \tag{A.15}$$

where x_{c} is the distance in which the image charge starts dominating. At this distance

$$E_{\mathrm{c}} + E_{\mathrm{i}}(x_{\mathrm{c}}) = 0 = E_{\mathrm{c}} - \frac{e}{16\pi\varepsilon_0}\frac{1}{x_{\mathrm{c}}^2} \tag{A.16}$$

and solving for x_{c} leads to

$$x_{\mathrm{c}} = \sqrt{\frac{e}{16\pi\varepsilon_0 E_{\mathrm{c}}}}. \tag{A.17}$$

Furthermore, assuming a constant electric field E_{c} the first integral of A.15 is readily solved and we have the intermediate expression

$$\delta\varphi = E_{\mathrm{c}}x_{\mathrm{c}} - \frac{e}{16\pi\varepsilon_0}\int_{x_{\mathrm{c}}}^{\infty}\frac{1}{x^2}\, dx. \tag{A.18}$$

Solving the integral is straightforward and leads to

$$\delta\varphi = E_{\mathrm{c}}x_{\mathrm{c}} + \frac{e}{16\pi\varepsilon_0}\frac{1}{x_{\mathrm{c}}}. \tag{A.19}$$

Inserting A.17 into A.19

$$\begin{aligned}
\delta\varphi &= E_{\mathrm{c}}\sqrt{\frac{e}{16\pi\varepsilon_0 E_{\mathrm{c}}}} + \frac{e}{16\pi\varepsilon_0}\frac{1}{\sqrt{\frac{e}{16\pi\varepsilon_0 E_{\mathrm{c}}}}}, \\
&= \sqrt{\frac{eE_{\mathrm{c}}}{16\pi\varepsilon_0}} + \sqrt{\frac{e^2}{(16\pi\varepsilon_0)^2}}\frac{1}{\sqrt{\frac{e}{16\pi\varepsilon_0 E_{\mathrm{c}}}}}, \\
&= \sqrt{\frac{eE_{\mathrm{c}}}{16\pi\varepsilon_0}} + \sqrt{\frac{e^2}{(16\pi\varepsilon_0)^2}\frac{1}{\frac{e}{16\pi\varepsilon_0 E_{\mathrm{c}}}}}, \\
&= \sqrt{\frac{eE_{\mathrm{c}}}{16\pi\varepsilon_0}} + \sqrt{\frac{eE_{\mathrm{c}}}{16\pi\varepsilon_0}},
\end{aligned}$$

$$\delta\varphi = \sqrt{\frac{eE_c}{4\pi\varepsilon_0}}. \tag{A.20}$$

Finally, the energy reduction is the potential reduction times the elementary charge, that is:

$$\delta W = e \cdot \delta\varphi = \sqrt{\frac{e^3 E_c}{4\pi\varepsilon_0}}. \tag{A.21}$$

A.3 Child-Langmuir Equation

In a thermionic cathode, such as the FEBIAD's, the number of electron emitted depends on the temperature as long as the voltage is sufficient to extract them, and the cathode is said to operate in the thermal limited regime. However, when the voltage controls the maximum number of electrons, as is the case sometimes for the FEBIAD, the transport of electrons is prevented and the cathode is said to operate in the space-charge limited regime (see Sec. 3.2). This regime is described by the Child-Langmuir equation.

The derivation of the Child-Langmuir equation starts with the Poisson equation in 1-D:

$$\frac{d^2V}{dz^2} = \frac{\rho}{\epsilon_0}. \tag{A.22}$$

Moreover, the charge can be expressed as $\rho = J/v$, and v can be found from

$$\frac{1}{2}mv^2 = e \cdot V,$$

which combine to

$$\rho = J/\sqrt{\frac{2eV}{m}}. \tag{A.23}$$

By further combining Eqs. A.22 and A.23

$$\frac{d^2V}{dz^2} = \frac{J}{\epsilon_0\sqrt{\frac{2eV}{m}}}, \tag{A.24}$$

$$= \frac{JV^{-1/2}}{\epsilon_0\sqrt{\frac{2e}{m}}}. \tag{A.25}$$

The following boundary conditions are imposed: the cathode is located at $z = 0$ with

$V = 0$, the anode is located at $z = d$ with $V = V_{\mathrm{a}}$, and the electric field at the cathode surface is $dV/dz = 0$

The fist step to solve is multiplying both sides by $2 \cdot dV/dz$

$$2 \cdot \frac{dV}{dz}\frac{d^2V}{dz^2} = \frac{JV^{-1/2}}{\epsilon_0\sqrt{\frac{2e}{m}}} 2 \cdot \frac{dV}{dz}. \tag{A.26}$$

From which follows that

$$\frac{d}{dz}\left[\left(\frac{dV}{dz}\right)^2\right] = 2\frac{JV^{-1/2}}{\epsilon_0\sqrt{\frac{2e}{m}}}\frac{dV}{dz}. \tag{A.27}$$

Integrating once leads to

$$\begin{aligned}
\left(\frac{dV}{dz}\right)^2 &= 4\frac{JV^{1/2}}{\epsilon_0\sqrt{\frac{2e}{m}}} + \cancelto{0}{C_0}, \\
\frac{dV}{dz} &= 2\sqrt{\frac{JV^{1/2}}{\epsilon_0\sqrt{\frac{2e}{m}}}}, \\
\frac{dV}{dz} &= 2\sqrt{\frac{J}{\epsilon_0\sqrt{\frac{2e}{m}}}}V^{1/4}
\end{aligned} \tag{A.28}$$

Where the constant C_0 is found to be 0 when applying the boundary conditions. Re-arranging and integrating once more it follows:

$$\begin{aligned}
V^{-1/4}dV &= 2\sqrt{\frac{J}{\epsilon_0\sqrt{\frac{2e}{m}}}}dz, \\
\frac{4}{3}V^{3/4} &= 2\sqrt{\frac{J}{\epsilon_0\sqrt{\frac{2e}{m}}}}z + \cancelto{0}{C_1}, \\
\frac{2}{3}V^{3/4} &= \sqrt{\frac{J}{\epsilon_0\sqrt{\frac{2e}{m}}}}z,
\end{aligned} \tag{A.29}$$

where the constant $C_1 = 0$ after applying the boundary conditions. By squaring and

solving for J is found that:

$$\frac{4}{9}V^{3/2} = \frac{J}{\epsilon_0\sqrt{\frac{2e}{m}}}z^2, \tag{A.30}$$

$$J = \frac{4}{9}\epsilon_0\sqrt{\frac{2e}{m}}\frac{V^{3/2}}{z^2}. \tag{A.31}$$

And for a voltage V_a applied to the anode which is located at a distance d, the classical expression is recovered:

$$J = \frac{4\epsilon_0}{9}\sqrt{\frac{2e}{m}}\frac{V_\mathrm{a}^{3/2}}{d^2}. \tag{A.32}$$